The impact of thermal fracturing on the near-wellbore region during CO_2 injection in depleted gasfields

A numerical investigation

B.B. Scheffer

Master Thesis

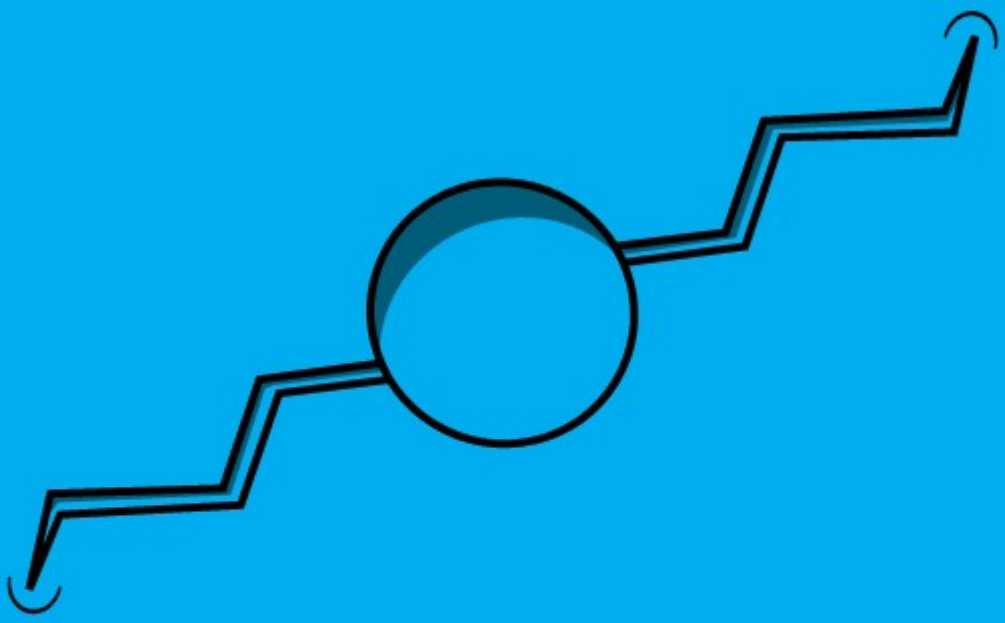

TU Delft

The impact of thermal fracturing on the near-wellbore region during CO_2 injection in depleted gasfields

A numerical investigation

by

B.B. Scheffer

to obtain the degree of Master of Science
at the Delft University of Technology,
to be defended publicly on Tuesday November 11, 2022 at 10:00 AM.

Student number: 4441664
Project duration: November 15, 2021 – November 11, 2022
Thesis committee: Dr. Ir. F. C. Vossepoel, TU Delft
Dr. A. D. Daniilidis, TU Delft
Dr. A. Barnhoorn, TU Delft
Ir. J. de Kok, EBN B.V.

TU Delft

Abstract

This research describes how thermal fractures impact the near-wellbore (NWB) region of a depleted gasfield in a carbon sequestration project. As CO2 is usually injected in its supercritical phase, the injection fluid is injected on high pressures and low temperatures. This is in high contrast with the depleted gasfields, which have a low reservoir pressure. The increase in pressure and decrease in temperature causes a thermoporoelastic response, resulting in a reduction of stress inside the reservoir. Once the fracture initiation stress, the so-called fracture stress, is reached, thermal fractures form.

Thermal fractures form only due to extensive cooling of the reservoir. The fractures impact the NWB region; due to opening of fractures there is a drop in pressure in the bottomhole pressure (BHP). This increases the reservoir's injectivity. This research uses CMG GEM to model this. The simulation uses a homogeneous box dual permeability model with the model being initialized as a generalized depleted gas reservoir in the North Sea. To model the fractures, the Barton Bandis model is used. This model changes the permeability in a fracture cell once fracture conditions are met.

From this model, the moment of fracturing (fracture time), the fracture halflength and the injectivity of the reservoir is researched by performing a sensitivity analysis on key parameters. It is found that the thermal fractures propagate conform to the propagation of the coldest part of the thermal front. The thermal front propagates further once the fracture conditions are met sooner due to fluid highways or when the pressure build up in the reservoir is slower.

The sensitivity on the geomechanical parameters showed that only the stress conditions in the reservoir changed, causing the injection constant to change and thus a different fracture time. The way the reservoir reacted to the initiation of fractures was the same; the injectivity was improved similarly for each parameter.

The effective permeability (thickness and permeability) determines, together with the injection rate, the way the pressure builds up in the reservoir changes the increase of injectivity due to fracturing slightly. Increasing the reservoir volume causes a slower pressure build-up inside of the reservoir, allowing the thermal front to propagate further and thus longer fracture lengths.

Lastly, the sensitivity on the thermal effects showed that a higher difference between the reservoir and injection temperature causes the fracture to be less dependent on the increase of pressure to fracture, resulting in earlier fracturing and longer fracture halflength. The pressure build-up is not changed, so the injectivity remains similar to the basecase scenario.

All in all, this thesis gives an insight on how key parameters impact thermal fracture behavior. It also shows what range of parameters can be expected. Combining these two gives an insight on what parameters the focus should be on to better describe the behavior of thermal fractures, to economize the operation by leaving out or including extensive data collection on key parameters. This helps to improve the injection strategy with CO2 injection projects in depleted gasfields.

Preface

This thesis ends my era as a student. For the past seven years I have tried to educate myself to better understand the earth, and now especially the geo-energy beauty of it. To achieve this I am incredibly thankful to firstly the TU Delft, which gave me a terrific learning environment. Even though most of the experience was through online classrooms, I have made great development both personally as professionally by the guidance of all my lecturers and especially my colleague students.

Secondly, I would like to thank EBN B.V., and more specifically the CCS team. The team gave me an utmost warming welcome, allowing me to really experience what it is like to work in the energy transition sector. An experience that is almost as valuable as the experience I acquired by writing this thesis.

Next, I would like to thank my EBN supervisors; Rowan, Thijs and Joop. Although Rowan left the company in the middle of my thesis, the wisdom on how to model CCS projects and the process involved really gave me an understanding on what is possible with numerical models and how to work methodologically towards a solid research. Thijs, on its turn, always had great ideas on how to tackle an issue and motivated to solve problems by critically thinking about the physics involved, rather than just accept what a model provides. Joop was a great help with solving numerical problems, while also helping me focus on where the emphasis should be on. His expertise on reservoir simulation always gave me the confidence that there was a solution when issues arose, even though it might take a few days to solve them.

Then, my TU Delft supervisors, Alex and Femke. Although the contact was limited over the last year, I have never felt like I could not ask a question, which I think is extremely important in a thesis research. Together with the critical but positive feedback you provided you helped me focus on how to formulate my work correctly, something I struggled with myself.

Lastly I want to thank my family. The last years have been tough, but by sticking together and looking out for each other we have managed to continue, for me ultimately leading to this Master's degree. Therefore I want to dedicate this thesis to my parents. I wish you were both still here to witness this.

B.B. Scheffer
Rotterdam, November, 2022

Contents

List of Figures

List of Tables

1 Introduction

The urgency to reduce CO_2 emissions is increasing by the day [1], with an anthropogenic carbon footprint of 35 Gt in 2020 [2, 3]. The climate plan of Paris aims to reduce the emissions with 95 % compared to 1990 by 2050, to limit the global warming to 1.5 °C [1]. To reach this goal, a transitional period has been started to switch from the traditional emitters towards more renewable and cleaner alternatives. This process is widely known as the energy transition. For the Netherlands, the goal is to reduce the greenhouse gas emissions with 49% compared to 1990 before 2030, meaning a reduction of CO_2 discharge to the atmosphere to 49 Mt [4]. However, with an emission of 138 Mt CO_2 in 2020 [2, 3] and with the demand for energy increasing, temporary and imminent solutions for diminishing the emissions have to be considered. One of these solutions is storing the CO_2 in the subsurface.

1.1. Subsurface storage of CO_2

The sequestration of CO_2 is a type of a Carbon Capture, Utilization and Storage (CCUS) project (Figure 1.1). It is an operation where carbon dioxide is injected into the subsurface. Once injected, the CO_2 is expected to remain permanently in the reservoir, instead of contributing to the greenhouse effect in the atmosphere. A CCUS project can be shaped in different forms and sizes. Figure 1.1 gives an overview of the possibilities. It can be used as an injection fluid for Enhanced Oil Recovery (EOR) projects, injected in saline aquifers or in depleted gas fields.

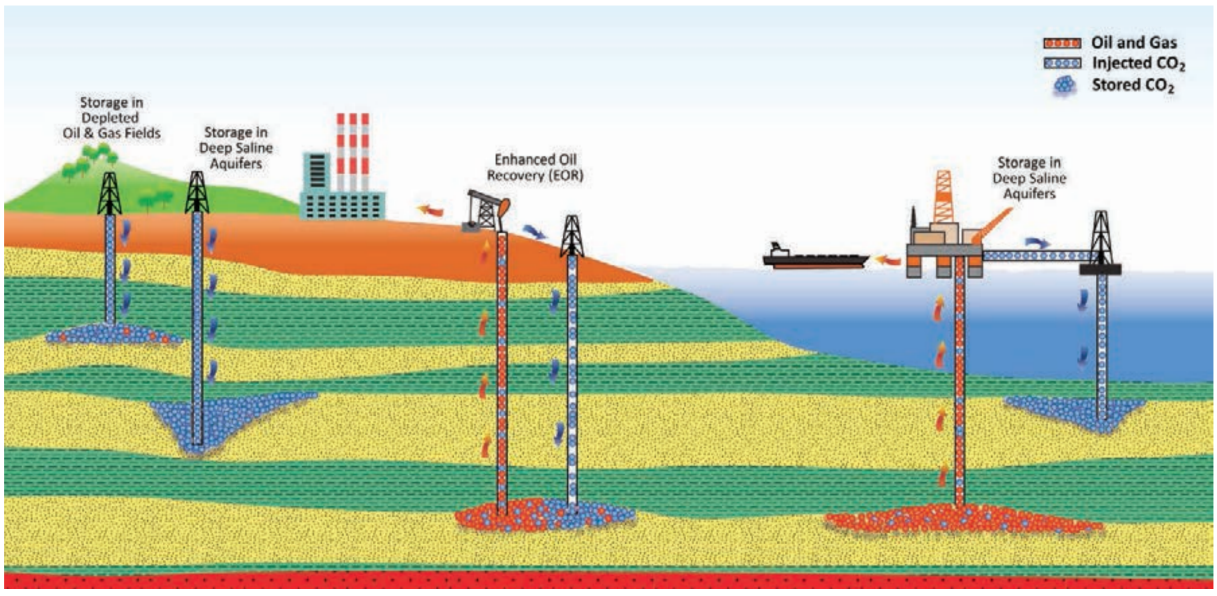

Figure 1.1: Different types of CCUS projects [5].

In 2021, the yearly amount of stored CO_2 is 40 Mt [6]. Together with the projects that are being developed, which aim to store another 50 Mt yearly, one-thousandth of the yearly worldwide CO_2 emissions is stored in the subsurface [6]. The current world-leaders in CCS are the United States, where CO_2 is mainly stored after it is captured from gas powered plants. The CO_2 is then used as an injection fluid

for EOR purposes or in saline aquifers [6]. In case of the Netherlands, there is momentarily multiple projects under development for CCS in depleted gasfields. For these projects, it is important to understand all involved processes as thorough as possible. This research focuses on the thermal effect on the geomechanical state of a reservoir, as this is not yet fully understood.

1.2. Prior knowledge and advances of CO_2 and thermal effect on the geomechanical state of a reservoir

During CO_2 injection, the CO_2 slowly fills the reservoir. The CO_2 preferably is injected in its dense or supercritical phase due to flow assurance and economic reasoning [7]. CO_2 is in its dense phase with higher pressures or lower temperatures. For CCUS projects in EOR or aquifers, the high initial pressure means that the temperature does not have to be lowered excessively to reach dense phase. However, the pressure increase in the reservoir together with the cooling due to the relatively low temperatures of CO_2 during injection can cause fractures to form, that are initiated due to the change in pressure and the temperature. These kind of fractures are called thermal fractures.

In previous research on the effect of the cooled down zone of the reservoir, the so called thermal front, it is found that fracture length increases when thermal effects are the catalyst for fracturing [8]. This is expected to have a larger impact with greater temperature differences. However, this is highly dependent on the propagation velocity of the CO_2 plume. it is also found that the propagation of the thermal front stays behind when the propagation speed of the CO_2 plume is enhanced by increasing the rate [9]. The cooling of the rock near the fracture is a slower process than pressure diffusion. This means that with an increased rate, the driving force behind the stress change in the whole reservoir is less dependent on the thermal influence. This makes fracture propagation less dependent on the thermal effects. Therefore, it is possible to identify two regimes: a regime where the thermal effect controls fracture propagation and a regime where it is more pressure controlled, while both thermal and pressure effects play a role in the change of stress conditions [9].

These findings on the relation between pressure dissipation and the behavior of the thermal front led to new research on the effect of fracturing. It concluded that injection into the reservoir becomes easier due to thermal fractures [8, 10]. This improvement is called an increase of injectivity of the reservoir. On its turn, the fractures then influence the propagation of the CO_2 front, effectively changing the shape to be more elliptic along the fracture direction. This change in shape allows for faster propagation of the thermal front, allowing further propagation of the fracture into the reservoir [10] (Figure 1.2). This ellipsoidic plume can cause an increased vertical propagation of the CO_2, which leads to cooling of the caprock. This cooling might initiate a breach of the caprock [8, 11]. To reduce this risk, the vertical propagation can be limited by changing the injection rate or by increasing the injection temperature.

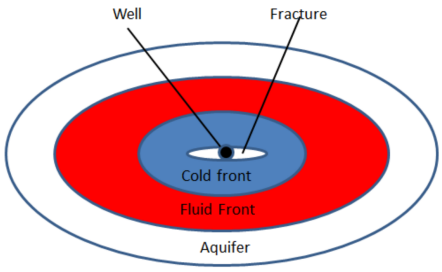

Figure 1.2: Elliptical shape of the thermal (cold) and fluid fronts around the injection well [12].

Other research found that the thermal front propagation is highly dependent on the geomechanical rock parameters. Especially the thermal expansion coefficient, which describes how a rock expands or shrinks due to a change in temperature. It is a measured parameter, with a higher thermal expansion coefficient leading to higher deformation and stress response for the same temperature change. This also leads to a thermal front that propagates faster [13]. This subsequently impacts the minimal horizontal stress, in such a manner that it can lead to inelastic strain in the cooled region [13]. It is important to understand the impact of the inelastic strain and deformation in the reservoir, as the thermal

expansion coefficient could be different in the caprock compared to the reservoir. If the thermal expansion coefficient is an order of magnitude larger in the caprock, it could be that the base of the caprock breaches due to vertical propagation of the fracture [13]. This could also be caused by injecting with increasing injection rates [14]. The shrinkage of the reservoir rock may lead to a reduction of compressional stress in the caprock, ultimately leading to a breach in the base of the caprock with increasing rates due to the vertical propagation of the thermal fracture from the reservoir to the caprock, as increased pore pressure enhance fracture propagation. This research [14], however, was conducted on a CCS project in a saline aquifer, which exceeded initial reservoir pressures after injection.

Contradictory to this, it is found unlikely that fractures will be initiated due to cooling effects in the caprock, as the drop in the in-situ minimum horizontal stress is different in the reservoir than in the sealing formation [15]. The thermal front propagates horizontally more easily in the reservoir due to a low vertical permeability compared to the horizontal. The caprock is also dominantly affected by conduction as advection is very limited due to its extremely low permeability. The cooling therefore has a positive effect on the vertical containment of the fracture as it is more likely to propagate horizontally due to limited cooling in the vertical direction.

Taking this information into account, an optimisation algorithm was proposed [16] on the operational parameters. It constrains the maximum fracture length by increasing the injection temperature (causing lower temperature difference) or by decreasing the injection rate. This also shows that thermal impact on fractures happens sooner or later during CO_2 injection, no matter how significant the temperature difference is, as the pore pressure increases continuously. This means that the injection temperature can be lowered to enhance thermal fracturing and thus an earlier increase of injectivity in the reservoir, or that the injection temperature can be increased to delay thermal fracturing until injection is shut off to prevent near-wellbore effects or seismic risks caused by thermal fractures.

A confirmation of this effect was found by Jung et al. [17]. They performed a history match in a CCS field in an saline aquifer, taking in to account pressure and thermal effects. In an operating reservoir, the pressure in the bottom of the borehole (bottom hole pressure) remained the same while the rate was increased. This observation could later be explained with history matching using CMG GEM dual permeability model. This happened in an aquifer based CCS project, but it shows that injection temperature should be considered when injecting into a reservoir. Without the thermal effect, the hydraulic pressure never reaches fracture stress in the simulation. The research however urged, that local heterogeneity could also be a cause of locally reaching fracture pressure, so definitive conclusions are premature, but it does show the possibility of significant increase of injectivity due to thermal fracturing in saline aquifers [17].

When translating this to depleted gas fields, the key challenge is maintaining flow control due to the high pressure differences between the well and the reservoir, especially in the beginning. Changing injectivity due to thermal fracturing may jeopardize this. For injection in a depleted gas field, it is preferred to inject CO_2 in a very dense state in the reservoir. The CO_2 must be expanded in the reservoir in a controlled manner, as the cold substance can cause excessive cooling, possibly causing ice and gas hydrates to form [18].

1.3. Research scope

The effect of thermal fracturing in saline aquifers is better understood, but, contrary to injection in depleted gas reservoirs, these aquifers have less extreme cooling. Therefore it is interesting to have a closer look to the effect of thermal fractures in depleted gas fields.

In these fields, the reservoir pressure is significantly lower compared to initial conditions [18]. This means that the thermal front has a much lower in temperature. This causes great changes in stress conditions in the reservoir, the so called thermo-elastic response. The relation between the propagation of the thermal front and with thermal fracture initiation and propagation together with their impact on the state of stress in the reservoir has to be better understood for CCS projects in depleted gasfields [8].

Additionally, it is momentarily not clear what the magnitude of impact of all relevant parameters have on the thermal fractures. Providing an overview of the main parameters that influence the stress conditions and thermal front propagation can help to get a better insight on the effect of thermal fractures during CO_2 injection in depleted gasfields.

2
Background

2.1. Offshore storage potential

CCS projects in the Netherlands have high potential in offshore depleted gas fields within the North Sea area (Figure 2.1). There are multiple advantages for storing it in depleted gas fields; 1) the subsurface knowledge and collected data is already very extensive compared to unexplored territory due to the gas production, 2) depleted gas fields are assumed to be containing, as gas remained in the subsurface for millions of years [19, 20], 3) offshore projects do not cause the same objections of locals compared to onshore CCS projects, where constructive stakeholder dialogue is complicated [21] and 4) infrastructure that is already in place for gas production can be modified and re-used.

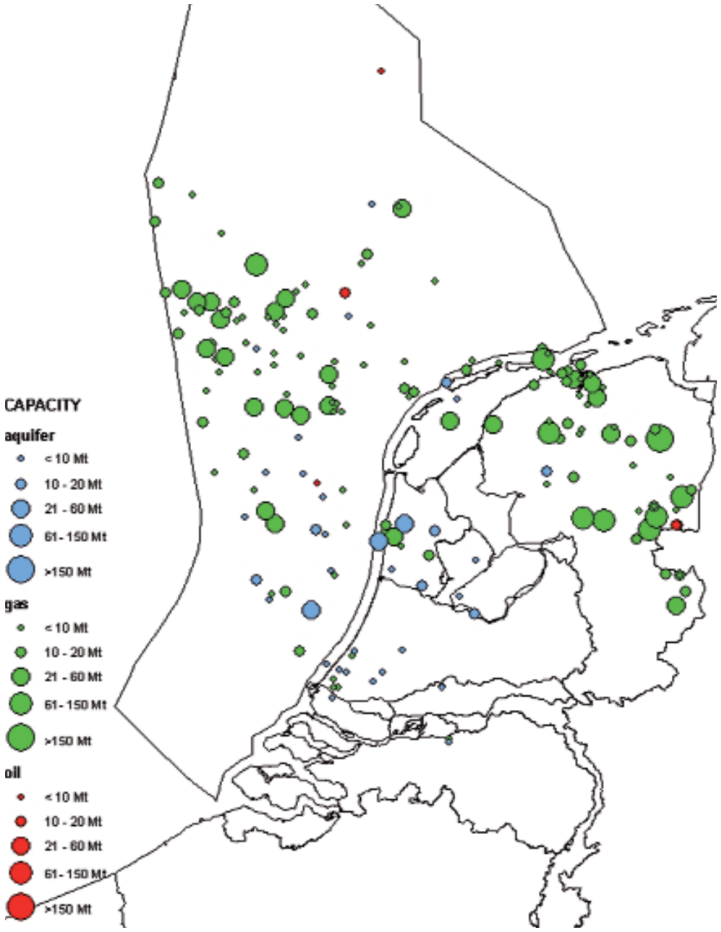

Figure 2.1: Location and storage potential in the Dutch on- and offshore subsurface [22].

The total storage potential of the North Sea fields which is theoretically available is estimated to be 1.7

Gt, comprised of 173 fields [23]. The Dutch government plans to use this potential, by aiming to store 20 Mt per year by 2030 in the subsurface. A great challenge is to qualify the potential of these fields correctly to realise a CCS project. This is dependent on many factors; e.g. the size of the field, the regional geology, the available opportunities for a given depleted gas field to transport the CO_2 to the injection platform. Therefore, precise candidate selection is of utmost importance.

An example of one of the selected candidates is Porthos. This benchmark project in the North Sea plays an important role for future Dutch CCS projects. Porthos is located near the port of Rotterdam and aims to inject 37 Mt CO_2 over a period of 15 years [24]. Due to the revolutionary character of this project, it is handled carefully and many uncertainties are expected. Some of these uncertainties are the containment of the CO_2 in the reservoir and how the reservoir will react on injection of the CO_2, both in far field and near-wellbore regions. Additionally, the chemical and thermodynamic behavior of CO_2 has to be taken in to account, e.g. how does the reservoir react to thermal fractures. Other then operational difficulties, it is also a challenge to monitor the CO_2 after injection.

2.2. Geological setting

The majority of the potential fields in the North Sea are located in the Southern Permian Basin (SPB), a sag basin that formed during the Variscan orogeny. This basin households the two main formations that have been used for gas production; the Rotliegendes and the Buntsandstein formations. The SPB has a complex history of episodic tectonism, changing climates and marine flooding, allowing for different depositional environments that benefit gas entrapment and preservation [19]. It leads to an extensional phase opening the basin from the NE to the SW, allowing for a geological trend in the system from NW to SE. Currently, the basin is tectonically inactive.

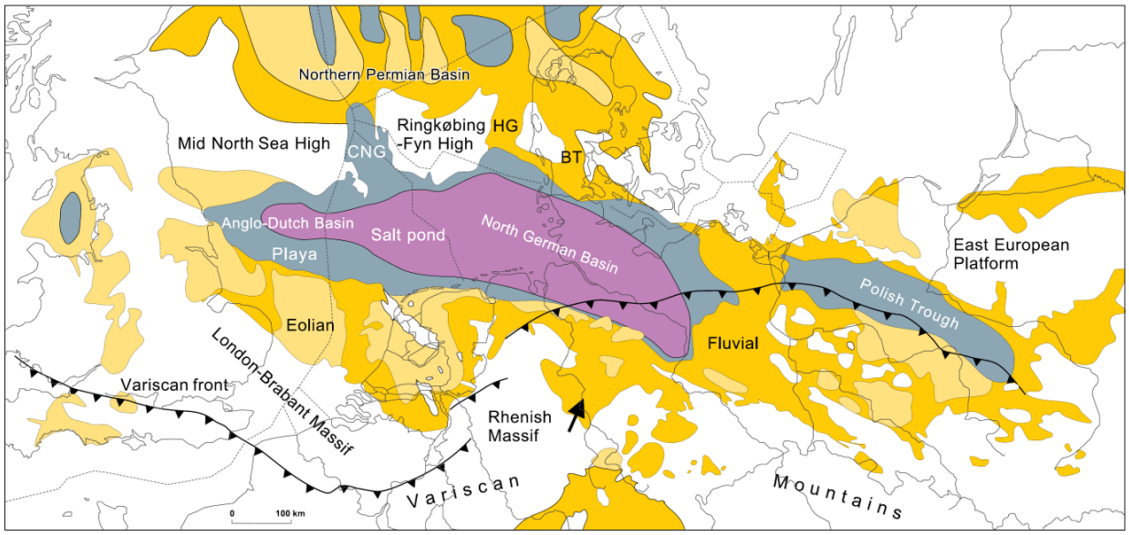

Figure 2.2: Deposition map of the SPB. The Eolian deposits get space for deposition due to Variscan front in the South, allowing the basin to open [25]

The Rotliegendes formation consists in the Netherlands of the Slochteren sandstones, which is an aeolian deposit formed during syn-rift deposition. As the SPB subsided, a lot of accommodation space arose. During this time, the SPB was paleographically closer to the equator, resulting in a warmer and dryer climate. This allowed for the basin to be filled with fine, homogeneous sandstones, with thicknesses up to 350 m. Figure 2.2 shows the infill of the SPB, with mainly aeolian deposits in the Dutch North Sea [25]. The Rotliegendes is overlain with the Zegstein formation after abrupt transgression, which acts as a seal in the form of salts and claystones. Other possible seals are the intra-Rotliegendes shales, or occasionally the Bunter- or Vlieland claystones [20].

The Bundsantstein group, usually addressed as the 'Bunter' sandstone, is a group consisting of multiple formations that formed in the early Triassic in a fluvial setting [20]. The formations present in the North Sea are the Hardegsen, Detfurth and the Volpriehausen formation. They are deposited as post-rift sediments in the SPB. The seal is formed after transgression by the Solling Claystone or the Vlieland Claystone formation.

2.3. Drive mechanisms

The drive mechanisms in a reservoir determine its natural energy. During production of a gas reservoir, it is possible that the loss of energy in the system, the reducing pressures, is repleted by a water drive. This water drive is a result of aquifer support, a connection between the reservoir and the surrounding aquifers [26]. Production that solely uses the energy of the reservoir is better known as primary production. Secondary production would be the production as a result of repressurization.

Primary production induces flow in a reservoir, which allows fluids to expand due to the reduced pressure after production. The three main drives in a natural gas reservoir are a gas expansion (depletion) drive, an aquifer drive or a combination of the two. Dry and wet reservoirs usually exist in single phase while depletion is an isothermal process [26].

When the reservoir is aquifer driven, there is adjoined water aquifers. The pressure differences due to production result in an overflow from the aquifer to the reservoir. If the reservoir is not in connection with an aquifer, the water cannot flow towards the reservoir. A water-driven system has little pressure decline after production and remains close to hydrostatic pressure. According to Figure 2.3, the pressure in an aquifer driven system can be almost fully recovered [18]. This reservoir can be repressurized in three manners, that can be present in a reservoir in combinations; peripheral water drive, edgewater drive and bottomwater drive. Pheripheral water drive means that the reservoir is encircled by an aquifer and is in connection with the reservoir. Edgewater drive is when the reservoir is only connected to an aquifer on an edge, while bottomwater drive solely has a connection to the bottom of the reservoir [26].

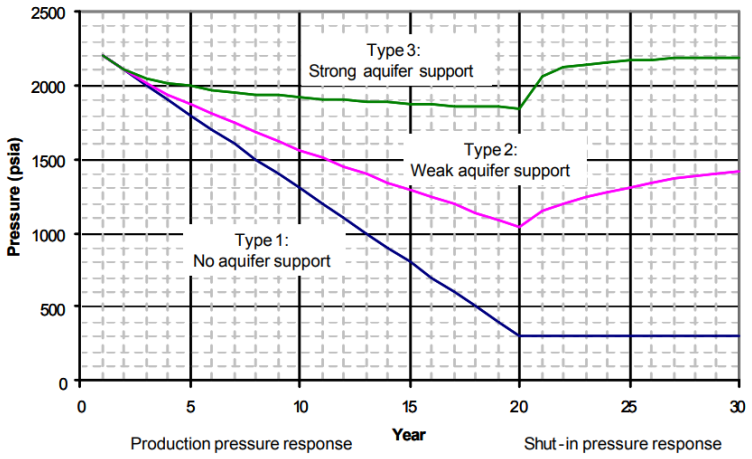

Figure 2.3: Reservoir response after production, for waterdriven and depletion driven reservoirs. [18]

In the case of depleted gasfields, depleted reservoirs are reservoirs with a pressure which is lower than initial pressure. However, since gas is much more compressible than water, a very big and high permeability aquifer is needed to get strong aquifer support, which is usually not the case in the depleted gasfields in the Dutch North Sea. This means that after production, only type 2 or type 1 recovery is expected and the remaining gas and water fill the reservoir by expansion [18].

3
Research Objectives

This research aims to create a better understanding of the geomechanical conditions, behavior and reaction of a depleted reservoir after CO_2 injection. The focus is on thermal fractures. The circumstances in which they initiate and propagate in depleted gas reservoirs is not fully understood yet, together with their impact on the injectivity. A clearer comprehension of the importance of the key geomechanical- reservoir- and operational parameters on thermal fracturing is therefore necessary to broaden the knowledge of the involved processes during CO_2 injection in the near-wellbore region.

3.1. Research questions

To achieve this, the main research question arises:

- **What is the impact of thermal fractures during CO_2 injection in depleted gas fields?**

To find the answer to this question, multiple sub-questions have to be asked to understand how CO_2 acts in the reservoir and how it changes the geomechanical conditions and the thermal behavior, both before and after fracturing:

- How do the thermal fractures initiate?
- How do the thermal fractures propagate into the reservoir?
- How does the injectivity change as a result of thermal fracturing?

The first two sub-questions can be disclosed by answering geomechanical topics:

- How can the state of stress be estimated of a depleted gasfield?
- How does the state of stress change due to cold CO_2 injection?

By answering these questions, the next question is:

- How do fractures impact CO_2 plume and thermal front propagation?

To understand this, a parametric investigation can be conducted on the key parameters, by asking:

- How do the geomechanical parameters influence the impact of thermal fracturing, including:
  - Poisson's ratio [-]
  - Young's Modulus [GPa]
  - Thermal expansion coefficient [1/°C]
  - Biot's coefficient [-]
- How do the reservoir parameters influence the impact of thermal fracturing, including:
  - Permeability [mD]
  - Reservoir thickness [m]
  - depleted reservoir pressure [MPa]

  - Depth [m]
  - Reservoir volume [bcm]

- How do the operational parameters influence the impact of thermal fracturing, including:
  - Injection temperature [°C]
  - Injection rate [kg/s]

By answering these questions, thermal fractures in depleted gasfields can be better characterized. This leads the follow-up question, being:

- What parameters are important to measure to improve the description of thermal fracturing?

The overarching result leads to awareness of the geomechanical reaction of the near-wellbore region during CO_2 injection. This awareness helps improve the description of thermal fractures during CO_2 injection in depleted gasfields in the North Sea, leading to safer operations with reduced uncertainties and an improvement of injection strategy, which subsequently increases the overall quality of the operation.

3.2. Relevance

Changes in injectivity can cause well instability or operational suspense as the injectivity determines the maximum rate of injection to the reservoir and how the reservoir reacts to that rate. In general, an increase of injectivity means the reservoir can handle higher rates, which can be interesting for reservoirs with very low permeability, as thermal fractures would then make the reservoir more suitable for CCS.

However, a negative effect of thermal fractures could be hydrate formation. This is especially relevant for CCS in depleted gasfields, as hydrates form under low pressure (under 50 bar) and temperature conditions [27]. When thermal fractures increase the injectivity, there will be a reduction of the BHP when the injection rate remains constant, which subsequently lowers the bottom hole temperature (BHT). This can cause impermeable hydrate structures to form, which effectively block reservoir pores and the fluid flow within the reservoir, mainly when CO_2 is in two-phase region. This, on its turn, causes a loss of injectivity as they act as barriers to the high permeable sands [27].

The results can also be relevant to make a preliminary estimation of geomechanical instability and seismic reactions. If the thermal fractures reach nearby fault structures, the redirection of the internal angle of friction might cause fault reactivation or compressional fracture initiation [28]. It is also possible that the change of the geomechanical situation might initiate fractures in the caprock. Both fault reactivation and fractures in the caprock can jeopardize the integrity of the caprock, which might cause leakage. By providing a preliminary insight on the impact of thermal fractures in the near-wellbore region, it can give an understanding on what the uncertainties are, subsequently leading to a parametric investigation on for example the geomechanical parameters or a reevaluation of the permeability values, to reduce operational risks and optimize the operation with an improved injection strategy.

3.3. Research outline

The remaining chapters describe how the end product is acquired. Chapter 2 gives background information on what CO_2 sequestration is and in what setting it is investigated in this research. Chapter 4 then describes the physical phenomenons involved and how these phenomenons can be modelled accurately. Chapter 5 then describes how the model is defined and initialized, to model the results for the research. These results are then used to generate a discussion, to link the results to the expected results based on chapter 2, chapter 4, chapter 5 and to other research which subsequently leads to an insight on the impact of thermal fracturing in the near-wellbore region in CO_2 sequestration projects in depleted gas fields. Lastly, the finding are concluded in chapter 8.

4

Methodology

4.1. CO_2 phase behavior and thermodynamic properties

For CO_2 sequestration projects, it is preferred to inject the CO_2 in supercritical state. This allows for much denser and thus more efficient injection [29]. Thereby, it is expected that the substance has up to 95% purity or higher, because the CO_2 is usually purified at the surface before injection [18]. However, it is important to realise that CO_2 is not in single phase condition inside the reservoir. In the reservoir, the remaining hydrocarbons create a multicomponent system with the CO_2. After CO_2, methane has the largest mole fraction. The phase behavior of a component is dependent on its internal energy. The internal energy defines how the system thermodynamically behaves and is a function of entropy and volume [30]

$$\Delta U = TdS - PdV \tag{4.1}$$

where T is temperature, dS the change in entropy, P pressure and dV the change in volume. When multiple components are present, each component contributes to the function of phase behavior. Figure 4.1 showcases a PT diagram of different CO_2-CH_4 mixtures [31] and a Px diagram with different temperatures. Figure 4.1a shows that the critical point of CO_2 lies on higher temperatures and lower pressure with higher CO_2 mole fraction, meaning that the two phase region is reached faster for purer CO_2 mixtures when a reservoir is cooled.
With CO_2 injection in depleted gasfields, the pressure at the start of operation can be as low as 20 bar. In the near-wellbore region, the CO_2 mole fraction behind the CO_2 front will be close to pure, reaching the critical point at around 30 °C. This means that supercritical state in the near-wellbore area will be reached once the pressure reaches above 80 bar. In front of the CO_2 plume the mole fraction will be lower, reaching the critical point at lower temperatures and on higher pressures. This means that different parts of the reservoir reach the two-phase region during injection while the CO_2 plume propagates through the reservoir.

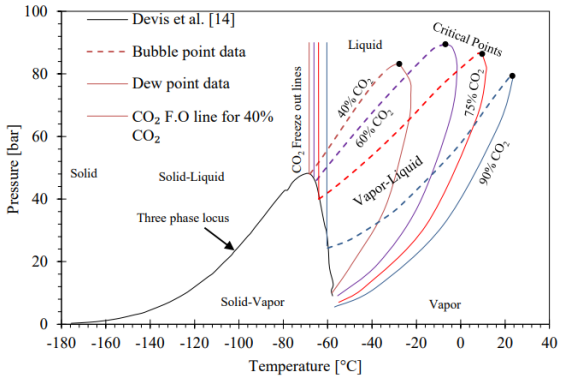

(a) PT diagram for CO_2-CH_4 binary system with different concentrations

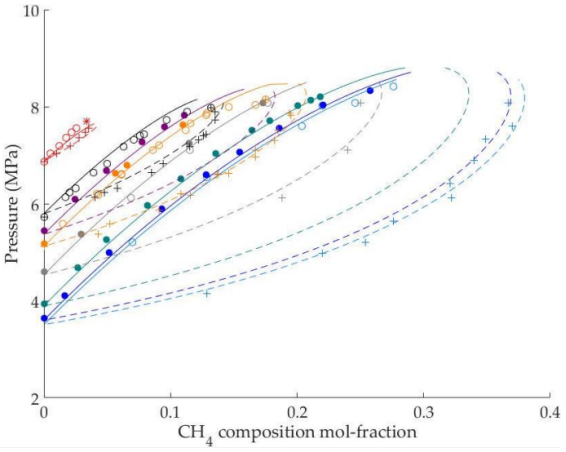

(b) Px diagram for CO_2-CH_4 binary system with different temperatures, from 273.15 (cyan line) to 301 K (red line).

Figure 4.1: PT and Px diagram for a binary system containing CO_2 and CH_4 [31, 32].

The other diagram (Figure 4.1b) shows that the bubble points are reached on higher pressures with increasing temperatures [32]. It supports Figure 4.1a, showing that the two-phase region increases in size with decreasing temperatures. This is because the critical point shifts towards higher CH_4 mole fraction, increasing the pressure range in which two-phase conditions form. For depleted gasfields this means that when injecting with low temperatures, two-phase can be expected inside the reservoir while the pressure builds up.
The phase behavior has a great impact on the properties of CO_2. Figure 4.2 illustrates the effect different phases have on the density and the viscosity for a binary mixture of 94% CO_2. With an increasing pressure and with varying temperatures, the CO_2's density and viscosity changes significantly. Figure 4.2a shows that there is a steep increase in density when the pressure reaches 70 bar for 40 to 80 °C. A similar effect is visible for the viscosity of CO_2, where Figure 4.2b shows that the gradient of speed of sound reduces with increased pressure, and lies lower for higher temperatures. This means that there is a shift of phases at the start of the curve, which reduces the increase of the speed of sound as it would travel the fastest in denser or more viscous mixtures [33]. Translating this information to CO_2 injection, the changes in the thermodynamic properties can have a great influence on CO_2 propagation, especially close to the well.

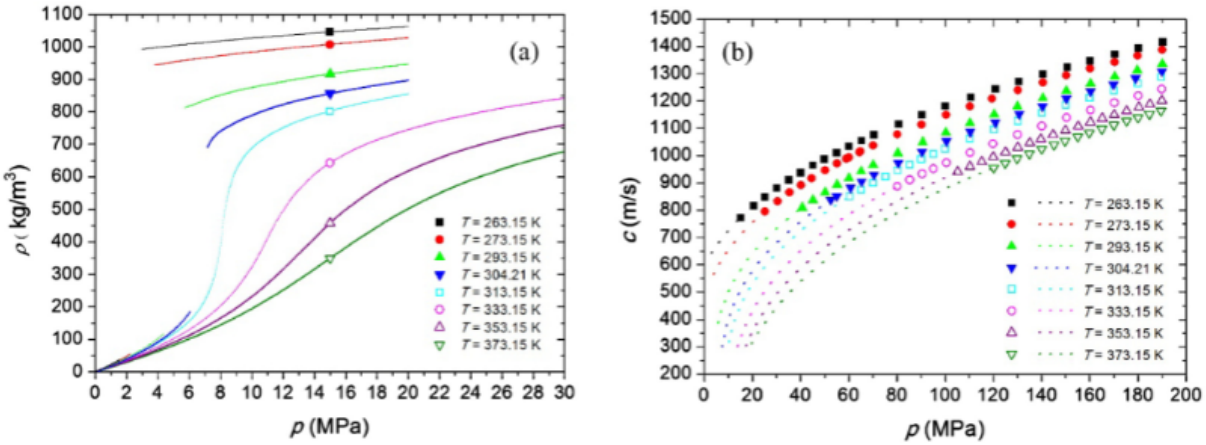

Figure 4.2: a: Density of a 94% CO_2 binary mixture with increasing pressure and temperature [33]. b: Speed of sound changes in a binary CO_2 - CH_4 system with increasing pressure. A higher speed of sound means that the binary system is more viscous.

4.2. Near-wellbore effects

The near-wellbore (NWB) effects include all alterations to the system close to the well that are caused due to injection of CO_2. Figure 4.3 includes an overview of the main processes around a wellbore [34]. These effects have an impact on the geochemical, geomechanical and thermal state of a reservoir and thus ultimately on flow characteristics, CO_2 containment and the temperature profile. The effects provide feedback on each other, e.g. mineral precipitation will have an impact on the flow characteristics, which subsequently as an impact on the geomechanical state of the reservoir. There are some additional effects such as exothermic CO_2 dissolution or endothermic water vaporization [13] which are left out in Figure 4.3 as they are not solely effecting the NWB region. This research only focuses on the thermal and geomechanical effects and their relationship during CO_2 injection. This section defines the thermal effects, while the geomechanical effects are extensively discussed in section 4.4.

4.2.1. Joule-Thomson effect

The Joule-Thomson effect (JTE) or Joule-Thomson Cooling (JTC) is an effect that causes additional cooling of the reservoir, other than heat diffusion and advection. JTC is a result of adiabatic pressure decrease. This phenomenon is a result of a sudden increase of volume, allowing a growing distance between molecules, which, due to the vanderwaals forces, results in a sudden increase in potential energy [35]. This sudden increase can be expected during injection in a depleted gasfield, where a low reservoir pressure acts as a pressure release compared to the higher bottomhole pressures caused by the preferred injection rate. As it is an adiabatic system, meaning that no heat is lost in this process, the increase in potential energy means that the kinetic energy drops for a ideal gas, according to

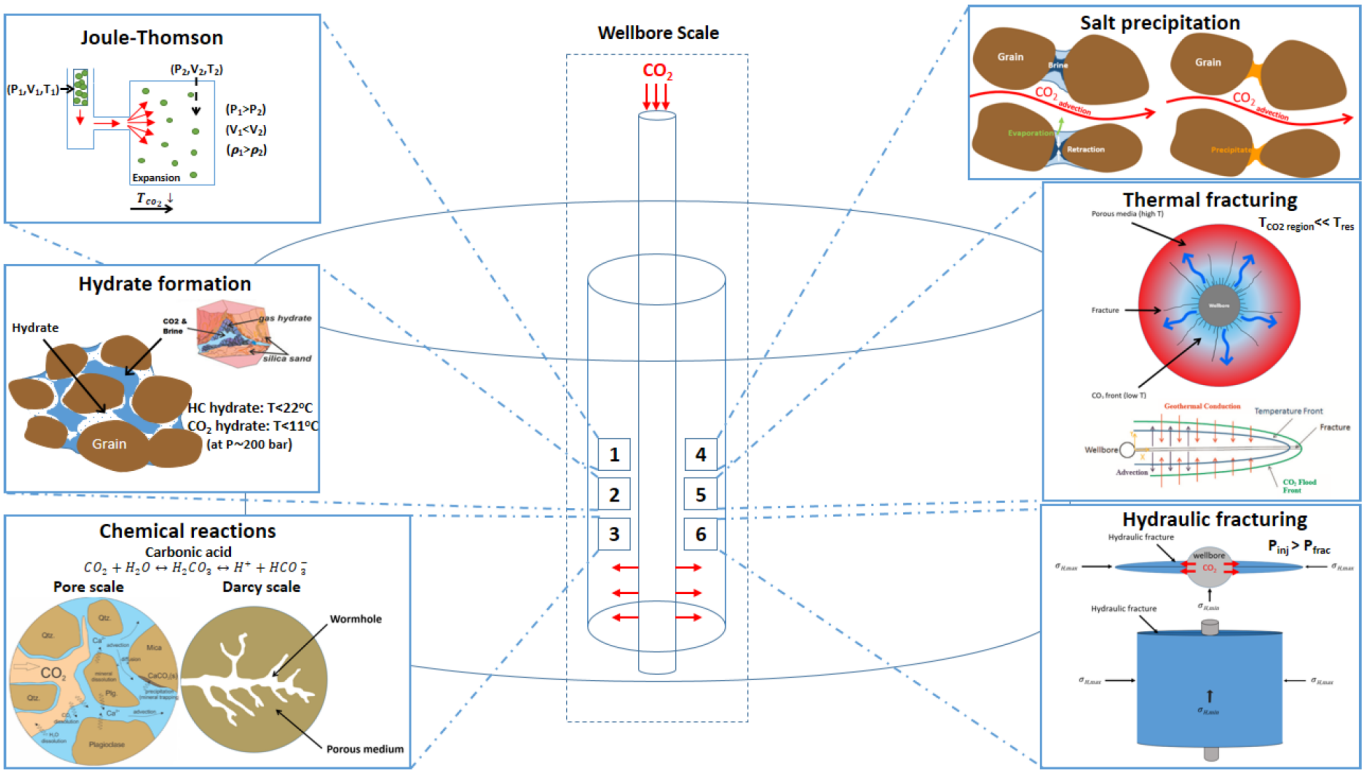

Figure 4.3: Near-wellbore effects as a result of CO_2 injection [34].

Equation 4.2

$$dw = \Delta U = p_1 V_1 - p_2 V_2 \tag{4.2}$$

where dw is the change in work, ΔU the change in internal energy, p pressure and V volume. However, CO_2 is not an ideal gas, giving a change of enthalpy as

$$\Delta H = \Delta U + \Delta(pV) \tag{4.3}$$

Implementing Equation 4.3 in to Equation 4.2 gives a $\Delta H = 0$, meaning JTE is at constant enthalpy. From experiments it is observed that a Joule-Thomson coefficient (μ_{JT}) can be found, which shows a linear relationship between the drop in pressure and the drop in temperature due to the JTE

$$\frac{\Delta T}{\Delta P} \approx \left(\frac{\partial T}{\partial P}\right) = \mu_{JT} \tag{4.4}$$

A positive μ_{JT} means that the system cools, with a higher coefficient resulting in more cooling. The JT coefficient varies strongly for different substances and is highly depended on initial surface temperature and the expansion pressure. Figure 4.4 shows the μ_{JT} of CO_2 and methane with increasing pressure for different temperatures [36]. It can be seen that when the CO_2 is in the gaseous phase at lower pressures and temperatures, the μ_{JT} is significantly higher than methane's gaseous phase. However, once the temperature and pressure is increased, the CO_2 enters dense or supercritical state, which have a much lower μ_{JT} than gaseous methane. Thus, the JTC will be less intensive with injection of denser/liquid CO_2. However, injection in depleted gas reservoirs means high pressure differences, and thus a potential shift towards the gas phase at the start of injection, which allows for more extensive cooling [34].

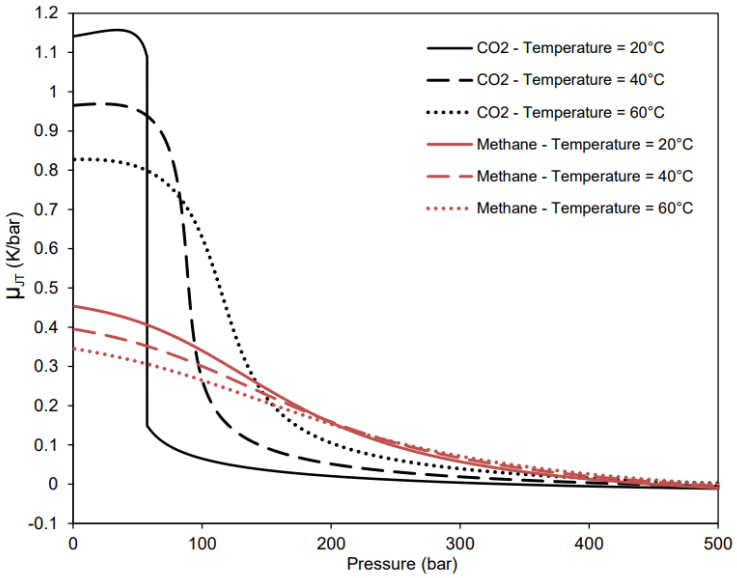

Figure 4.4: Joule-Thomson coefficient for CO_2 and CH_4 for different temperatures over increasing pressure [36].

This shows that injecting in tight, low permeability reservoirs in depleted conditions where CO_2 slowly propagates through the reservoir, cause the highest μ_{JT}, resulting in intense cooling with CO_2 propagation [35]. The cooling effect in the near-wellbore region is not exactly the same as JTC, as it is not a fully adiabatic system, but are often described similarly. The cooling in the NWB region can be better described as expansion cooling [37]. This cooling effect will decrease with increasing reservoir pressure, as the pressure difference between the well and the reservoir reduces.

4.3. Governing equations

The Equation of State (EOS) in a reservoir is the relation between the pressure, volume and temperature (PVT) over time, The EOS can be defined by the governing equations. CO_2 storage involves the solution of the component transport equations, the equations for thermodynamic equilibrium between the gas and aqueous phase and the equations for geochemistry [38]. This section defines the relations between the multiple components for a CO_2 storage fully-coupled geochemical EOS compositional simulator. The PVT relation then can be coupled to the geomechanic effects due to cold CO_2 injection.

4.3.1. Equation of state

This research uses the EOS calculation based on the approach of Peng Robinson (PR). This is a cubic EOS, which allows to find the vapor-liquid equilibrium in a system [39]. This approach makes use of two constants, the attraction (a) and the repulsion (b) parameters. These can be defined by experimental data. The PR EOS reads

$$P = \frac{RT}{V_m - b} - \frac{aT}{V_m^2 + 2bV_m - b^2} \tag{4.5}$$

in which R is the universal gas constant, V_m the molar mass and T the temperature. This allows you to find the relation between P, T and V_m using the critical temperature and pressure of a gas (T_{crit} and P_{crit}), which are defined as constants as

$$a = 0.45724 \frac{R^2 T_{crit}^2}{P_{crit}} \tag{4.6}$$

and

$$b = 0.07780 \frac{RT_{crit}}{P_c rit} \tag{4.7}$$

This definition of a and b is for pure substances only. In case of mixtures, the van der Waals mixing rules apply to these constants [40]. For a, this can be defined as

$$a = \sum_{i,j} z_i z_j \sqrt{a_i a_j}(1 - k_{ij}) \tag{4.8}$$

and

$$\sum_i x_i b_i \tag{4.9}$$

where z_i and z_j are the mole fraction of each component, a_i and a_j the attraction constants of each component and k_{ij} is the binary interaction parameter.

4.3.2. Mass balance equation

Darcy's law governs the flow in the reservoir with multiple components. The multi-phase flow can be defined by the transport of a component over time. The components in a CO_2 sequestration project are considered immiscible, according to Nghiem et al. [41]. The mass conservation equation for one component in phase a [42] can be defined as

$$\frac{\partial(S_a \phi \rho_a)}{\partial t} = \nabla \cdot (\rho_a v_a) + Q \tag{4.10}$$

where S_a, ϕ, ρ and ∂t are the saturation of phase a, the porosity, the density of phase a and the time-step over which it is calculated respectively. The first term describes the volume of phase a. This is equal to the vector of the flow rate velocity, v, times the density together with the rate of the source term, Q. The velocity of a component can be described as

$$v_a = -\frac{k_{r,a} K}{\mu_a}(\nabla P_a - \rho_a g \nabla z) \tag{4.11}$$

This equation consists of the relative permeability (k_r) of the phase, the rock permeability (K), the viscosity (μ) and the pressure and height differences (∇P and ∇z, respectively). Combining Equation 4.10 and Equation 4.11 together and calculating them for all the components, leads to

$$\sum_{a=1}^{N_p} \frac{\partial(S_a \phi \rho_a x_{i,a})}{\partial t} = \nabla \cdot \left[\sum_{a=1}^{N_p} \rho_a x_{ia} \frac{k_{r,a} K}{\mu_a}(\nabla P_a - \rho_a g \nabla z) \right] + Q_i \qquad i = 1, \cdots, N_c \tag{4.12}$$

Here, the transport of a component (N_p) is summed for ∂t, using its mole fraction (x_i), where i defines a component, with the total number of components being N_c. As mass conservation is assumed, the total saturation is considered to be

$$S_w + S_g = 1 \tag{4.13}$$

where S_w (water saturation) is defined as

$$S_w = \frac{N_{n_c+1}}{\phi \rho_w} \tag{4.14}$$

which translates to a summation of all the components as follows

$$\sum_{i=1}^{N_c} S_{i\alpha} \qquad i = 1, \cdots, N_c \tag{4.15}$$

The same applies to the mole fraction of each component;

$$\sum_{i=1}^{N_c} x_{i\alpha} \qquad i = 1, \cdots, N_c \tag{4.16}$$

This way, the molar volume (V) consistency can be equated as in Equation 4.17

$$V\frac{\sum_{i=1}^{n_c+1} N_i^{n+1}}{(\rho_g S_g + \rho_w S_w)^{n+1}} - V\phi^{n+1} = 0 \tag{4.17}$$

where the first term is the volume occupied by the fluids and the second term is the pore volume, resulting in consistency between them.

4.3.3. Energy balance equations

The Energy balance equation is a Darcy flow based expression of the mass balance equation configured to translate the energy and thus the temperature in a system. By modifying each term of Equation 4.10 to also include its energy output for each phase, one finds the energy balance equation as

$$\sum_{a=1}^{N_p} \frac{\partial(S_a\phi\rho_a U_a) + (1-\phi)C_r(\Delta T)}{\partial t} = \nabla\cdot\left[\sum_{a=1}^{N_p}\rho_a H_a v_a\right] + \sum_{a=1}^{N_p}(H_a Q_a) \tag{4.18}$$

where C_r is the heat capacity of the rock, ΔT the temperature change and H_a and U_a are the enthalpy and the internal energy of phase a.

4.3.4. Thermodynamic equilibrium

The thermodynamic equilibrium is a physical rule where thermodynamic system must be in equilibrium between the phases [38]. This can be done by mass transfer, where the fugacity of each phase must be equal to ensure equilibrium. For N_c number of components, this can be described as

$$f_{ig} - f_{iw} = 0, i = 1, \cdots, N_c \tag{4.19}$$

where f_{ig} and f_{iw} are the fugacity of component i in the gas phase and in the aqueous phase, respectively. In CO_2 sequestration, the gas is considered to be a multicomponent mixture. the fugacity of the gaseous phase is calculated from an equation of state (EOS), such as Peng Robinson, whereas the f_{iw} is calculated using Henry's law, which is defined as

$$f_{iw} = x_{iw}\cdot H_i \tag{4.20}$$

where x_{iw} is the mole fraction of component i and H_i being Henry's constant. This constant is a function of pressure, temperature and salinity. to calculate the Henry's constant one must solve

$$ln[H_i] = ln[H_i]* + \frac{\overline{V_m}(P - P*)}{RT} \tag{4.21}$$

in which H_i* is the Henry's constant for component i at reference pressure P_i* and $\overline{V_m}$ is the partial molar volume of component i. This assumes that the temperature and salinity do not change significantly throughout the reservoir and that a representative value for temperature and salinity could be used to calculate Henry's constant [38].

4.3.5. Matrix-fracture interaction

In case of fractured reservoirs, the interaction between the matrix and fracture must be taken in to account when formulating the mass balance equation. As both the fracture and matrix participate in the flow and heat transfer, each transfer between the two are considered, being; matrix-matrix flow, matrix-fracture flow and fracture-fracture flow [43]. The flow between the fracture and the matrix for a component in phase a reads

$$\tau = \Sigma_p\rho_a\frac{k_{r,a}K}{\mu_a}x_a(p_m - p_f) \tag{4.22}$$

where $p_m - p_f$ is the difference in pressure between the fracture and the matrix and Σ_p is a transmissibility factor and is a representation of the transmissibility between the fracture and the matrix combined with a shape factor. The shape factor can be calculated with

$$\Sigma_p = 4V_b \sum_i \frac{k^*_{mi}}{L_i^2} \tag{4.23}$$

where L_i is the fracture spacing, k^*_{mi} is the effective matrix permeability in all directions for component i and V_b is the reference volume. Using Equation 4.22 and 4.23, Equation 4.12 can be modified to include the mass balance equation for fracture

$$\left[\sum_{a=1}^{N_p} \frac{\partial(S_a \phi \rho_a x_{i,a})}{\partial t} - Q_i\right]_f = \nabla \cdot \left[\sum_{a=1}^{N_p} [\rho_a x_{ia} v_{ia}]_f\right] + \tau \qquad i = 1, \cdots, N_c \tag{4.24}$$

and for matrix

$$\left[\sum_{a=1}^{N_p} \frac{\partial(S_a \phi \rho_a x_{i,a})}{\partial t} - Q_i\right]_f = \nabla \cdot \left[\sum_{a=1}^{N_p} [\rho_a x_{ia} v_{ia}]_m\right] - \tau \qquad i = 1, \cdots, N_c \tag{4.25}$$

4.3.6. Injector well model

A well model is necessary to formulate under which conditions the injected substance will enter the reservoir model. It relates the injection rate to the pressure in the reservoir and the BHP. This is defined by the Peaceman equation, which can be written as

$$Q_i = WI \frac{k_{r,a} K}{\mu_a} (P_{BHP} - P_{res}), \qquad i = g, w \tag{4.26}$$

with $P_{BHP} > P_{res}$, otherwise there is no overpressure to make injection happen. The WI is the Well Injectivity index, a term that describes the ability of a well to receive injected substances. A higher WI means that a reservoir is able to receive more injected fluids over a time period. This is dependent on the well geometry and the geometry of the drainage circle:

$$WI = 2\pi ff kh \frac{w_{frac}}{ln(r_e/r_w) + S} \tag{4.27}$$

where ff is the fraction of completion, k the effective permeability, h is thickness, w_{frac} is the well fraction governed by areal geometry, r_d the drainage radius, r_w the well radius, r_e the effective radius of the well and S is the skin factor [38]. The effective well radius can be found with

$$r_e = CC\sqrt{A/w_{frac}} \tag{4.28}$$

in which CC is the geometric factor and A the area of the grid-block. This means that the well index is heavily dependent on the defined grid-block dimensions, which makes WI a unreliable expression to compare different models with each other, only if the models share similar gridding dimensions.

4.4. Geomechanics

The geomechanics of a reservoir system are defined by the principal state of stress. The stress is a tensor (S) composed of three principal vectors in three directions, assuming a fully elastic, homogeneous and isotropic system; S_1, S_2 and S_3. These are the total stresses in each principal direction (Figure 4.5). The stress tensor defines the stress regime in a reservoir. The largest stress acts on the plane perpendicular to the vertical direction, which is usually defined as S_1, while S_2 is the second largest stress vector and S_3 the smallest. These are the eigenvalues of the principal stress directions:

$$S = \begin{bmatrix} S_1 & 0 & 0 \\ 0 & S_2 & 0 \\ 0 & 0 & S_3 \end{bmatrix} \tag{4.29}$$

The zeros represent the shear stresses, the stresses that work on the surfaces (Figure 4.5). In a reservoir, S_1, S_2 and S_3 are assigned to the vertical, horizontal maximum and the horizontal minimum

stress (the $S_{vertical}$, $S^{max}_{horizontal}$ and $S^{min}_{horizontal}$ respectively). A different distribution of the maximum stress directions cause different stress regimes. According to Anderson's theory of faulting [28], this can lead to a normal faulting regime, thrust faulting regime or a strike slip regime (Figure 4.5).

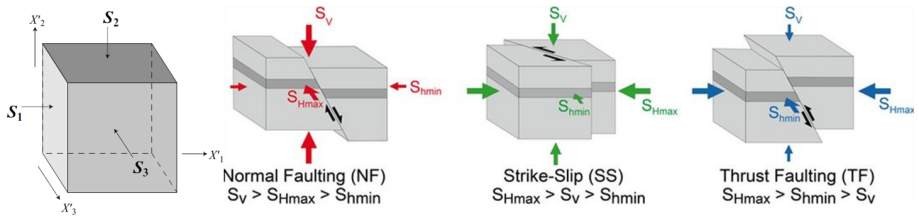

Figure 4.5: Anderson's theory of faulting, showing the influence of the distribution of stresses in the subsurface [28]

.

Equation 4.30 shows how the stress in each direction is defined. The total stress (S_i) consists of the effective stress (σ), which is the stress applied to the body of the rock by the surrounding rocks, together with stress inside the rock, which is caused by the pressure inside the pores (σ^p):

$$S_i = \sigma_i + \sigma^p \tag{4.30}$$

The pore pressure in a reservoir is a dynamic parameter in time and space. In reservoir engineering, the pore pressure is affected by injection and production during the operation window. The effective state of stress in a reservoir is also defined in three main directions. σ_v is the vertical component caused by the overlying rocks, the overburden. This can be calculated by Equation 4.31,

$$S_v = \int_0^Z \rho g z \, dz \tag{4.31}$$

where ρ is the density of the overburden at a certain depth, z the depth of the reservoir and g the gravitational constant. The horizontal component of the stress tensor is defined by the maximum and minimum horizontal state of stress. The horizontal component can be calculated based on σ_v (Equation 4.32)

$$\sigma_h = \frac{\nu}{1-\nu}\sigma_v + \mathrm{T} \tag{4.32}$$

where ν is the Poisson's ratio, a rock property that describes how much elongation happens perpendicular on the loading direction of the rock. T is a stress vector that indicates the tectonic component, giving a directional addition to either the σ_h^{max} and the σ_h^{min} based on the tectonic activity.

4.4.1. Thermoporoelasticity

The state of stress can be influenced by processes in the reservoir. The total stress changes due to pressure and temperature changes. The effect these together have on the overall stress is called the thermoporoelastic response of the reservoir and can be used as a generalized theorem as to why the stress conditions change during operation [28].

Poroelastic stress

The poroelastic response is the response the pores have on the reservoir rocks due to either changing volumes of the rock or due to changing pore pressure. Thus, when a volume shrinks, the pores execute an enhanced stress on the reservoir rock. This can cause deformation. By increasing the P during injection, the pores produce higher forces on the reservoir rock. The effect of poroelasticity on the state of stress can be described as in Equation 4.33. In this equation, α is the Biot coefficient and $\Delta\sigma^P$ is the change in stress due to the poroelastic effect [44].

$$\Delta\sigma^P = \alpha \Delta P \tag{4.33}$$

The Biot coefficient is an empirically found parameter that describes the fluid volume change induced by bulk volume changes in the drained condition, as seen in Equation 4.34

$$\alpha = 1 - \frac{K_D}{K_s} \tag{4.34}$$

where K_D is the compression modulus of the drained porous rock and K_s of the non-porous solid. For sands, α is close to 1 and for rocks α can be as low as 0.7 [28].

Thermoelastic stress

The thermoelastic response is the reaction of a rock body on the changes in temperature. A change in temperature leads to dilation or contraction of a rock, in which contraction is caused by cooling and causes a decrease in stress and for dilation vise versa [17]. However, for a body that is in steady-state, the analytical solution for an uniform temperature decrease with one-dimensional vertical strain and constant vertical stress with no change in pore pressure [17] equals

$$\Delta\sigma^T = \frac{E\alpha_T\Delta T}{1-\nu} \tag{4.35}$$

where α_T is the measured linear thermal expansion coefficient, ΔT the temperature difference between the injected fluid and the reservoir conditions and E the Young's modulus. The Young's modulus, or the elastic modulus of the rock, describes the tensile or compressive stiffness of a rock by quantifying the relationship between stress and strain. α_T defines the change in length due to temperature change [28], according to

$$\alpha_T = \frac{\Delta L}{L\Delta T} \tag{4.36}$$

where L is the length of the body. Considering Equation 4.33 and Equation 4.35 a more detailed version of Equation 4.30 can be written down as

$$S = \sigma + \sigma^P + \Delta\sigma^P + \Delta\sigma^T \tag{4.37}$$

4.4.2. Thermoelastic adjustment factor

As α_T is the linear thermal expansion coefficient, it assumes a one dimensional expansion. The temperature front in the reservoir, however, propagates in a cylindrical to elliptic shape. Equation 4.35 assumes homogeneous isotropic cooling. In reality, the thermal front forms a cold and hot zone, with a transition zone in between. This causes the different zones to pull at each other, as they each have different compressional and tensional forces [45]. To account for this effect, the thermoelastic solution looks like

$$\Delta\sigma^T = f_{adj}\frac{E}{(1-\nu)}\alpha_T\Delta T \tag{4.38}$$

where f_{adj} is the adjustment factor. This adjustment factor can range from 0.5 to 1, based on the distance of the thermal front. If the ratio of the reservoir thickness (h) and the diameter (d) of the thermal front, better known as d/h, reaches towards infinity, f_{adj} becomes close to 1. When d/h is lower than 1, f_{adj} is close to 0.5 [45]. A numerical approximation, calculated by Perkins and Gonzalez [45], finds that the f_{adj} can be given by

$$f_{adj} = \frac{(1-\nu)}{E\alpha_T}\Delta\sigma = 0.5\left[1 + \frac{1}{1 + 1.45(\frac{h}{d})^{0.9} + 0.35(\frac{h}{d})^2}\right] \tag{4.39}$$

Figure 4.6 includes the outcome of Equation 4.39 for a d/h ranging from 0.001 to 1000. In practice, the disc shape typically has a ratio of 0.1 to 6, which means that the adjustment factor would range between 0.5 and 0.9 over the project lifetime. The adjustment factor can be found when the depleted state of stress, the thermo- and poroelastic effect and the stress conditions after injection are known;

$$f_{adj} = \frac{\sigma - \sigma_{depl} - \Delta\sigma^P}{\Delta\sigma^T} \tag{4.40}$$

where σ_{depl} are the effective stress conditions at depleted state and σ the effective stress conditions after injection.

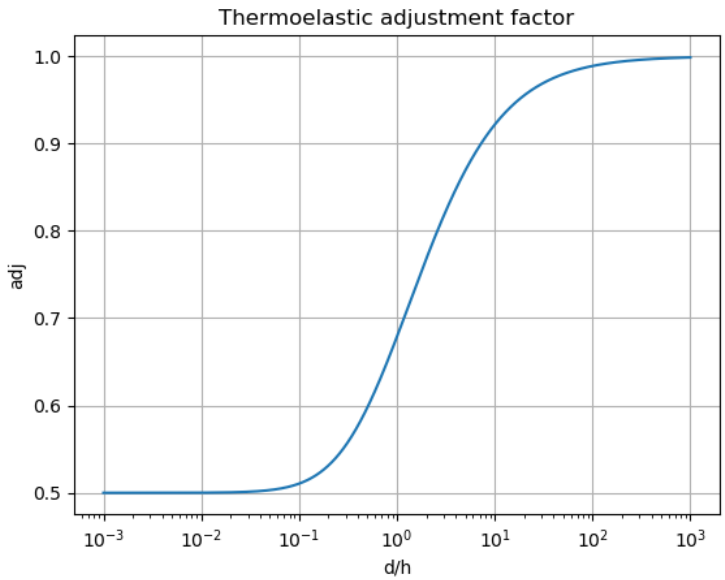

Figure 4.6: Adjustment factor for a d/h of 0.001 to 1000.

4.4.3. Stress conditions in a depleted gas field

A depleted gas field is a result of gas production, which lowered the pore pressure in the reservoir significantly. The relation between the vertical and horizontal stress can be expressed as a ratio, being

$$\mathrm{K}_0 = \frac{S_h}{S_v} \tag{4.41}$$

and for the effective stress

$$\mathrm{K}'_0 = \frac{\sigma_h}{\sigma_v} \tag{4.42}$$

where K_0 and K'_0 are the ratios between the vertical and horizontal total and effective stress at virgin reservoir conditions. Equation 4.32 shows that the relation between the vertical and horizontal effective stress can also be described as $\mathrm{K}'_0 = \frac{\nu}{1-\nu}$. The relation between the effective stress and pore pressure change due to depletion can be expressed as a constant, namely the arching constant or the depletion constant (γ). This constant can be found for the vertical and horizontal stress:

$$\gamma_v = \frac{\Delta S_v}{\Delta P}, \qquad \gamma_h = \frac{\Delta S_h}{\Delta P} \tag{4.43}$$

Assuming that the depleted gas reservoir is large enough that the change in vertical stress can be spread over the horizontal interval, ΔS_v is constant and thus equal to zero. However, the horizontal arching constant can also be found [46] using:

$$\gamma_h = \alpha \frac{1-2\nu}{1-\nu} \tag{4.44}$$

This means, by combining Equation 4.43 and Equation 4.44, that the change in horizontal stress can be found with

$$\Delta S_h = \alpha \frac{1-2\nu}{1-\nu} \Delta P \tag{4.45}$$

with a change in stress being

$$\Delta\sigma_h = (\alpha - \gamma_h)\Delta P \tag{4.46}$$

In this manner, the change in vertical and horizontal stress can be calculated for a field that has been depleted. This, however, assumes a constant temperature over time during production. Combining the previous equations gives us

$$S_h^{depleted} = S_h^{initial} + \Delta S_h \tag{4.47}$$

$$\sigma_h^{depleted} = \sigma_h^{initial} + \Delta\sigma_h \tag{4.48}$$

where $S_h^{depleted}$ and $\sigma_h^{depleted}$ is the total and effective minimum stress in a gas field after depletion.

4.4.4. Mohr-Coulomb theory and fracture initiation

Now the stress regime in a depleted gasfield is understood, it can be placed in context with fracture initiation in the reservoir. A widely known way of picturing the state of stress in the reservoir rock and its failure criterion is the Mohr coulomb criterion. The Mohr circle is a 2D representation of the largest and smallest principal stresses, the σ_1 and σ_3. Whenever the stresses change, the circle rearranges itself by changing its diameter or its position. On the Mohr-Coulomb diagram the circle is accompanied by the Mohr-Coulomb failure criterion, which is defined by

$$\tau = C + \sigma_n tan\phi \tag{4.49}$$

where C is the cohesion, a rock parameter that represents the shear strength of a rock, ϕ is the angle of internal friction, which is a correction for the shear force acting on a body. σ_n is the normal stress on the principal stress directions. When the Mohr circle moves towards a position where it intersects the failure criterion, the rock will break on the angle on which the circle hits the failure line. However, when the circle is not large enough to hit the failure line before the failure line's origin, it will break without an angle of internal friction. Figure 4.7 illustrates the different types of fractures that can be initiated by intersecting the failure line. Once the circle reaches the failure line on an angle in the compressional regime, it breaks as a mode II fracture. If the rock breaks without being on an angle, it means that the stress working on the rock is zero or below, meaning there is negative compression on the rock, better known as tension. This leads to extensional fractures, better known as mode I fractures [47]. Mode I fractures always initiate and propagate perpendicular on the direction of the minimum principal stress. A hybrid fracture is a transition phase between extension and shear fractures, in which fractures form under mixed tensile and compressive stress states [48].

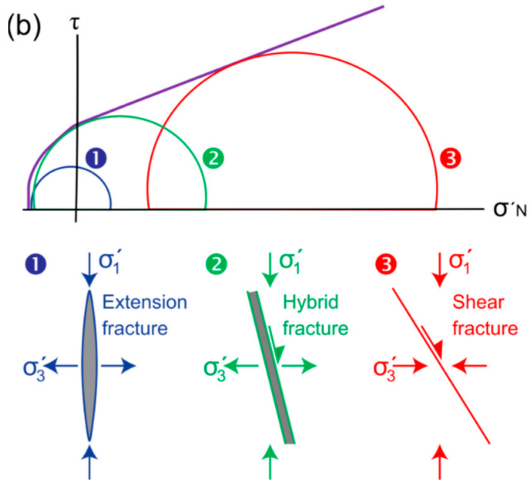

Figure 4.7: Mohr diagram showing different fields where extensional (mode I), hybrid and compressional/shear (mode II) fractures initiate [47].

Figure 4.8 illustrates the schematic change of stress due to poroelastic effects during depletion and injection depicted by the Mohr circle. Following the above equations, the Mohr circle shifts towards the

right while increasing in diameter during depletion. During injection, Figure 4.8 illustrates the separate and combined effect of the poroelastic and thermoelastic responses on the Mohr circle. These effects combined result in fracture initiation.
In case of deeply buried reservoirs, the rock strength is fairly large and the direction of the principal plane of stress is aligned with the principal stresses, resulting in an angle of internal friction of 0. This means that there are no shear stresses working on the surfaces. The failure envelope is only reached on the x-axis, in the tensional regime. The tensional regime results in mode I fractures, which usually is the case for thermal fracture initiation [28]. When a reservoir remains in isothermal conditions and fractures solely due to the poroelastic effect, it is called a hydraulic fracture. However, when there is a presence of faults in the reservoir, they can act as a stress plane, redirecting the principal stresses. This can cause an internal angle of fraction and thus shear stresses on the rock surface [28]. This, in its turn, can lead to fractures to initiate or can reactivate fault activity.

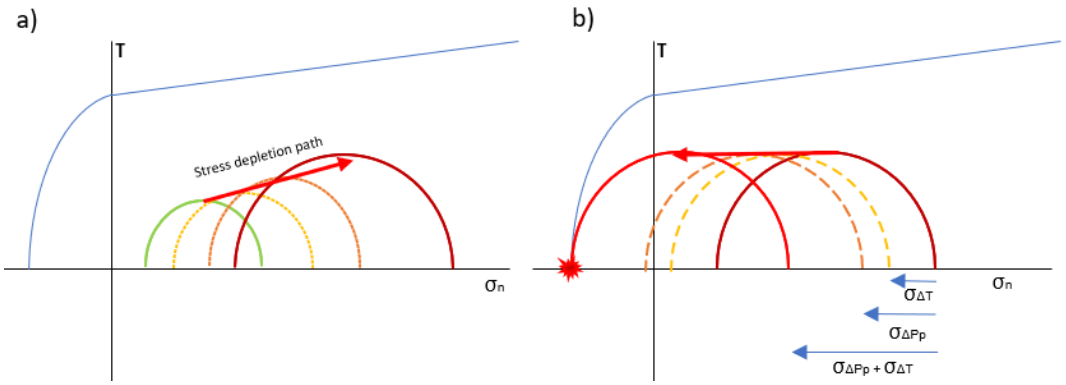

Figure 4.8: Change of stress after depletion and injection. The y-axis shows the shear stress, the x-axis the normal stress. a: Depletion of a gasfield. b: Injection in a depleted gasfield changes the Mohr Coulomb diagram due to thermoporoelastic effects, until tensional/thermal fracture initiation.

4.4.5. Depletion and injection constant

Strain hardening is an effect that is caused by plastic deformation that occurs during depletion. It means that the rocks are not perfectly elastic, and thus do not follow the same stress path during injection as with depletion [49]. This means that the manner in which the stress conditions change due to the thermoporoelastic effect, the depletion constant γ_h, changes during injection in to a injection coefficient [50]. The injection constant has a lower value then the depletion constant due to hysteresis, meaning that injection causes a faster drop of σ_h^{min} during injection.

4.5. Numerical Methods

4.5.1. CMG GEM

The reservoir simulation software that is used to model the impact of thermal fracturing in a depleted gas field is developed by Computer Modelling Group Ltd. (CMG). This simulator, named GEM, is an EOS reservoir simulator for compositional, chemical and unconventional reservoir modelling. GEM was build for extensive oil and gas recovery simulations, but due to its robust thermal module combined with its geomechanic functionalities it is suitable for CCUS applications. It is a fully implicit simulator with adaptive implicit option, which can be useful for converging problems. It uses PR- or Soave- Redlich-Kwong EOS, which can also be replaced by EOS data prepared in CMG's WINPROP. The geomechanic module can progress elastic and plastic deformation during production or injection, and facture initiation. Table 4.1 describes the physical properties GEM is able to simulate, and which are used in this research. These properties allows to focus on the impact of stress changes due to temperature and pressure changes, fracture initiation and propagation and the fracture's effect on the simulation and thus on reservoir behavior. Other physical processes are turned off because they significantly increase the computational power required to calculate the simulation and thus increase model instability. Water vaporization is turned off because the vaporization adds a minor cooling effect on top of the other thermal effects, but the inclusion of H_2O in the EOS reduces model stability. Salt precipitation would decrease the well's injectivity, which would add multiple components to the system while contributing

only slightly to the effect of thermal fracturing. Lastly, permeability reduction is excluded as permeability reduction of the matrix would have a small effect on the overall outcome with the injection of almost pure CO_2.

Physics	GEM	note
Multi-phase flow	✓	
EOS	✓	Peng-Robinson
Multi-component	✓	CH_4, CO_2, H_2O
Salt precipitation	×	
Water vaporization	×	unstable model
Permeability reduction	×	
Residual trapping	✓	
Relative permeability	✓	tabular
Capillary pressure	✓	tabular
imbibition	×	tabular
Thermal option	✓	
Geomechanics	✓	

Table 4.1: Physical processes included in GEM and which are used in this research. Modified after Creusen [34]

For this research an academic license is used instead of a commercial license. The academic license is not limited on the physical processes, but is limited to single core simulations, with a maximum amount of 100.000 active grid cells. Simulations with elaborate subsurface models are therefore not possible, as well as simulations with extremely fine grids.

Geomechanic module

The coupling between the geomechanical model and the simulator is fully coupled in a modular and explicit fashion to improve flexibility and decrease computational cost [38]. Figure 4.9 shows the roadmap for sequential coupling of the geomechanic calculations. The geomechanic calculations are similar to what is described in chapter 2, but also takes in to account the effect of porosity changes due to stress changes, that cause displacement and thus a change in strain. The stress is calculated using the force equilibrium equation;

$$\sigma = f(\epsilon) \tag{4.50}$$

where σ is the effective stress tensor, f the body force tensor and ϵ the strain tensor. This means that the effective stress is calculated based on strain, which is on its turn based on the strain-displacement relation;

$$\epsilon = \frac{1}{2}(\nabla u + (\nabla u)^T) \tag{4.51}$$

The displacement u and u^T are respectively the displacement caused by the change in pressure and the change in temperature. The total displacement is calculated based of the thermoporoelasticity, in the form of

$$\nabla[C : \frac{1}{2}(\nabla u + (\nabla u)^T)] = -\nabla[(\alpha p + \eta \Delta T)]I \tag{4.52}$$

where C is the tangential stiffness tensor (equivalent of the Young's modulus in 1D), I the identity operator, η the thermal elasticity constant which is a parameter for the change of displacement caused per degree of temperature change. According to Figure 4.9, this is used to redefine the porosity and thus the compressibility and permeability of the system, as porosity is a function of pressure, temperature and total mean stress [38].

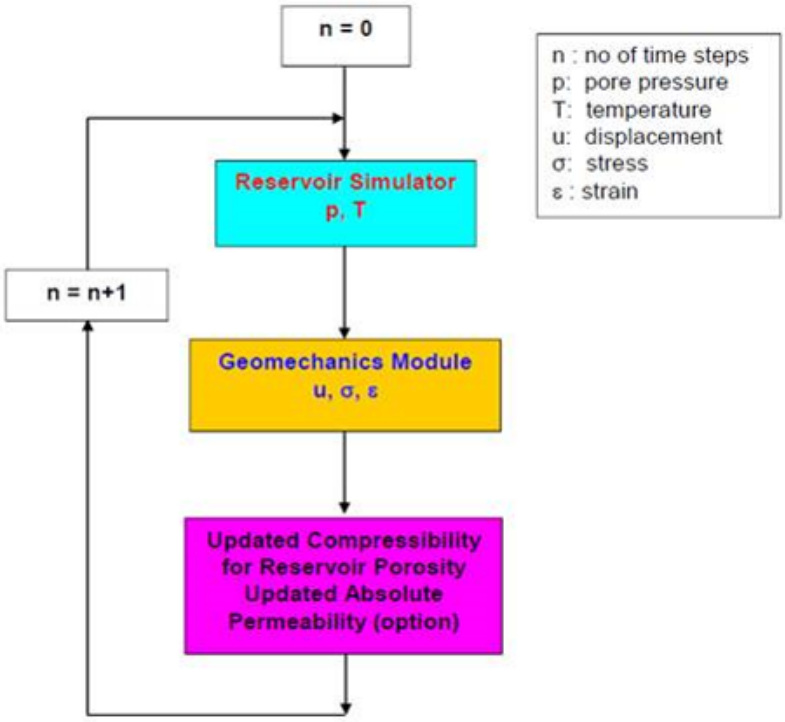

Figure 4.9: Roadmap for the geomechanic calculations in GEM [38]

4.5.2. Dual Medium simulation

A dual medium model is a modelling technique where two media can be assigned to one reservoir model [51]. This is done by specifying two separate grid systems within a model, as can be seen in Figure 4.10 [52]. In case of fracture simulation, the media are specified to be a matrix and a fracture medium. The main difference between these two media is their permeability and porosity values, as fractures usually have low volumes but high flow potential. One porosity and permeability then represents the rock matrix and the other represents the fracture network.

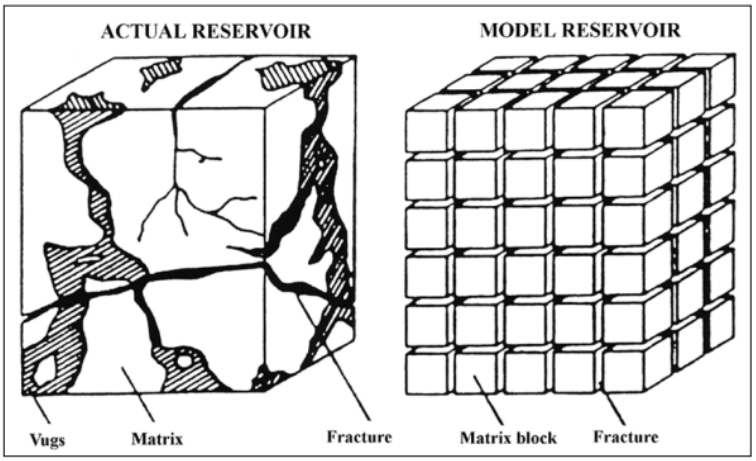

Figure 4.10: Transformation of a natural fractured reservoir to a dual medium model [52]

In single medium models, a simulation cell is assigned only one permeability value. This means that, to simulate natural fractures, blocks need to be assigned different permeability values with very fine grid blocks to correctly simulate the influence of a fracture on the system. This would include computational demanding grids with high heterogeneity, whereas it is deemed to have the same effect as

dual medium modelling [51]. This is because the interaction between grid blocks of the two grids is calculated simultaneously according to subsection 4.3.5.

In Figure 4.11 this is called a Dual-porosity Dual Permeability (DPDP) model [53]. This figure represents fracture modelling options. Single-Porosity Single-Permeability (SPSP) models are used for fractured models when there is natural fractures with a very tight matrix, where the pore volume in the matrix is very limited and the flow is solely defined by the fractures. Dual-Porosity Single-Permeability (DPSP) is used when the matrix does not enhance flow but is significantly larger in terms of pore volume and therefore can be considered as an influential asset to the reservoir's flow [53]. This could be the case for very tight shales. When fractures are induced, a reservoir has matrix flow, so it is important to model all interactions. This is the case for Dual-Porosity Dual-Permeability (DPDP) modelling.

As explained in section 4.4, the fractures are usually propagating orthogonal on the direction on the minimum stress, following the principal of mode I fractures. For this reason, the DPDP model is limited to only propagate in one direction. This also means that it is not necessary to model other grid cells that are not located orthogonal to the minimum stress. Therefore it is decided to not include these cells, and reduce the number of grid blocks to have a width of one cell, as the fracture would not propagate in another direction anyway. The width of this cell should be minimized, as fracture aperture is only a few millimeters and the fracture cell should not contain a high pore volume to incorrectly model a fracture's impact on fluid flow. However, as matrix volumes are usually significantly larger than fracture volumes due to their difference in porosity, the impact on the fluid flow with larger fracture cells is small.

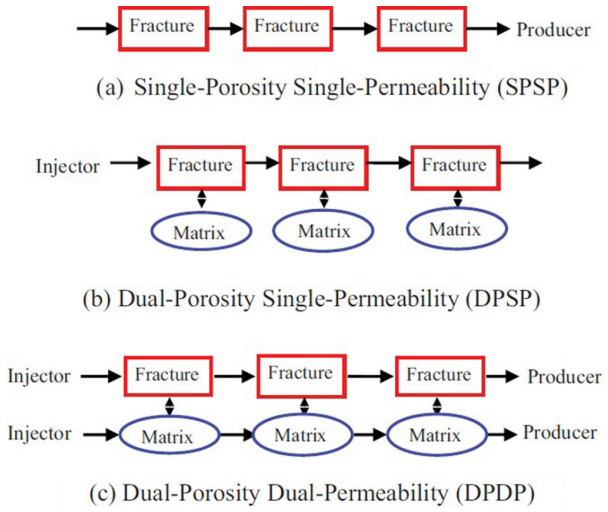

Figure 4.11: Representation of the dual porosity interaction between grid blocks, works similarly for dual permeability [53]

Barton Bandis model

The Barton-Bandis (BB) fracture model is an application to the dual medium grid to replicate the effects of fracturing in the reservoir. By using the geomechanic module of the GEM software, the stress field can be implicitly simulated in the matrix grid. When certain threshold values are reached, better known as the fracture stress, the secondary grid, the fracture grid is explicitly assigned a permeability value, representing the fracturing effect. This is an effective way of modelling as it leaves out the complicated geometries of a fracture, while simulating its effect on the reservoir's flow behavior and CO_2 plume propagation. Figure 4.12 shows the path a fracture grid cell undergoes during simulation with changing stress conditions. The relevant parameters that are involved are:

- e_0; Initial fracture aperture $[m]$
- k_{ni}; Initial normal fracture stiffness $[kPa/m]$
- frs; Fracture opening stress $[kPa]$
- k_{hf}; Hydraulic fracture permeability $[mD]$

- k_{ccf}; Fracture closure permeability $[mD]$
- k_{rc}; Residual value of fracture closure permeability $[mD]$

A fracture is assigned a permeability value that is at least several magnitudes larger than the matrix permeability, as the fractured cells basically act as voids. After fracturing, the stress can increase because of increasing temperature or decreasing pressures, due to lower rates or after injection stopped. This would increase the effective stress. Once σ_n increases above 0, the grid cell is no longer in the tensional regime, meaning that compressive forces close the fracture. When the grid cell becomes compressive again, it gets assigned k_{ccf} in the fracture grid, meaning that fracture closure is initialized. With increasing σ_n the fracture permeability keeps decreasing until k_{rc} is reached. k_{rc} is the fracture's remaining permeability after closure. As there is no form of proppant in the fracture, the k_{rc} can become as low as its original permeability. Figure 4.12 divides these processes in different paths, which can be explained for CO_2 injection by:

- AB: the initial σ_n of the reservoir, which decreases due to CO_2 injection until frs is reached.
- BC: fracturing is initialized, assigning k_{hf} to the fracture grid cell.
- CD: If σ_n continues to drop, the fracture remains open and maintains k_{hf}
- DE: k_{hf} is maintained until the compressional regime is reached (when $\sigma_n > 0$).
- EF: Once σ_n becomes positive, the fracture closes. Once the compression starts, k_{ccf} is assigned to the grid cell.
- FG: with increasing σ_n the permeability gets an exponential behavior with the k_{rc} being the asymptotic value on the x-axis

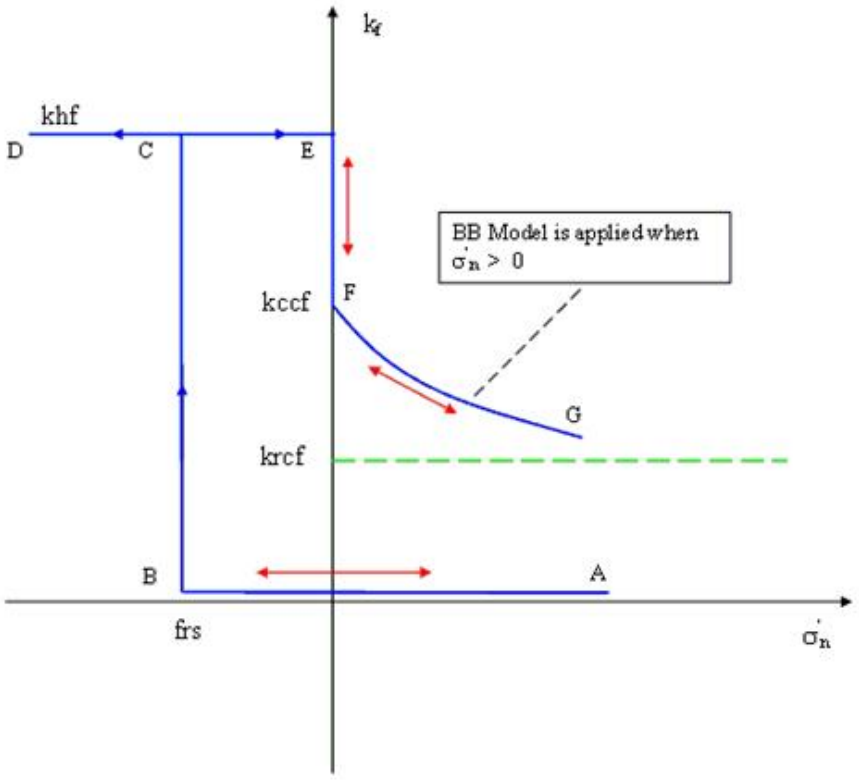

Figure 4.12: Barton Bandis fracture permeability diagram [38]

5
Model set up

To be able to effectively perform an investigation on the Dutch North Sea's fracturing behavior in depleted gasfields due to CO_2 injection, a wide range of parameters can be defined. These can be subdivided in reservoir, rock and operational parameters.The parameters are defined based on databases, lab tests from previous research and standardized industry values.

5.1. Defining a depleted gas reservoir

A basecase scenario for depleted gasfields in the North Sea is defined in Table 5.1. The basecase is defined by the second parameter, the mid parameter. The low and high case are the range in which the parameter can occur in gasfields in the North Sea.

Basecase				
	low	mid	high	[unit]
Rock properties				
Poisson's ratio	0.15	0.20	0.25	$[-]$
Young's modulus	20	25	30	$[GPa]$
Biot's coefficient	0.8	0.9	1	$[-]$
Thermal expansion factor	6e^{-6}	9e^{-6}	12e^{-6}	$[1/°C]$
Reservoir properties				
Permeability	2	15	60	$[mD]$
Reservoir thickness	20	50	80	$[m]$
Depleted reservoir pressure	20	30	40	$[bar]$
Volume	1	2	4	$[bcm]$
Thermal gradient	-10%	-	+10%	$[°C/100m]$
Operating conditions				
Injection temperature	5	20	35	$[°C]$
Injection rate	10	20	30	$[kg/s]$
Stress conditions				
Effective minimum stress	16560	21560	26560	$[kPa]$
Fracture pressure	-1000	-2000	-3000	$[kPa]$

Table 5.1: low, mid and high case for each parameter.

5.1.1. Rock properties

The rock properties include the parameters that define the geomechanic reaction of the rock under stress. The main parameters that influence the state of stress are the Biot's coefficient, Young's modulus, Poisson ratio and the thermal expansion coefficient. Defining the rock properties can be done statically and dynamically. Static properties are defined in the lab, based on physical core plug samples, with idealized experiments. For example, the Poisson ratio is found by measuring the horizontal and the vertical elongation after pressurizing a rock sample. In Figure 5.1 an overview is added of the results of static experiments on sandstones, limestones and shales with different porosity. The porosity

in the North Sea reservoirs are typically between 0.10 and 0.20, so therefore the Young's Modulus is in the range from 20 to 30 GPa and the poisson ratio between 0.15 to 0.25.

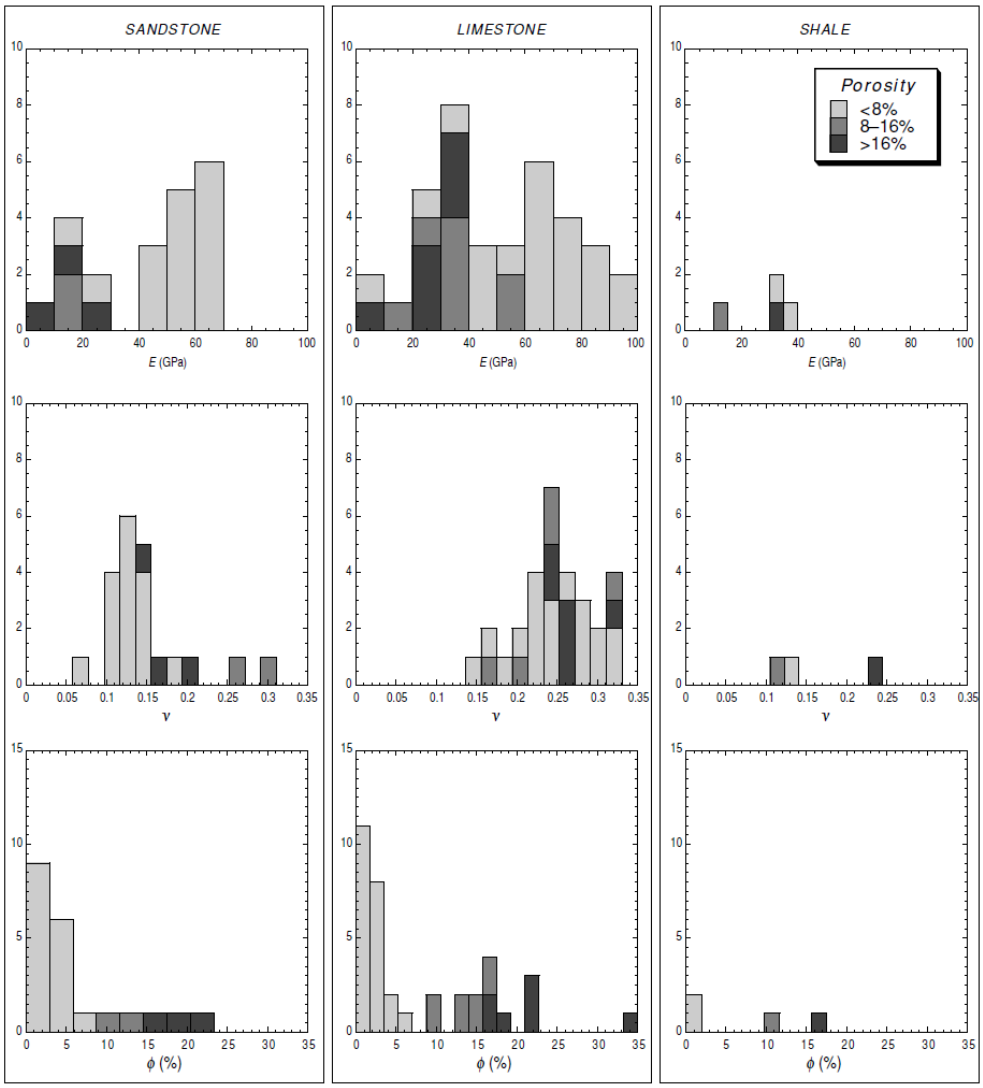

Figure 5.1: Rock parameters based on static lab experiments [28]

The thermal expansion coefficient is a relation between the quartz content of a sandstone and its expansion due to temperature changes [28]. An increased α_T results from higher quartz content in the rock. Figure 5.2 show the experimental results, concluding that a typical sandstone has a thermal expansion coefficient ranging from $6 * 10^{-6}$ and $12 * 10^{-6}$ 1/°C.

The fracture pressure of the rock defines under what tensile conditions a fracture initiates. Expert opinion is that the tensile rock strength is close to zero, compared to the initial minimum horizontal stress, ranging from -1 to -3 MPa.

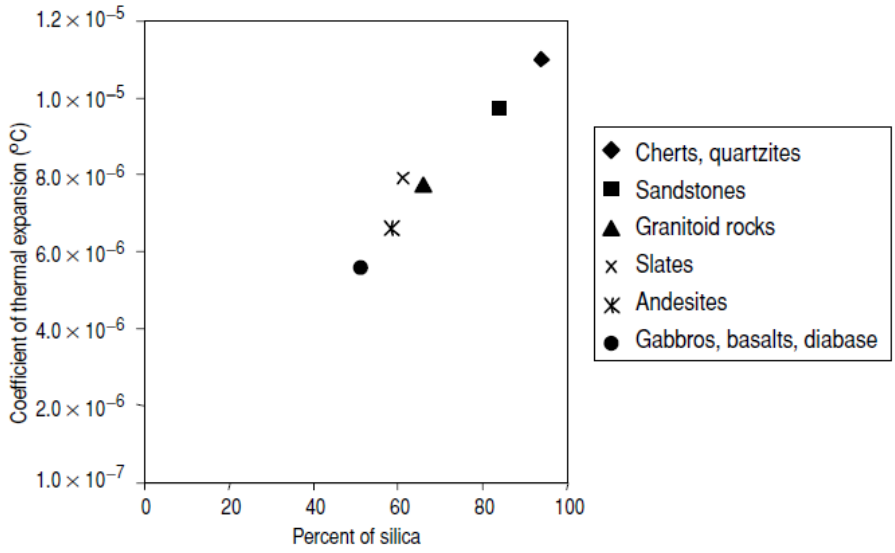

Figure 5.2: Thermal expansion coefficient based on the silica content in a rock. A typical sandstone has a thermal expansion coefficient of $10e-6\ 1/C$ [28]

5.1.2. Reservoir parameters

The reservoir parameters describe under what conditions the rocks are situated. This includes the size of the reservoir, the depth on which the reservoir lies, its thickness, its permeability, reservoir pressure, the stress conditions of the reservoir and the thermal gradient in the subsurface, which determines the reservoir's temperature.

Permeability and thickness

In reservoir engineering, the flow potential through the reservoir is usually defined as kh, which is known as the effective permeability, in mDm. This is the thickness of the reservoir multiplied by the average permeability over this interval, giving a better indication on how much CO_2 can be injected over a well interval. The kh used in this research is based on expert's experience, based on the average values found in the Rotliegendes and the Buntsandstein formation in the North Sea reservoirs (Table 5.2). Additionally, a homogeneous reservoir with a horizontal-vertical permeability ratio (kV/kH) of 0.1 is assumed.

Case	kh	thickness	permeability
Basecase	750 mDm	50 m	15 mD
Permeability (HC)	3000 mDm	50 m	60 mD
Permeability (LC)	750 mDm	50 m	2 mD
Thickness (HC)	1200 mDm	80 m	15 mD
Thickness (LC)	300 mDm	20 m	15 mD

Table 5.2: effective permeability for the low (LC) and high (HC) cases for the permeability and thickness parameter.

Stress conditions, thermal gradient and depleted reservoir pressure

The state of stress for a depleted gasfield can be formulated from the rock properties, together with the equation from section 4.4. However, both the horizontal and vertical stress can be locally very different due to the overburden composition, state of depletion and also due to unknown reasons. Another way of deciding the minimal horizontal stress is by using leak off test (LOT) data.

A LOT, also known as a minifrac test is a test where the pressure in a well is increased on a constant rate to initiate a hydraulic fracture [54]. Figure 5.3 illustrates that the point of fracturing can be recognized as the point where the pressure build up is not linear anymore. This is the so called leak of point (LOP). As discussed before, fracture initiation by pressurization is caused by mode I fractures. Thus, this test allows you to identify the direction of the minimum horizontal stress and its magnitude, which would be

equal to the LOP. However, it should be mentioned that this is not a perfect method to determine the minimum principal stress of a field, as wells are 1D data points and the hoop stress, the stress around the borehole, can influence the outcome of the LOT [28].

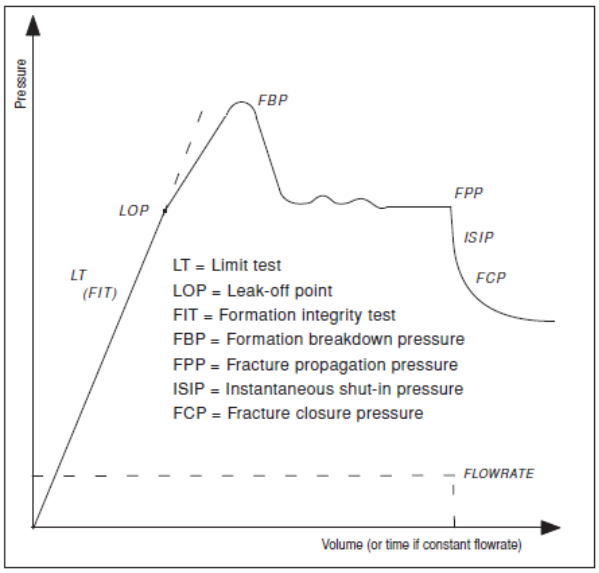

Figure 5.3: Schematic representation of the determination of the minimum principal stress in a borehole [28]

Finding the maximum horizontal stress, however, is more challenging [54]. Expert advice is that if there is no (major) active tectonic regime present, and without extensive logging data available, the S_h^{max} can be estimated to be 10% higher than the S_h^{min}.

The leak off test data of the North Sea is available in the SNS database in Appendix A. This database, created by EBN B.V. in collaboration with TNO, consists of LOT's and temperatures of 1143 wells . Using the SNS database, the minimum horizontal stress at 3000 m deep is 45 to 55 MPa, resulting in an average minimum horizontal stress gradient of 16.7 kPa/m. The effective minimum horizontal stress can then be calculated to be 26330 kPa. The vertical and effective vertical stress is calculated to be respectively 33000 and 65700 kPa based on the hydrostatic gradient. For this research, however, to closely research the effect of thermal fractures and the effect of the main parameters on thermal fractures, a lower minimum horizontal stress gradient is assumed. This gradient is 15 kPa/m, resulting in an effective minimum stress of 21560 kPa. The constraint on the maximum reservoir pressure due to re-injection is set in between the LOT and the vertical stress conditions before depletion, at 40000 kPa.

The temperatures of the wells in the SNS database is used to define an average thermal gradient for the North Sea area;

$$T = \frac{D + 77.67}{30.7} \tag{5.1}$$

where T is the temperature at depth D. The depleted reservoir pressure is dependent on the state of depletion of the reservoir, but can go as low as 20 bar for reservoirs with favorable production conditions. The range is therefore set from 20 to 40 bar.

5.1.3. Operational parameters

For CCS projects, two parameters can be controlled during injection, the injection temperature and the injection rate. However, these parameters are influenced by the state of the reservoir and the preferred reservoir conditions. A lower rate means that the reservoir will be filled slower, the reservoir pressure will increase slower and the CO_2 plume will propagate slower. The latter is also defines the thermal front propagation and the reservoir temperature, which drops due the cold CO_2 that is injected. The

rates and injection temperature used in the screening are based on industry standards to ensure the preferred operation conditions. These ranges are 10 to 30 kg/s and 5 to 35 $°C$ respectively.

5.2. Analytical sensitivity study

Based on the thermoporoelasticity equations in section 4.4 a preliminary sensitivity study can be done. By calculating the change in stress for each high and low case, the pressure at fracture initiation can be calculated. The increase in injectivity and fracture propagation and halflength cannot be calculated in this manner, but it does give an insight on how the parameters affect the stress conditions and can be used to validate the system by comparing the pressure and temperature conditions in the model at the moment of fracture initiation with the expected fracture initiation based on the thermoporoelastic response. However, the thermoporoelastic equations do not include the flow equations, meaning that only the rock parameters, depleted reservoir pressure and stress are considered in the comparison. This way, the effect of the compressibility, displacement and strain caused by the injected CO_2 is not included in the change of the stress conditions. To correctly validate the model, the adjustment factor has to be found according to subsection 4.4.2 to compare the analytical solutions with the solutions of the numerical model.

5.3. Numerical model

A depleted gas reservoir model is simulated by creating a Cartesian dual permeability box model. Figure 5.4 includes the box model. The remainder of this section explains how the model attributes are defined to make it both realistic and applicable to the research aim.

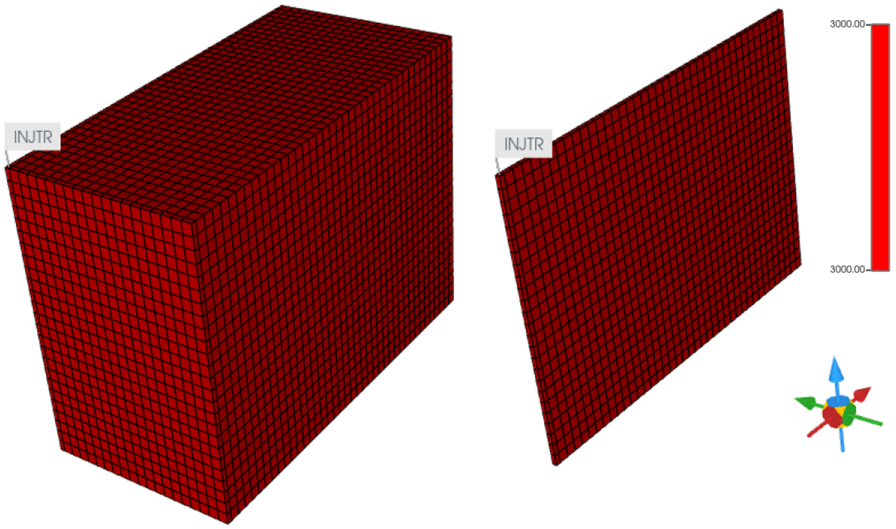

Figure 5.4: Box model of the basecase, with on the left the matrix grid and right the fracture grid, both in depleted state (initial conditions).

5.3.1. Matrix and fracture grid definition

At depleted reservoir conditions, the matrix and fracture grid share the same properties throughout the model except for the porosity. The porosity for the fracture grid is set to be 0.001 as this significantly reduces the pore volume inside the fracture. In reality, a fracture is an opening with very small aperture, of only a few millimeters. As the dimensions of the fracture grid are the same as the matrix grid, the pore volume of this fracture is sized down to represent the small volume that a fracture could have. Secondly, the fracture grid is set to be inactive for all layers except the horizontal interval that is inline with the location of the well (Figure 5.4). This is because, as chapter 2 describes, fracture propagation is only expected to take place orthogonal to the direction of the minimal stress and thus extra fracture grid cells would only cause computationally more costly simulations, as their pore volumes are considered small enough to not have a major influence on the propagation of the CO_2 plume before fracture initiation. So it is important to emphasize that the fracture geometry is not accurately modelled with an aperture, but

solely on how the flow in the model would be influenced by an increase in permeability after fracturing in a very low pore volume fracture grid block that communicates with the surrounding matrix and fracture cells.

5.3.2. Model dimensions

The model is designed to correctly translate the physics in the system during injection. To research the effect of the fractures, the model must be large enough to incorporate the full fracture length, while preventing enhanced pressure build-up around the well due to limited pressure dissipation, which can happen if the model is too small. Therefore, the model is 800 by 800 m in i and j directions, with a k direction that is constant through the reservoir and is defined by the thickness of the reservoir.

Model optimization

To minimize the computational cost of the simulation, the amount of grid cells can be reduced. In this process, it is important to make sure the outcome of the simulation does not change. As fracture propagation is only in one direction, in the j direction, there is no reason to simulate all cells in the i direction. Therefore, half of the gridcells in the i direction are removed. This would, however, reduce the total pore volume to 50%, and thus the pressure build-up in the system would increase with a similar factor. Therefore a volume multiplier is necessary to account for this effect.

Volume correction

The storage potential of the reservoir is based off the recovered gas volume from the reservoir during production. This is expressed in volume of gas at surface conditions, in bcm. To reach this volume at reservoir conditions, which is dependent on its volumetric expansion factor and the available pore space, the gas volume at reservoir conditions can be calculated using Equation 5.2 [55]

$$B_g = \frac{V}{V_{sc}} = \frac{pTz}{p_{sc}T_{sc}z_{sc}} \tag{5.2}$$

To find the exact volumetric factor for the reservoir conditions in this model, the B_g has been extracted from GEM by simulating gas production from virgin reservoir condition (before depletion). With B_g known, the required pore volume can be calculated that matches the preferred storage volume. By adding a pore volume multiplier to the outer cells of the reservoir, the right reservoir size can be created, while not disturbing the NWB effects of CO_2 injection. The volume factor of the outer cells is set while considering a total surface volume of 2 bcm for the full grid (for the basecase), with a volumetric expansion factor of gas being $B_G = 3.76e^{-3}$.

Quarter grid

A second option for simulation optimization is by modelling only a quarter of the grid. As the model is perfectly symmetric in all four directions, it is possible to only model 25% of the model. However, a few modifications have to be made in the well model, according to the Peacemen equation (Equation 4.27). The w_{frac} is the radial fraction of the well, which is set from 1 to 0.25 for a quarter grid. The geometric factor (CC) is a correction for the location of the well inside the grid block. For a full model, the well perforates in the middle of the grid block, while for a quarter grid, this perforation is located in the corner of the cell. The CC for a center grid cell injection is 0.56 and for a corner grid cell injection is 0.36 [38]. Lastly, as the total pore volume is 0.25 of the original, the rate is also set to 0.25 of the original rate to ensure the same pressure build up in the system. The well diameter remains the same. This also means that the grid blocks of the vertical interval of the well is 0.25 of its original size, as the boundary cells of the quarter grid got split in half. Figure 5.5 depicts all the volume and grid modifications done for the depleted gas field model.

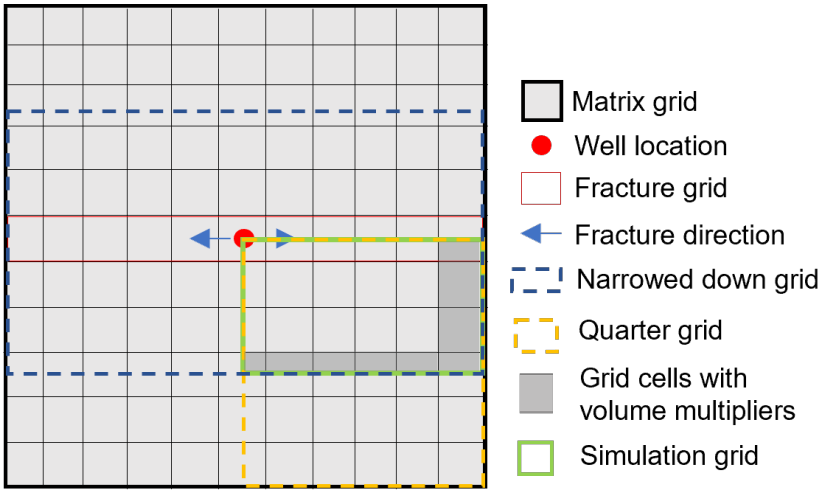

Figure 5.5: Top view of a schematic reservoir model that shows the reduction of gridcells to optimize simulation time. The simulation grid (green) shows the part of the model that is simulated.

5.3.3. Well model and injection fluid

The well diameter is 0.08 m, which is the default value for the GEM simulator SOURCE. Industry standard is to perforate the whole reservoir interval, thus the perforation interval is equal to the thickness of the reservoir. The injection fluid is close to pure CO_2, comprised of 96% CO_2 and 4% CH_4. As CO_2 and CH_4 are miscible, the viscosity and density are almost identical to pure CO_2. However, for simulation purposes, the injection fluid is not pure as this allows for a slight change in thermodynamic behavior of the injection fluid. With a mixture, there is a two-phase region as it is a binary system. Without a binary system, the injection fluid is more sensitive to phase changes (section 4.1). When the phase change happens in a reservoir, there is rapid density changes of the CO_2, changing the volume of the injected phase rapidly and thus the pressure in the reservoir. These fast pressure changes in a small time frame cause converging issues in the simulator, thus a less pure CO_2 mixture is preferable for modelling CO_2 injection.

5.4. Model Assumptions

To focus on the effect of thermal fractures in the reservoir, a couple assumptions are made to simplify the model. Therefore, it is assumed that the model has a homogeneous lithology with an anisotropic permeability. This includes homogeneous rock compressibility, rock geomechanics and porosity. Some of the physical assumptions are shown in Table 5.3.

Physical process	
Water vaporization	excluded
Salt precipitation	excluded
Non-isothermal	included
Poroelasticity	included
Thermoelasticity	included
Porosity change	included
Strain hardening	excluded

Table 5.3: Physical processes included in the model

5.5. Boundary conditions

The vertical and horizontal boundaries of the model are no-flow boundaries. The vertical boundaries have heat-loss with the overburden and underburden, which is calculated by the default rock density of 2650 kg/m^3 and a thermal rock conductivity of 2 $J/m \cdot s \cdot K$. The geomechanic boundaries allow for

displacement in all directions except for the bottom of the model, as that is used as reference point. Lastly, the thermal module is not able to simulate below 0.3 $°C$, so injection with extremely cold CO_2 is not possible. The maximum BHP that is allowed in the well is based on the virgin reservoir pressure, as inflation beyond virgin pressure is undesirable due to the unknown seismic risk that it creates. The virgin reservoir pressure can be estimated with the hydrostatic gradient and is set to 40 MPa. The simulation is ran for a maximum of 15 years, which should easily cover the injection time it takes to fill the reservoir and helps to understand the reservoir behavior right after injection ended.

5.6. Defining Barton Bandis model

The Barton Bandis model, as explained in Figure 4.5.2, needs to be defined to formulate when fracture initiation happens and how the fractures close with pressure and temperature dissipation. frs is based on the tensile behavior of sandstones. Expert opinion is that the tensile rock strength is close to zero, compared to the initial minimum horizontal stress, ranging from 0 to -3 MPa. The fracture closure conditions are less important for this research, because during injection the pressure conditions remain high enough to keep the fractures open. Once operation stops the fracture permeability is not so relevant anymore. Therefore, standarized and default values are used for this, including the e_0, k_{ni}, k_{ccf} and k_{rc}.

5.6.1. Fracture permeability and porosity

The impact of the fracture permeability on the pressure development over time, the fracture propagation and the injectivity was investigated for the Barton Bandis fracture modelling approach. In the Barton Bandis model, the fracture permeability is most relevant to run a sensitivity on, as the other fracture parameters are only used to define fracture closure behavior. Figure 5.6 shows that the fracture permeability has barely an influence on the fracture propagation, the fracture halflength. The similarity in fracture propagation are consistent with the BHP development of these cases, which are also very similar (Figure 5.7). Thus, the main consensus is that as long as the fracture permeability is significantly larger than the reservoir permeability (as in Figure 5.6, 15 mD in the reservoir and 0.2, 1, 10 and 100 D as fracture permeability), the impact of fracturing is more or less the same for different fracture permeability.

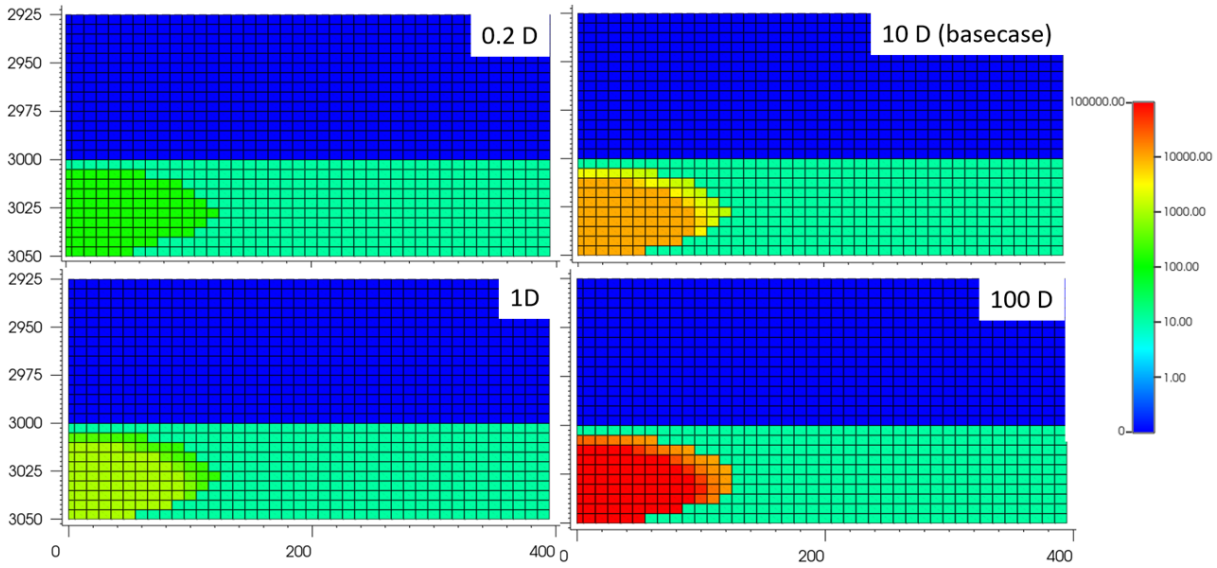

Figure 5.6: Base case after 15 years of simulation. It shows the permeability in the J-direction for each grid block in the fracture grid. A increased permeability (higher than its initiated value of 15 mD) means that the grid block is fractured.

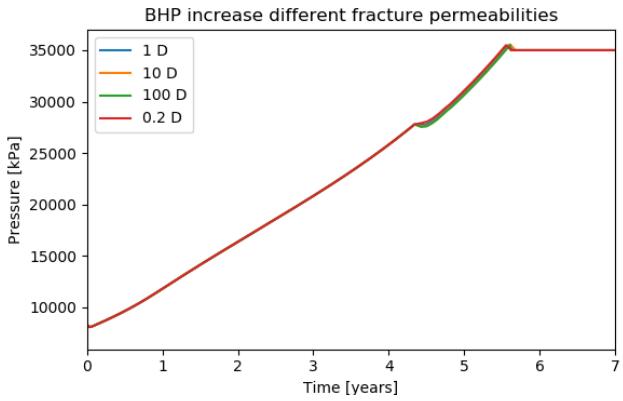

Figure 5.7: Base case after 15 years of simulation for different fracture cell permeability values. The BHP develops in a similar way for the different cases.

The effect of the fracture porosity is similar. As the fracture grid cells are significantly smaller in pore volume, the pressure development is similar with different fracture pore volumes. This pore volume can be seen as the way to define the aperture of the fracture, by multiplying the pore volume by the width of the cell. In case of a fracture porosity of 0.001 and a fracture cell width of 10 m, the aperture can be defined as $0.001 * 10 = 10mm$. This is a fairly large aperture for a fracture (for example, the maximum aperture due to cold CO_2 injection in a Norwegian North Sea reservoir is $0.5mm$ [56]), but the contrast is high enough to not disturb the outcome of the simulation. The main issue with defining the fracture porosity is that it is additional pore volume in the direction of the fracture due to added grid blocks, which can cause an even more elliptic propagation of the thermal front, even without fracturing. However, as the fracture grid is only 1 block wide, this effect is minimal in this research.

5.7. Grid refinement

Another technique to optimize simulation time is by grid refinement. Grid refinement is a process where an optimal grid size is being investigated. In this project it is essential to understand to what level the models can be compared to the reference model, which is the finest solution that comes closest to the actual physics by compartmentalizing the subsurface in very small sections. If it is decided to use a grid size that does represent the truth less detailed but is computationally much more favorable, it is important to understand how it impacts the relevance of the simulation. Figure 5.8 shows the BHP's of simulations with different grid cell sizes but equal pore volumes, together with a simulation of a full grid instead of a quarter grid. The simulations are equal to that of the basecase, but with an injection temperature of 40 degrees (to simplify the simulation) and with an initial minimum stress of 15560 kPa (to ensure fracture initiation with high injection temperatures). It shows that the finest grid (5 m) fractures earliest, with the largest grid size (20 m) fracturing last.

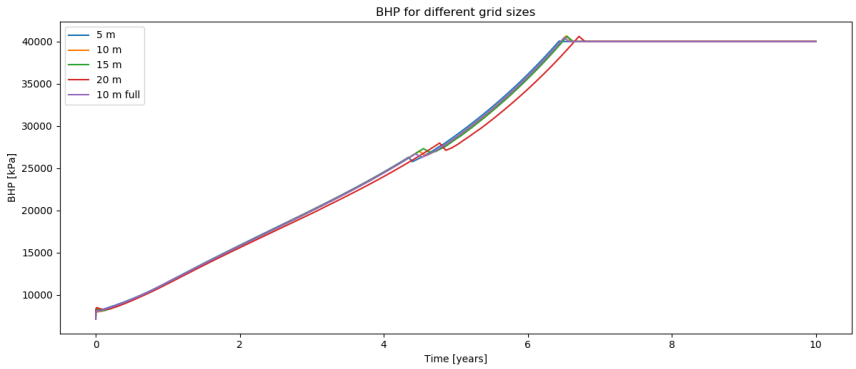

Figure 5.8: BHP development of different grid sizes with the same pore volume. Notice that finer grids initiate a fracture sooner. The full grid has very similar results to the quarter grid variant.

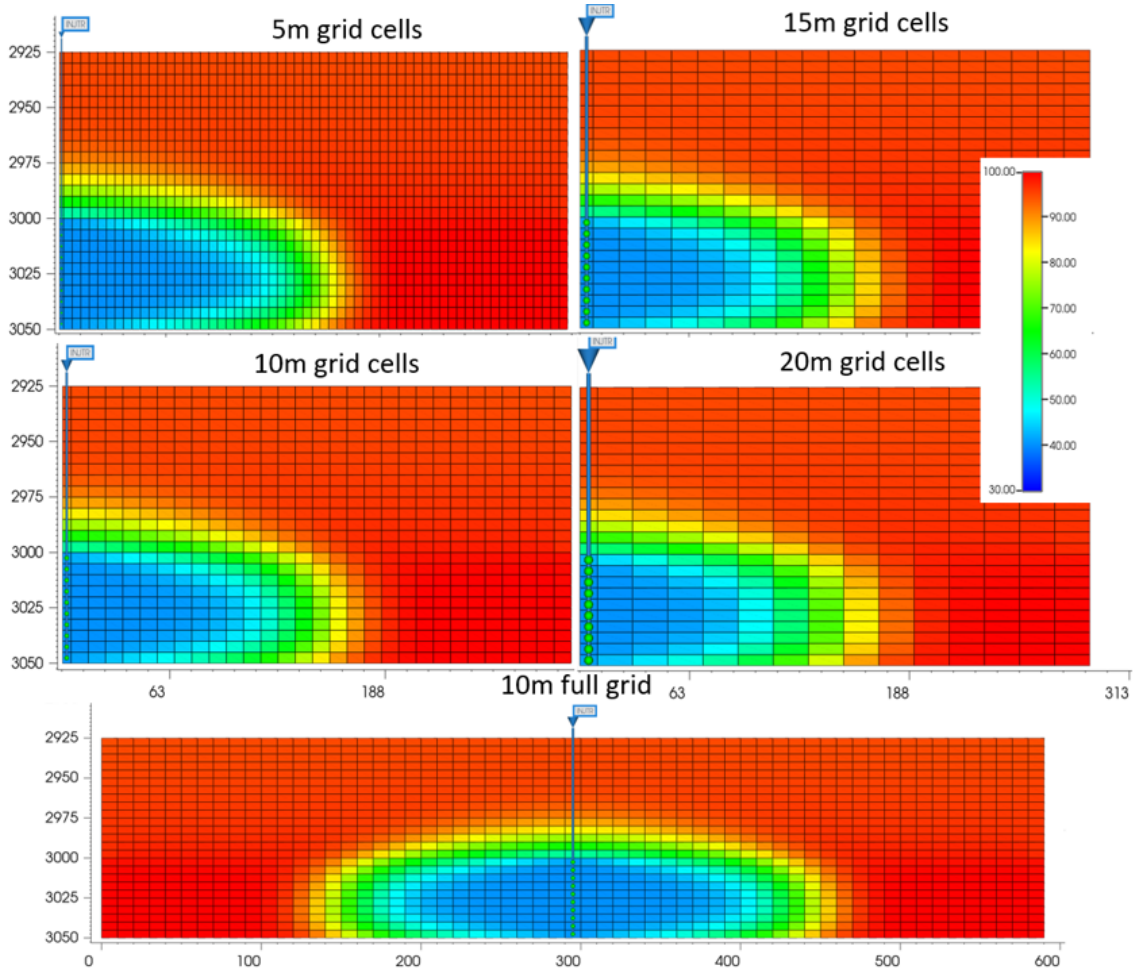

Figure 5.9: j-k cross-section of the thermal front for different grid sizes after 15 year of simulation. The thermal front reaches more or less the same distance, while the cooling in the perforation interval is more intense for finer grids. The bottom simulation contains a full grid simulation with the well located in the centre of the model.

This can be explained by Figure 5.9. The cooling is more excessive in a shorter time with finer grids causing faster fracture initiation. Cells closer to the well will undergo faster cooling and faster pressure build up once they are reduced in size. However, the temperature front propagation is similar as well as the drop in BHP due to fracturing. Table 5.4 shows the computational time of each mesh. It shows that the grid optimization (quarter grid compared to full fraction simulation) decreases simulation time by 82%, while the finest grid cell size of 5 m takes almost 15 times longer than 20 m grid cell sizes. Based on all these results, a grid size of 10 by 10 m is decided on.

simulation fraction	cell size	simulation time
quarter	5x5 m	38:33
quarter	10x10 m	09:47
quarter	15x15 m	04:13
quarter	20x20 m	02:27
full	10x10m	54:01

Table 5.4: Grid simulation times

Additionally, Figure 5.8 and Figure 5.9 include a simulation of a full sized simulation with grid cell size of 10x10 m, instead of a quarter grid simulation. This proves that the quarter grid has the same results as the full grid.

5.8. Caprock

To model the effect of the decreasing temperature and increasing pressure of the reservoir on the overlying rocks, a caprock has been added. The caprock is set to be close to impermeable, with a permeability of 0.00001 mD. The caprock has been both added to the matrix and the fracture grid, to see if there is fracture initiation in the caprock. The caprock is initiated under the same geomechanical conditions as the reservoir, as geomechanical data of the caprock is not available. Different caprock initiation could change the stress path of the caprock but not necessarily the simulation of the reservoir, on which the focus lies in this research. The caprock is simulated for two reasons; i) to understand the effect of cold CO_2 injection on the caprock and ii) to mitigate a simulation issue of the GEM software outside of the reservoir in to the cap rock. The former reason to simulate might be compromised by the latter. The issue originates by GEM's method of calculating the thermoelastic stress. It is suspected that the displacement caused by the thermal response in the reservoir subsequently causes a displacement in the top layers of the grid. It seems that boundary condition issues, meaning that the boundaries are static and do not respond to the displacement of the cooled down region, cause an accumulation of stress in the cap rock, above the cooled down region. When the thermoelastic effect is turned off, this effect is not present anymore. Turning this effect off is not an option however, as this is the driving force behind thermal fracture initiation.

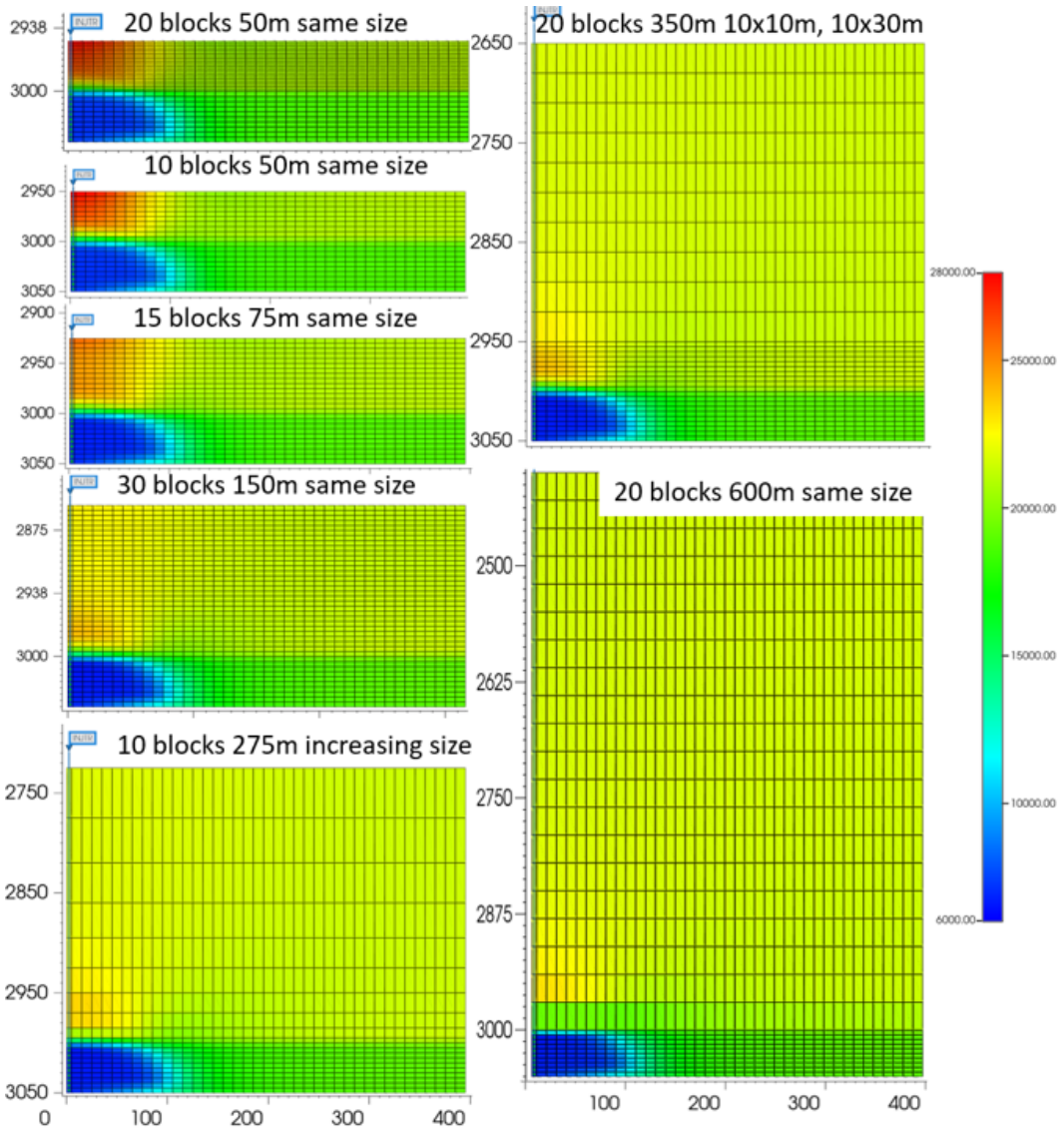

Figure 5.10: $j - k$ cross section of the minimum stress of different caprock sizes, after 15 months of simulation. An increase of minimal stress can be seen right above the reservoir due to the simulation issue.

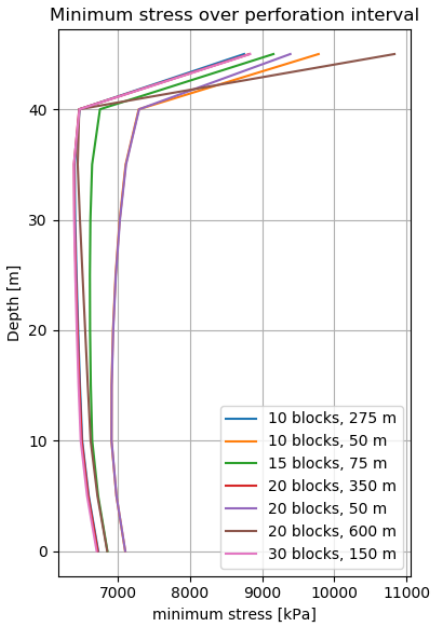

Figure 5.11: Minimum stress variations along the well interval for different cap rock definitions after 15 months of simulation. The top perforation still undergoes the issue. Further it can be seen that a thicker caprock has lower minimum stress values in the remaining perforation cells.

To find a cap rock that is most suitable to model the thermoelastic response in the reservoir as accurately as possible, different cap rocks, cap rock thicknesses and different cap rock grid cell sizes have been investigated. Figure 5.10 show different definitions of the cap rock dimensions and Table 5.5 gives an overview of their effect. It shows that a very thick cap rock does mitigate the problem better compared to thinner cap rock sizes. The increase of minimum stress always occur from the top of the reservoir to around 50 m above it, but with thicker cap rock sizes this effect is reduced to an increase towards 22000 kPa instead of 28130 kPa with a cap rock of 50 m thick.
The issue still slightly effects the simulation of the reservoir in the top perforation (Figure 5.11). This causes a tempered decrease of the effective minimum stress in the top reservoir layer, while the temperature and the pressure in this layer would expect fracture initiation during simulation. Figure 5.11 show the minimum stresses along the well after 15 months of simulation. It can be seen that a thicker cap rock means that the reservoir has lower minimum stress values because there is less displacement due to distant boundary conditions and will thus fracture sooner. Based on these two figures, it is decided to make the cap rock 1.5x the thickness of the reservoir of the basecase (75 m) with the same grid cell thickness as the reservoir, as this mitigates the error sufficiently while keeping a computationally less demanding simulation.

caprock thickness	cells	cell size	maximum σ_{min} [kPa]	minimum σ_{min} [kPa]
50 m	20	2.5 m	28130	6610
50 m	10	5 m	27500	6549
75 m	15	5 m	25150	6300
150 m	30	5 m	24390	6259
275 m	10	increasing	28130	6150
350 m	20	10x5 m, 10x30 m	22130	6100
350 m	20	30 m	22000	6090

Table 5.5: Different caprock thicknesses and grid cells cause different minimum horizontal stress values inside the reservoir. The table includes the minimum and maximum values for the minimum horizontal stress inside the reservoir after 15 months of simulation.

5.9. Determining fracture initiation and propagation

Fracture initiation is determined in the numerical model by finding the grid block that fractures first. Usually, fracture initiation happens in a perforated grid block as the pressure difference and the temperature difference are the most extreme in this vertical interval, while the CO_2 plume propagates away from the well. The plume propagation is expected to have its effect on fracture propagation as well. The relation between the CO_2 plume and the thermal front defines how the fracture propagates. This propagation happens both in the vertical and horizontal direction and is expected to be the furthest for the horizontal interval on the same depth as the fracture initiation due to its kV/kH relation. To find the maximum fracture halflength during operation, the permeability of the fracture grid on the last time-step is compared to its permeability at the first time step. If it increased in value, it means that the BB model was activated and that the fracture has initiated in that grid block. The furthest activated cell is then the length of the fracture.

5.10. Determining injectivity improvement due to fracturing

The injectivity index can be calculated by GEM by using Equation 4.27 which is dependent on the Peacemen equation. However, as Equation 4.28 shows, this equation is dependent on the size of the perforation block. This is a debatable method, as the perforated block is only 1/4 in size due to the quarter grid model and because this would only allow comparison between models with same sized perforation cells. Therefore it is decided to define the injectivity by

$$I = q/(BHP - P^{av}) \tag{5.3}$$

where q is the flow rate, BHP the bottomhole pressure and P^{av} the average pressure in the reservoir model. When the reservoir fractures, there is a sudden pressure 'release' in the reservoir around the well as the permeability increases and thus a drop in BHP. Assuming a constant flow rate, this means that the injectivity increases due to fracturing. To quantify the increase of injectivity, a ratio can be calculated with

$$I_{ratio} = \frac{q_n/(BHP_n - P_n^{av})}{q_{n-1}/(BHP_{n-1} - P_{n-1}^{av})} \tag{5.4}$$

This equation compares the injectivity of the reservoir at timestep n with the injectivity of the reservoir at the previous timestep. However, this does not take in to account the total effect of fracturing, as vertical and horizontal fracture propagation will increase the injectivity on later stages as well. Therefore, the simulation is compared with the a simulation with the same parameters and fracture initiation turned off. This way, for timestep n, the influence of fracturing on the injectivity can be calculated. Equation 5.5 does not include q, as this is constant for both the fracture as the non-fracture case.

$$I_{ratio} = \frac{BHP - P^{av}}{BHP_{nofrac} - P_{nofrac}^{av}} \tag{5.5}$$

5.11. Injection constant

In GEM, there is no option to change the injection coefficient directly, but it can be modified using the equation of γ_h (Equation 4.44). By modifying the Poisson ratio, the equation can be solved to the desired γ_h during injection. Modifying the Poisson ratio has both an effect on the thermoelastic response and the poroelastic response of the reservoir, which is expected when the stress path is changed due to plastic deformation. The γ_h during depletion for the basecase is 0.675. According to P18-4 field research, as part of the ROAD project, a depletion constant of 0.675 would expect an injection coefficient between 0.5 and 0.6. This can be reached by changing the Poisson ratio to 0.307 and 0.35 respectively. In this research, the injection coefficient is added to see its effect on the basecase simulation, but is not involved in the sensitivity analysis as it is not certain what injection coefficient suits the simulation best.

5.12. Numerical sensitivity study

This model now can be used to simulate injection in a depleted gasfield. The matrix grid is 400 by 200 m, with a thickness of 125 m. The thickness consists of 50 m reservoir on the bottom with 75 m caprock

on top of it. The grid cells have a dimension of 10 by 10 by 5 meters. The fracture grid is located at the same i-coordinate as the well, and continues in the j-direction. It is a 40x1x25 grid, which means there is a total of 21000 grid cells to be simulated, with a pore volume of 0.00125 bcm at reservoir conditions. Now that fracture initiation, propagation and the injectivity ratio can be determined, the influence of all parameters can be studied. This is executed by simulating the effect of the high and low case of each parameter, by only changing that parameter per simulation.

6 Results

6.1. Analytical solution of the basecase

The analytical solution of the basecase is shown in Figure 6.1. The left figure depicts the magnitude of change of the poro- and thermoelastic response on the minimum stress. There are some striking notes, namely i) The thermoelastic effect is constant. This is not realistic as the temperature of the reservoir rock will not drop instantly to that of the injection fluid. This approach assumes an instant and constant temperature difference during injection. ii) Without adjustment factor as explained in subsection 4.4.2, the thermoelastic stress cause immediate tensile conditions. The minimum horizontal stress drops instantly from 21560 to -188 kPa. iii) As the thermoelastic effect is constant over increasing pore pressure, the gradient of the minimum horizontal stress is the same as the gradient of the poroelastic response.

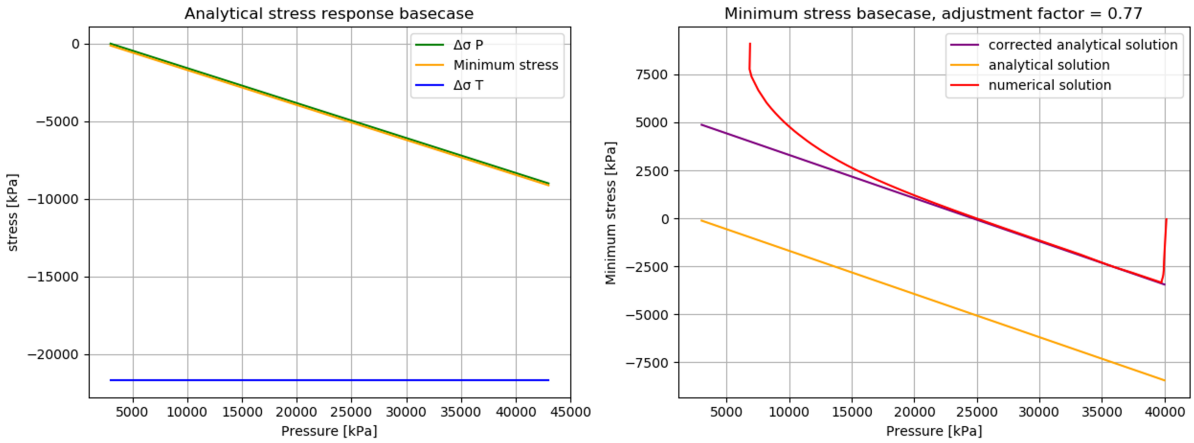

Figure 6.1: Analytical solution of the basecase. Left: solution based solely on thermoporoelastic equations. the thermoelastic stress reduction causes the minimum stress to instantly drop to -188 kPa. The orange line is a result of the thermoporoelastic response (the blue and green line) with 21560 kPa initial stress conditions and an instant ΔT of 80.25 °C. Right: The analytical solution from the left graph (orange) gets an adjustment factor applied to (purple) to match the numerical solution (red).

Figure 6.1b shows a graph containing the same analytical solution as Figure 6.1a, the minimum horizontal stress of the numerical solution and the analytical solution with an adjusted thermoelastic response. The horizontal stress of the numerical solution is taken from the cell of the perforation interval in which fracture conditions are met the soonest, so basically the cell in which the fracture initiation occurs. The graph of the numerical solution starts at a higher pressure due to the injection rate causing an immediate increase in the cell's pressure. The gradient of the numerical solution becomes constant when the cell is cooled to the temperature of the injection fluid. Near 40000 kPa the ΔT increases again as the BHP constraint causes the rate to drop, resulting in less cold CO_2 to be injected, increasing the cell's temperature. When the gradient of both solutions are equal, the difference between minimum stress is adjusted with an adjustment factor to the thermoelastic response of 0.77.

6.2. Numerical solution of the basecase

The numerical simulation using the model as described in chapter 5 gives the results of the basecase as described in Figure 6.2 and Figure 6.3. Figure 6.2 shows the BHP, average reservoir pressure and the rate during the 15 years of simulation. The graph shows that after 7 years the BHP constraint of 40000 kPa is reached, causing the rate to drop. The rate becomes zero once the average reservoir pressure matches the BHP, at which point the injector is no longer present in the model.
The BHP shows a response when the fractures are initiated. After 5.8 years there is a slight drop visible in the BHP, which is due to a pressure drop in the bottom of the well due to increased permeability in the cells near the well. Less pressure is now required to inject at the same rate, causing a drop in BHP. Comparing these results with the 2D cross-sections of Figure 6.3, it can be seen that the figures compliment each other.

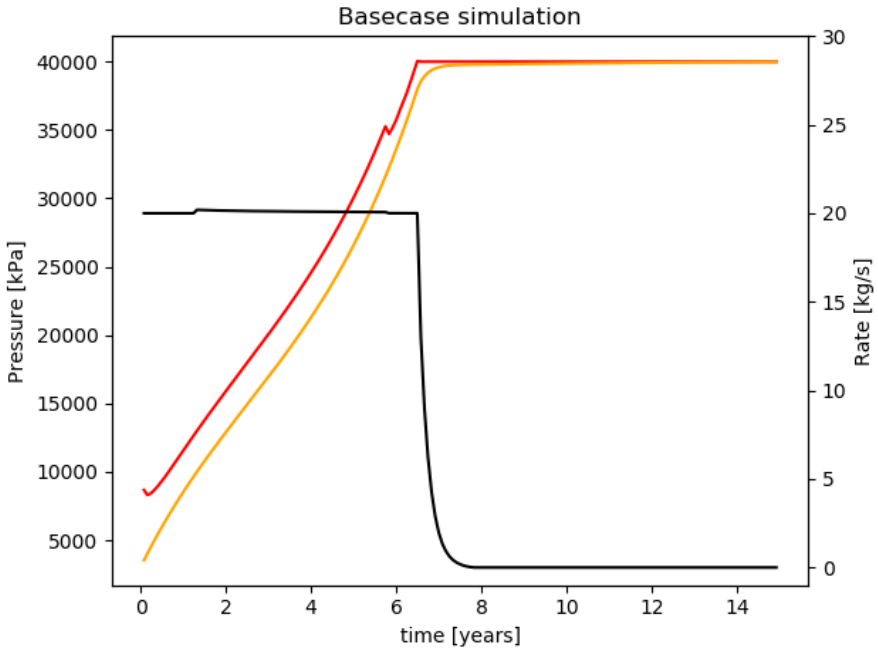

Figure 6.2: Basecase simulation, including the BHP, rate and average reservoir pressure over time.

Figure 6.3 shows the i-k cross-section of the model after 1, 5 and 10 years of simulation on the location of the well. The pressure, temperature, minimum stress and the permeability in the j-direction of the fracture grid is included. The latter gives an indication of the extent of the fracture, as the fracture opens perpendicular on the direction of the minimal stress, the i-direction. The 10 year cross-sections do not have an injector anymore. The pressure shows global increase with the injection of more CO_2, with slightly higher pressure values close to the well. The thermal front propagates and slowly warms up when the injector is removed.
The low effective permeability in depleted reservoirs causes the CO_2 to propagate horizontally as an expanding cylinder, with slightly higher concentration at the bottom of the interval. This is because the CO_2 is colder at the top, making the CO_2 a little more viscous and less easy to propagate through the reservoir. This effect would be much more noticeable with higher effective permeability values, but has almost no effect now.
The thermal front propagates much further in to the reservoir than in the caprock. This is because the reservoir has cooling both through conduction and advection, with a higher horizontal permeability as vertical permeability, whereas the caprock does not. The thermal front moves slower through the reservoir than the CO_2 plume, as the cooling of the rocks is a slower process compared to the propagation of CO_2. After injection stops, the thermal front warms up due to conduction to the caprock, due to the heat-loss to the boundaries of the simulation and due to conduction to the rest of the reservoir.

The decrease in minimum stress covers the same area as the thermal front, following the reaction based on the thermoporoelastic equations. This subsequently leads to a fracture with the same length as the coolest part (below 30 °C) of the thermal front, except for the top layer of the reservoir. The simulation issue in the calculation of the minimum stress causes the top layer of the reservoir to have a significantly lower drop in minimum horizontal stress than expected. This issue also prevents a numerical insight on caprock integrity.

The caprock does not show an increase in pressure, thus gets only cooled via conduction, minimally to 40 °C. Lastly, it is important to realise the reservoir only fractures towards the end of the lifetime of the well, which implies that without the thermoelastic effect the fractures would not initiate hydraulically.

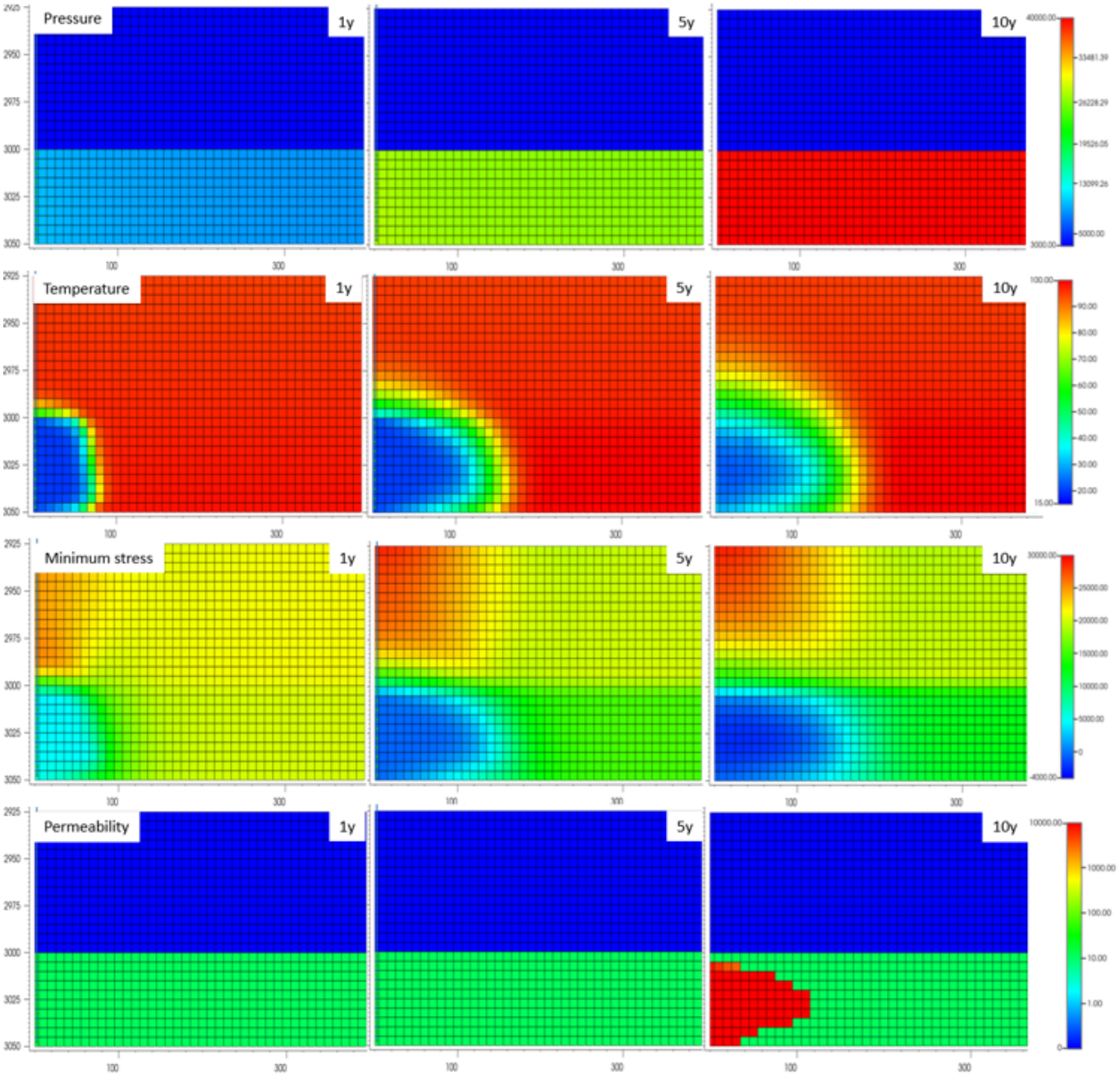

Figure 6.3: i-k cross-section of the simulation of the basecase over a 10 year window. After 10 years injection already stopped, causing the thermal front to warm up again slightly, while the minimum stress still increased as a result of higher pressure conditions.

6.2.1. Injectivity and injectivity ratio

Following Equation 5.4, the injectivity ratio for each timestep can be calculated. Using the average pressure and the BHP of Figure 6.2 and of the same simulation but without fracturing, the ΔP can be plotted as is shown in Figure 6.4a. A drop in ΔP means that there is less of a pressure difference required to inject and thus an increase in injectivity. However, once the BHP constraint is reached, the drop in ΔP means that the rate goes down, meaning that less pressure is needed as less CO_2 is injected. It also shows that without fracturing, the BHP constraint is reached sooner, causing the rate to drop sooner. This means that the average reservoir pressure equals the BHP later (so the reservoir is 'full' later in time), as it did not become easier to inject CO_2 in to the reservoir.
Figure 6.4b then calculates the injectivity ratio between the two cases. Until fracture initiation the ratio remains 1, as the simulations are identical until fracturing. The graph is cut off when the BHP constraint is reached and the rate drops, as this is no longer an increase in ratio due to an increased injectivity. It shows that the maximum injectivity ratio of the basecase simulation is 1.85, which means that the CO_2 becomes 1.85 times easier to inject into the reservoir due to the initiation of the thermal fracture.

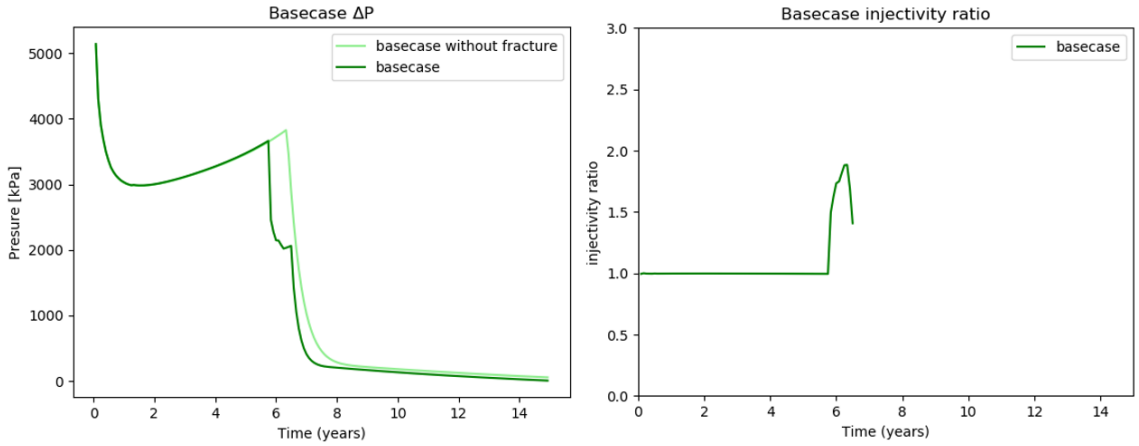

Figure 6.4: Injectivity ratio of the basecase. On the left the difference between BHP and average reservoir pressure (ΔP) is plotted for the basecase with fracturing and with fracturing turned off. Fracture initiation causes a sharp drop. Right: injectivity ratio between the fracture and the non-fracture case. The maximum injectivity ratio due to fracturing is 1.85.

6.3. Sensitivity analysis

This section includes the sensitivities of the analytical and numerical approach based on the high and low cases as defined in Table 5.1.

6.3.1. Analytical sensitivity analysis

Figure 6.5 shows bars plotted for the analytical solution of all the low and high cases. It only includes the parameters that can be adjusted in the thermoporoelastic equations in the form of a tornado plot. Each bar shows the pressure at which the fracture pressure is reached, with a constant ΔT, with the injection temperature at 20 °C and the reservoir temperature based on the thermal gradient as defined in Equation 5.1 (unless the sensitivity on one of these parameters is tested). With a reservoir at a depth of 3000 m, this gives an initial reservoir temperature of 100.25 °C. The minimum stress over pore pressure together with the adjustment factor of each case is added in Appendix B. The bars of the high and the low cases originate from the pressure at which the basecase reaches fracture pressure, at -2000 kPa (except for the sensitivity on fracture pressure). The high and low case of parameters at the top of the graph have the highest impact compared to the basecase. The least influential are at the bottom. If there is no bar showing, this could be because the fracture pressure remains the same or because fractures do not initiate. If there is no fracture initiation, the label of this case is labeled with an asterisk on the right side of the plot. Most bars in Figure 6.5a start at 3000 kPa, which means the thermoelastic effect instantly causes fracture initiation. Figure 6.5b displays the solutions with an adjustment factor of 0.77 applied to it. It shows some changes in the order of the graphs; the poroelastic effect is much higher on higher pressures, resulting in a higher ranking of the Biot's coefficient in the adjusted tornado. The thermal expansion coefficient has the highest impact now, as the negative impacts on the fracture

pressure are not included anymore for most of the cases as fractures do not initiate before the pressure limit is reached in the adjusted cases any longer.

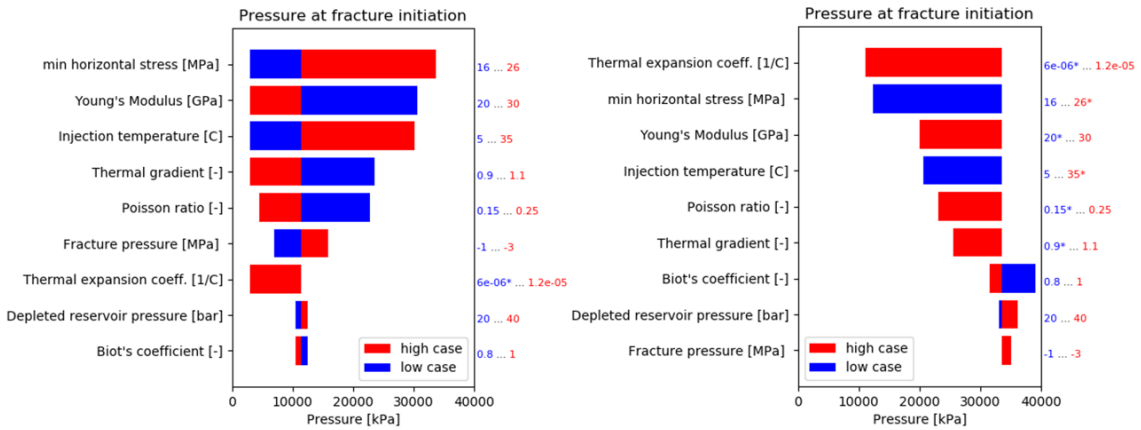

Figure 6.5: Tornado plot of the analytical solution at which pore pressure the fracture initiates. Left: analytical solution without thermal adjustment factor. Right: analytical solution with a thermal adjustment factor of 0.77. The parameters at the top have the most impact. If there is no bar showing, its either because the analytical solution does not reach fracture pressure or because the fracture pressure is reached at the same pressure as the basecase. If the former is true, the label of the case is labeled with an asterisk.

6.3.2. Numerical sensitivity analysis

Figure 6.6 includes all the sensitivities of the time until fracture initiation of the numerical solution. Similar tornado's for the BHP at which the fracture initiates, the halflength of the fracture after 15 years of simulation and for the maximum injectivity increase that happens due to fracturing are presented in Figure 6.7, Figure 6.8 and Figure 6.10.

The time until fracture initiation, or better known as the fracture time, is not present in many cases as fracturing does not happen. This is because the basecase simulation is already fracturing very close to when the BHP constraint is reached, which is the end of the lifetime of the operation. This means that when the sensitivity has a negative effect on the fracture time, fracture initiation does often not happen. This process is dependent on different factors for different sensitivities. For example, for the sensitivities on the rock parameters, the change in the stress path during injection is caused by the different reactions to the same pressure build-up and cooling of the reservoir. Whereas the rate, volume, permeability and thickness have the same stress path based on rock properties, but the change in the way pressure increases causes a stress path on a lower gradient when the fracture time is delayed. The lowest impacts are caused by the depleted reservoir pressure, fracture pressure and the Biot's coefficient. These three parameters do not necessarily change the simulation much, but just delay or accelerate pressure build up slightly due to their small range between the high- and lowcase.

The depleted reservoir pressure, however, is remarkable as both the high and low cases have a negative impact on the fracture time. Normally it is expected that, with a constant rate, following the porothermoelastic equations, lower depleted reservoir pressure would cause later fracture initiation whereas higher depleted reservoir pressure would fracture sooner, as can be seen in the analytical solution. The result in this tornado can be explained by a trade-off effect, where a lower depleted reservoir pressure causes lower BHP values as less pressure is needed to inject at the same rate. The average reservoir pressure is also lower. This causes a lower pressure build-up in the cells around the well, resulting in a later fracture time. The higher depleted reservoir pressure causes a faster BHP increase, as more pressure is needed to inject. However, as the average pressure is higher, the contrast between average pressure and BHP is lower, causing in this case slower pressure build-up around the well with constant rate. Another reason could be that the CO_2 has a different propagation through the reservoir as the CO_2 reaches two-phase criterion on different timesteps, causing density and viscosity changes to be slightly different over the course of the operation, can cause an effect for both cases to be negatively on the fracture time. However, this is only a minor effect.

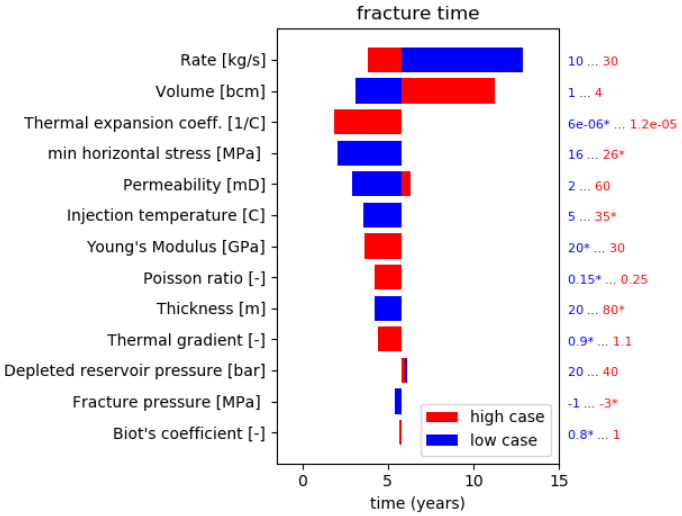

Figure 6.6: Time of fracture initiation of all the high and lowcases of each parameter. If there is no bar and an asterisk next to the label, it means there was no fracturing. If there is no bar and no asterisk next to the label, it means that the time of fracture initiation is the same as the basecase. The depleted reservoir pressure sensitivity both have a negative effect on the fracture time, which can be explained by the phase behavior of CO_2 and how this impacts the pressure development in the reservoir.

The BHP at the fracture time (Figure 6.7) gives an indication of the pressure at which the fracture initiates in the reservoir. The low and high case of the rate both have a negative effect on the BHP. It should be realised that the pressure in the cells in which the fracture initiate are the same, as the cooling for these cells is both equal to the temperature of the injection fluid, resulting in equal ΔT for both cases. A higher rate causes a bigger contrast between the pressure in the well and the reservoir, causing fracture initiation at higher BHP, with higher pressure build-up around the well. A lower rate, however, has the opposite effect. But because the BHP is lower during the operation, the contrast between reservoir pressure and well pressure is smaller, causing slower pressure build-p around the well, needing higher BHP before the fracture pressure is reached in the cell.

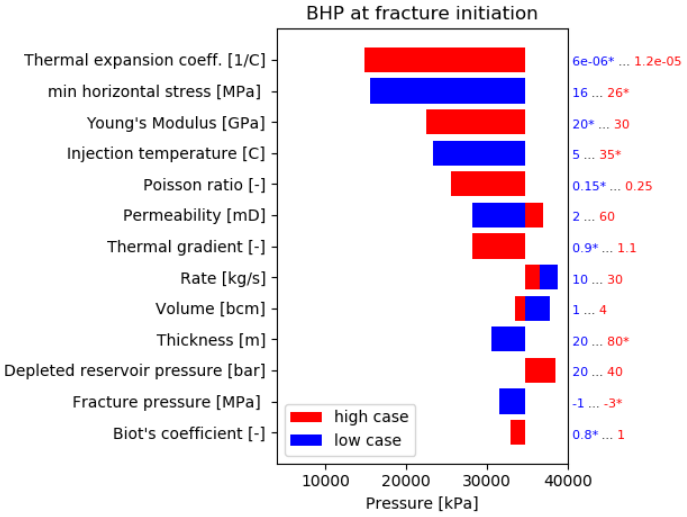

Figure 6.7: BHP at fracture initiation of all the high and lowcases of each parameter. If there is no bar and an asterisk next to the label, it means there was no fracturing. If there is no bar and no asterisk next to the label, it means that the BHP at fracture initiation is the same as the basecase.

The tornado of fracture halflength basically shows the extent of the thermal front when fractures are initiated, except for the sensitivities on temperature (injection temperature and temperature gradient). The thermal front reaches less far once the CO_2 plume propagates faster in to the reservoir. However,

once fracturing happens, the thermal front propagates further in the direction of the fracture due to fluid highways created by the fracture. The high and lowcase of permeability and the lowcase of the thickness have equal fracture halflengths as the basecase.

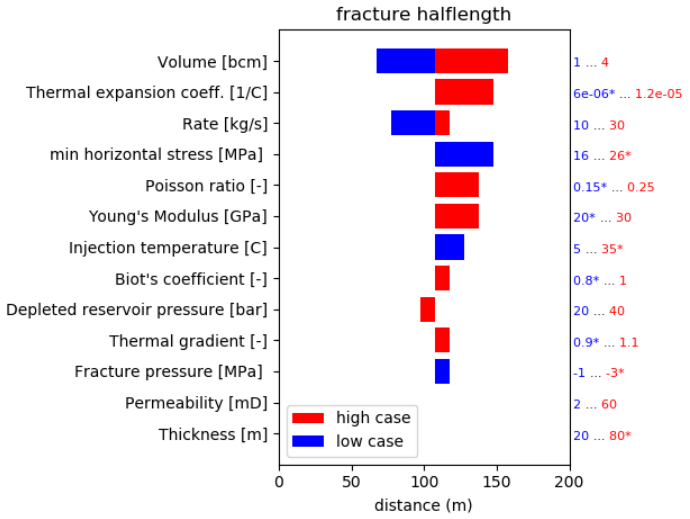

Figure 6.8: Fracture length of all the high and lowcases of each parameter. If there is no bar and an asterisk next to the label, it means there was no fracturing. If there is no bar and no asterisk next to the label, it means that the fracture length is the same as the basecase.

The last tornado gives an insight on the change in injectivity of the reservoir. Figure 6.9 shows what effect fracturing has on the pressure difference. The figure includes the high and low case for volume and how they compare to the basecase. The right side of the figure shows their injectivity ratio. Even though the pressure over time is significantly different, the three cases fracture on the same pressure difference and result in similar injectivity increases due to fracturing, with a maximum injectivity ratio of 1.95. This can be explained by the constant effective permeability before and after fracturing of all the sensitivities (except for the sensitivity on permeability and thickness), giving a BHP that reacts similar for the same change in its well interval over the different sensitivities. Furthermore, because the fracture only forms in the later stage of the operation, the drop in pressure dos not cause a sudden change of phase, meaning that the thermodynamic properties of the CO_2 do not change drastically due to fracturing. If the fracture would initiate on much lower pressures, the impact on injectivity is expected to be much higher.

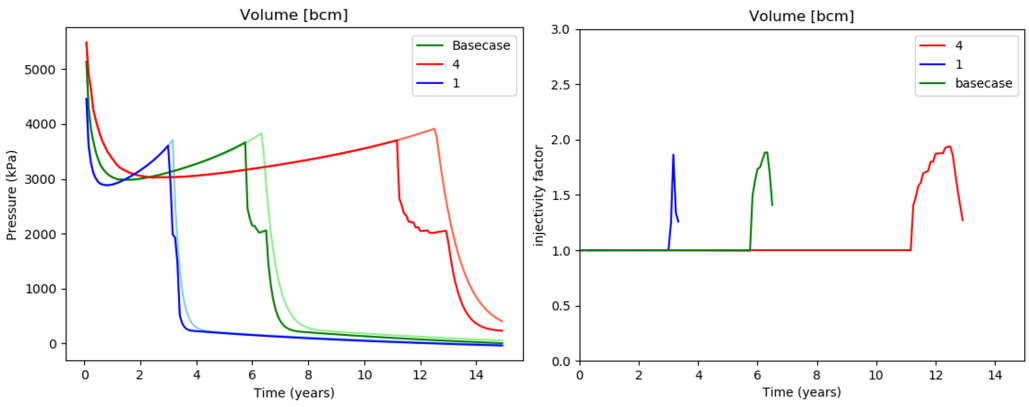

Figure 6.9: Left: BHP changes due to fracturing of the high, low and basecase with changing reservoir volume. Red shows the highcase, light red the unfractured high case. Blue is the lowcase and lightblue the unfractured lowcase and green is the basecase' BHP. Right: Injectivity change for Volume sensitivity, in comparison with the basecase. The graph ends at the moment the BHP constraint is reached. The maximum is similar for all cases as the CO_2 does not change phases and the well interval is modified the same when fractures initiate.

Appendix C includes the injectivity increase for all the high and low cases of each parameter, in comparison to the basecase. The sensitivities show that after fracturing, the ratio remains close to constant until the BHP constraint is reached. Figure 6.10 includes the maximum injectivity ratios for all the sensitivities. It can be seen that only the cases that impact the BHP directly, being the permeability and the injection rate, have a maximum injectivity ratio that is slightly different to the other cases, with injectivity ratios reaching from 1.5 to 2.1. The other cases do not show a change in maximum injectivity ratio, as these parameters only impact the way the reservoir reacts on stress changes, not necessarily the effect of the fracture.

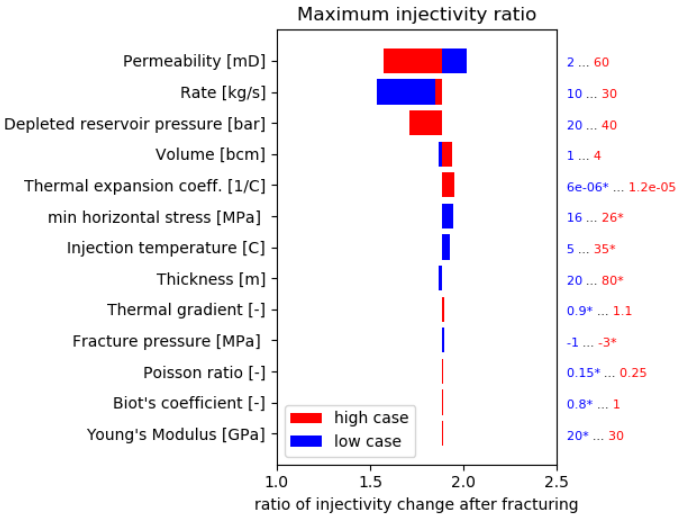

Figure 6.10: Injectivity ratio of all the high- and lowcases of each parameter. If there is no bar and an asterisk next to the label, it means there was no fracturing. If there is no bar and no asterisk next to the label, it means that the injectivity factor is the same as the basecase.

6.4. Consequences of a changing injection constant

The depletion constant of the basecase is 0.675. For the above sensitivities, the injection constant is assumed to be equal to depletion constant. By changing the Poisson ratio the injection constant can be altered. The injection constant would then be expected to have a similar impact to the reservoir as the sensitivity on the Poisson ratio has. Industry standard is that a depletion constant of 0.7 results in an injection constant of 0.6. Figure 6.11 includes the BHP, injectivity and injectivity ratio of the basecase simulation and simulations with an injection constant of 0.6 and 0.5. The fracture time gets reduced drastically with a lower injection constant. The fracture halflength increases, as fracture happens sooner creating a fluid pathway, causing further propagation of the thermal front. The injectivity ratio, however, remains constant, meaning that the pressure build up in the reservoir does not react differently due to an early fracture time and longer halflength.

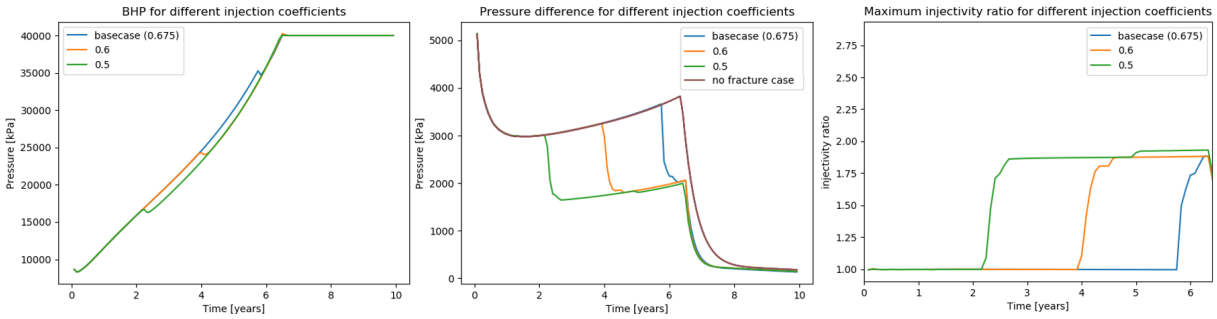

Figure 6.11: The BHP, pressure difference and injectivity ratio of simulations with an injection constant of 0.675 (which is the injection constant of the basecase), 0.6 and 0.5. Different injection ratios show a reaction of the minimum stress path and cause an earlier fracture time with lower injection ratio, but no change in injectivity increase.

7

Discussion

This chapter describes the observations that can be made from chapter 6, how the sensitivity analysis can be interpreted and used for better characterization of thermal fractures in depleted gasfields and how the results compare to other research and how this research can be extended in future work.

7.1. Trends in the fracture characteristics

Figure 7.1 include the tornado's sorted on rock properties, reservoir properties, operational properties and stress conditions, instead of sorting on impact. This allows to compare the different fracture characteristics with each other.

The top four parameters, the rock properties, show a consistent result; the high cases cause earlier fracture time at lower BHP values with longer fracture halflengths. The injectivity ratio remains constant. This implies that a change in the geomechanical properties does not impact the CO_2 propagation and the pressure build-up before fracturing, as well as the effect fracturing has on the injectivity, but solely impacts the stress path (the injection coefficient). The longer fracture halflengths can be explained by the fact that earlier fracture time means a favorable fluid path in the direction of the fracture, causing the thermal front to propagate further and thus further fracture propagation. The range of impact of the low and high case differ between the parameters, showing that the thermal expansion coefficient has a higher range in which it occurs in the North Sea and thus may be prioritized during data collection over for instance the Biot's coefficient, which solely impacts the poroelastic effect with a factor in a range from 0.8 to 1, having only a small impact on the whole simulation.

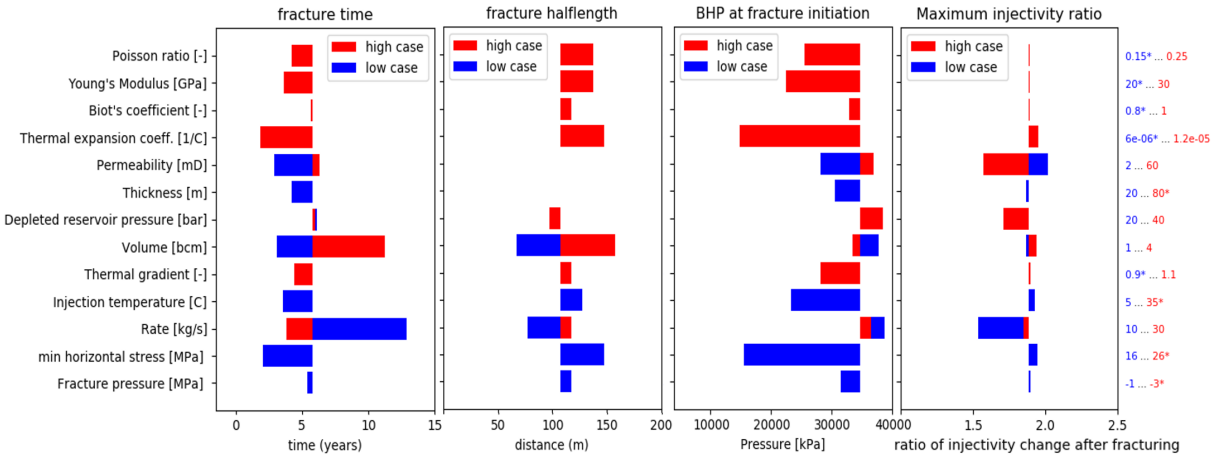

Figure 7.1: The tornado's of fracture time, fracture halflength, fracture BHP and maximum injectivity ratio ordered on property.

The reservoir parameters (permeability, thickness, depleted reservoir pressure, volume and thermal gradient) each impact the fracturing differently. The permeability and the thickness both change the effective permeability of the reservoir, where low permeability and thickness means that the pressure build-up around the well is faster and thus fracture time is sooner. The low permeability case also shows a maximum injectivity increase of 2.1 as the pressure build-up around the well causes a higher pressure

release after fracturing as the contrast between the pressure in the near-wellbore region and the rest of the reservoir is greater. The maximum injectivity increase with high permeability shows the opposite result. The fracture propagation is equal to the basecase for both the permeability and the thickness. This is not because the pressure build-up is the same, but because low permeability causes higher pressure build-up and thus less far propagation of the thermal front. The earlier fracturing then allows the thermal front to propagate again, reaching as far as the basecase. The same effect is reached by lower thickness, while higher permeability shows the opposite effect.

The reservoir volume impacts the reservoir differently compared to other parameters. A higher reservoir volume means that the average pressure build-up in the reservoir is slower, causing slower pressure build-up in the near-wellbore region and a later fracture time. The pressure build-up is slower, which means that higher BHP conditions are needed to reach fracture conditions in the reservoir. This also causes the CO_2 to propagate for a longer time period, causing the thermal front to reach further in the reservoir.

The thermal effects on the reservoir, the thermal gradient and the injection temperature, both show that a larger ΔT in the reservoir causes a more intense thermoelastic response, resulting in faster fracturing on lower pressure conditions. As is concluded before, lower pressure conditions at fracture initiation causes further thermal front propagation, as well as earlier fracturing, which both enhance the fracture halflength.

The rate changes the pressure build-up in the near-wellbore region in such a manner that higher BHP values are needed to reach the required pressure build-up as the contrast between well and reservoir pressure are not as high as with higher rates. This causes the fracture to initiate much later in time, causing the thermal front to propagate less far as the end of the project's lifetime is reached shortly after.

Lastly, different stress conditions do not change the pressure build up or the gradient of the stress path during simulation, but only change when fracture initiation happen. This, again, has positive feedback on the fracture length and fracture BHP.

The overarching result shows that for all the parameters that not directly impact how the CO_2 flows in the reservoir and changes the pressure build-up in the reservoir, the BHP at fracture initiation can be directly correlated with the fracture time. The injectivity changes similarly for all cases as the well interval and the pressure build-up does not change for most parameters, except for permeability, thickness and rate.

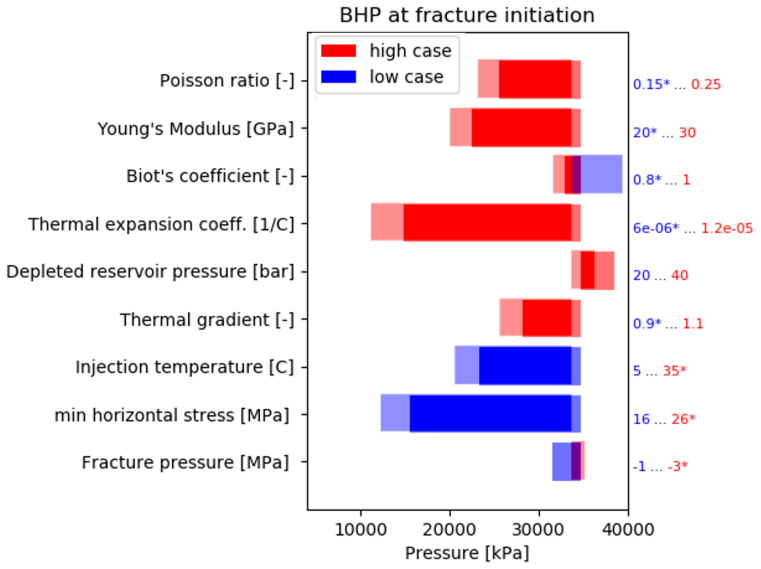

Figure 7.2: Comparison of the analytical result with the numerical result for the parameters included in the porothermoelastic equations. The lighter red and blue are the analytical solution, the stronger red and blue are the numerical solution.

7.2. Validation numerical solution

The analytical solution with the adjustment factor can be used to analytically validate the simulation results of the sensitivity analysis. Figure 7.2 shows the analytical solution of the pore pressure at fracture initiation projected over the numerical solution for BHP for the parameters that are adjustable in the thermoporoelastic equations. It shows that the analytical solution is very similar to that of the numerical solutions, where the difference can be explained by the fact that the numerical solution also includes the displacement in its calculation for the stress conditions, but more importantly that the BHP is the pressure at the bottom of the well and not the pressure locally in the reservoir at the location of fracture initiation. However, it does show that the reservoir follow the thermoporoelastic equations, and that the analytical solution can be used as an indication for fracture time, as the previous section concluded that the fracture time and BHP at fracture time have a direct relationship with each other for the parameters that are included in Figure 7.2.

7.3. Comparison with other research

The effect of the thermal front extending its reach when the pressure effect is less dominant is supported by Goodarzi, Settari, and Keith [8]. This research, while only looking closely to the effect of different operating conditions (injection temperatures and injection rate) does not include an insight on the reservoir parameters, but it concluded that, similarly to this research, when the poroelasticity is the driving force behind fracturing [16], the thermal fracture reaches less far compared to when thermoelasticity is the driving force.

The thermoelastic stress is also researched by Vilarrasa and Laloui [13] and Jung, Espinoza, and Hosseini [17]. The former found that the effect of thermal stresses by changing the thermal expansion coefficient in the caprock showed that no fracture propagation to the caprock is expected in any case, but when the thermal expansion coefficient is significantly higher in the caprock, it could cause plastic deformation. However, caprock integrity would not be compromised, similarly as is found in this research with the expected stress changes due to cooling. According to Jung, Espinoza, and Hosseini [17], the thermal expansion coefficient and the Young's modulus are most important during data collection in carbon sequestration projects in saline aquifers, to correctly predict fracture time and fracture halflength. Comparing this to CO_2 injection in depleted fields in the North Sea as is done in this research, the thermal expansion coefficient remains as a very important parameter to closely examine. However, the range of uncertainty of the Young's modulus is not as extreme.

The cooling of the caprock can however be examined in this research. Comparing it to Vilarrasa [57] it can be seen that buoyancy effects of the cold CO_2 cause more extensive cooling of the caprock, while this is not the case with the depleted reservoir simulation in this research as the tight reservoirs causes a very limited buoyant effect, causing the plume to propagate elliptically. This, together with the fact that it does have a low water saturation compared to the CO_2 injection projects in aquifers (so less buoyant CO_2 as the difference in density between methane and CO_2 is lower than water and CO_2), makes the cooling of the caprock to be less extreme in depleted gas reservoir injection.

The increase in injectivity due to thermal fracturing in this research is similar to that of Goodarzi, Settari, and Keith [8], which found an injectivity increase of a factor two. Similarly, Jung, Espinoza, and Hosseini [17] found that a field case experienced a constant BHP while ramping up the rate to be twice as high, presumably due to the effect of thermal fractures. However, in Goodarzi et al. [16], it is found that the injectivity increases with longer fracture halflengths for shear fractures due to thermal effects. This contradicts this research, which finds that the injectivity remains constant and only affects the way the CO_2 flows into the reservoir, extending the reach of the thermal front.

The fracturing happens late in the operation's lifetime in depleted gasfield injection, which is conform with the findings of Park [58]. However, different injection constants could really expedite fracturing, leading to more intensive pressure differences between the BHP and the reservoir.

All in all, the behaviour of thermal fractures in a depleted gasfields seem very similar to thermal fractures in saline aquifers, but the thermoelastic effect has a more prominent role and fractures are likely to form

at a later stage of the operation compared to carbon storage in saline aquifers.

7.4. Applicability

This study helps to comprehend how each parameter affects the way thermal fractures behave. According to which outcome might be sought, this can help to prioritize which data should be collected based on high impact parameters.

If, e.g., it is suspected that the injectivity increase due to fracturing might be problematic (formation of gas hydrates), it can be decided to inject on a lower rate with lower temperatures. This causes the CO_2 in the well to remain in supercritical phase, but causes more extreme cooling but a less intense injectivity increase.

A second example could be, that when a reservoir is expected to fracture during injection and the consequences of the calculated injectivity increase is not problematic, it can be decided to economize on the investigation on geomechanic parameters, as these parameters do not change the injectivity, because fracturing is only expected in a later stage of the operation, when the NWB region is single phase.

Overall, during operation characterization, some parameters have higher uncertainty than others, while others might be much more expensive to gather accurately. The outcome of the sensitivity analysis gives an insight to what parameters the emphasis should be on while describing the operation conditions to minimize the uncertainty of thermal fractures. This avoids wasting resources on less impactful parameters and improving the injection strategy of future CCS projects in depleted gasfields.

7.5. Future research

Future research could improve the applicability of this research to actual field cases. The most sensible improvement would be to investigate the effect of heterogeneity. The heterogeneity would impact both the horizontal and vertical propagation of the fracture by changing the pressure build-up in the reservoir and the manner in which it cools locally, as well as different injectivity increases as not all lithologies along the well interval would fracture at the same time.

Other improvements could be how the other NWB effects have an influence on the injectivity, the pressure build-up and how they provide feedback on each process.

A more operational-focused query is how temporary shut in of the well due to maintenance can influence the pressure build-up around the well as well as the propagation of the thermal front, and how a restart of the operation deals with fractures and its impact on injectivity. Hereby it is interesting to see how the restart of the well reacts to low BHP conditions, in which the two-phase region might be reached, which might react differently to the enhanced injectivity by the fractures.

Another interesting point is the total effect of stress hysteresis, and how this would impact all the sensitivities. If the GEM software issue for the calculation of the minimum stress can be solved, other deepening in to geomechanical reactions is possible. The caprock's integrity can be elaborated on by initializing the caprock by fitting geomechanical parameters, porosity and permeability settings as well as correct saturation levels. This way, a sensitivity analysis can be conducted to find under what conditions the caprock integrity may be jeopardized.

Lastly, as an elaboration on the previous proposal, it can be insightful to see how the sensitivities effect the stress conditions when the fracture reaches a fault. A fault can redirect the angle of internal friction, creating shearing conditions. Reactivation of such faults could also jeopardize caprock integrity.

8

Conclusion

This research describes how thermal fractures can impact the near-wellbore region during CO_2 injection in a depleted gas reservoir that is being used for CCS purposes. Firstly, the flow characteristics of CO_2 and the geomechanical reaction under changing pressure and temperature conditions are discussed.

Secondly, a method for accurately simulating a homogeneous box model with a dual permeability grid system is defined, to simulate propagation of the CO_2 in a depleted gasfield. Hereby it is also explained how the temperature and the pressure develops during injection.

Thirdly, a basecase model is defined together with a low- and highcase scenario for each influential parameter. Each sensitivity's fracture time, fracture halflength and BHP at fracture time is determined, together with the effect on the injectivity of the reservoir. It is found that the geomechanical properties do not affect how the near-wellbore region of the reservoir reacts to fracturing, resulting in constant injectivity increases for each parameter. It does, however, impact the fracture time. Sooner fracturing leads to further propagation of the thermal front, whose extent means longer fracture halflengths. The reservoir parameters do not change how the reservoir reacts to stress, but changes the way the reservoir handles pressure build-up. The thickness and the permeability define the effective permeability, where a lower effective permeability means faster and higher pressure values around the well, resulting in a more local thermal plume, but sooner fracture initiation. As these parameters effectively change the way the reservoir reacts to pressure build-up, these parameters influence the injectivity increase due to fracturing. The volume has a similar effect as the effective permeability, but with a slower pressure build-up for larger volumes around the well due to a lower average pressure, instead of the higher BHP values due to the flow properties. The operational parameters are similar to the reservoir parameters. The rate influences the pressure build-up around the well and thus the injectivity increase due to fracturing, while the injection temperature determines the pressure dependence during thermal fracture initiation, with lower injection temperatures resulting in fracturing at lower pressure conditions. It is important, however, to realise that the the last two parameters are the only two that can be changed during operation.

Furthermore, it is found that the injection constant due to stress hysteresis not necessarily changes the results much in terms of injectivity increase, but, similarly to the geomechanical parameters, cause earlier fracture time and a prolonged fracture propagation due to the fluid paths the fracture creates.

Then, the numerical solution is validated by the analytical solution, which is based on the thermoporoelastic effect. It is found that with an adjustment factor of 0.77 to the thermoelastic effect the analytical solution of the pressure at which fracture initiation occurs is more or less the same as the numerical solution. This means that the analytical solution can be used to make an indication on the fracture time once the pressure development is known in a reservoir under the preferred injection strategy.

Lastly, the outcome as showcased above can be used to better understand on which parameters the focus must be on during data collection to better describe the effect of thermal fractures. In this consideration, the accepted consequences must be known; if the thermal fractures are preferably avoided, if the injectivity increase must be minimized or that the fracture halflength must be contained to a certain region. Economic considerations should also be made, e.g. if it is as costly to gather information on the Biot's coefficient as it is for the stress conditions, it is much more appealing to have a closer understanding of the stress conditions. This way, the injection strategy can be maximally improved with the minimal economic costs in terms of the effect thermal fractures have on the operation.

A

SNS database

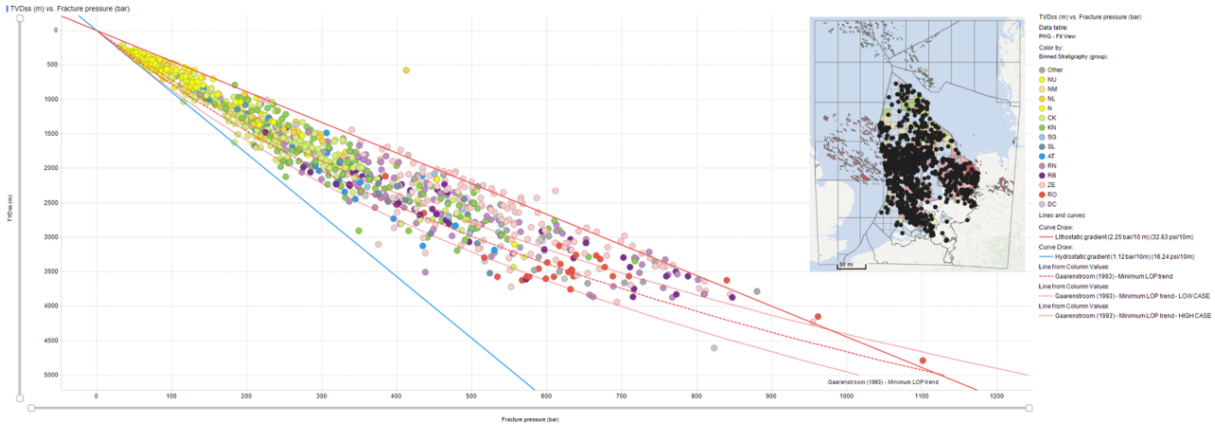

Figure A.1: Leak off test data from 1143 wells. A trendline is added to find the minimum LOP change with depth for the subsurface of the Netherlands and the Dutch North Sea.

Figure A.2: Well temperature data from 1143 wells. A trendline is added to find the temperature gradient for the subsurface of the Netherlands and the Dutch North Sea.

B

Analytical solutions

This appendix includes all the sensitivities that are calculated for the minimum stress decrease over pressure increase in Figure C.4 and Figure B.2. These solutions populate the tornado plots of the analytical sensitivity analysis.

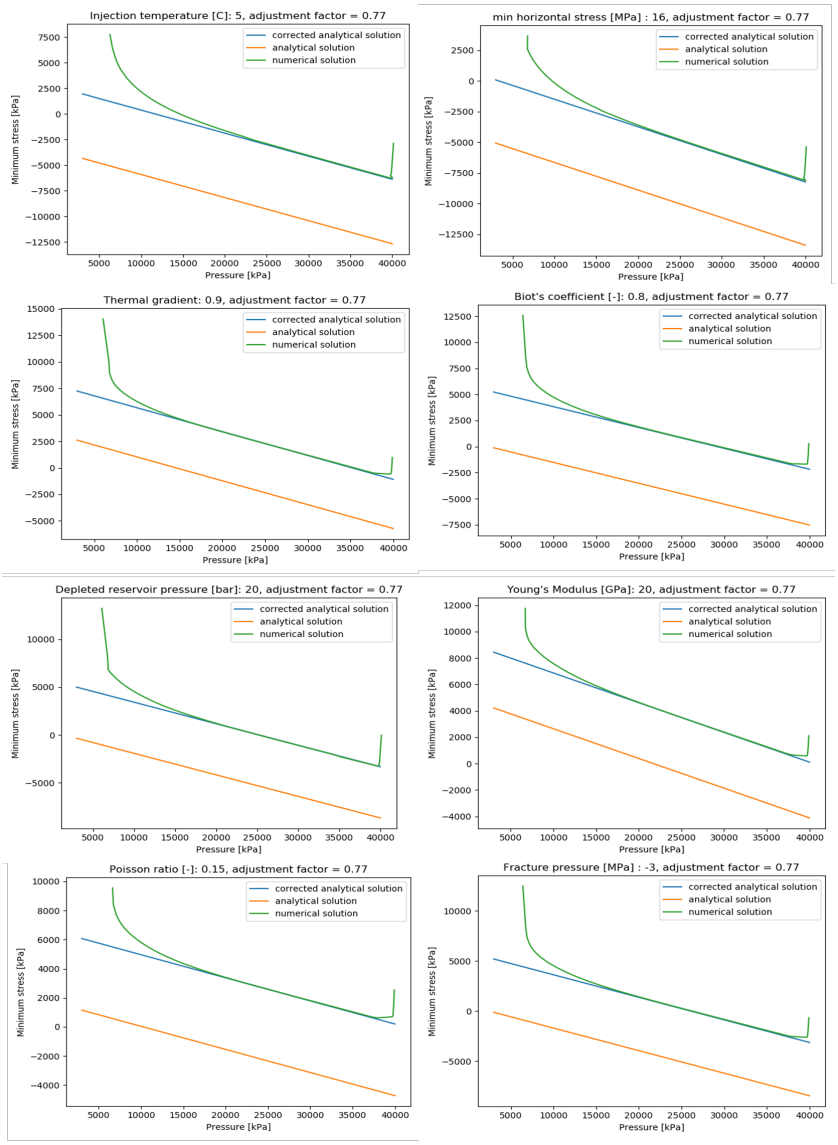

Figure B.1: Injectivity ratio of the basecase. On the left the difference between BHP and average reservoir pressure is plotted for the basecase with fracturing and with fracturing turned off. Fracture iniation causes a sharp drop. Right: injectivity ratio between the fracture and the non-fracture case. THe maximum injectivity ratio due to fracturing is 1.85.

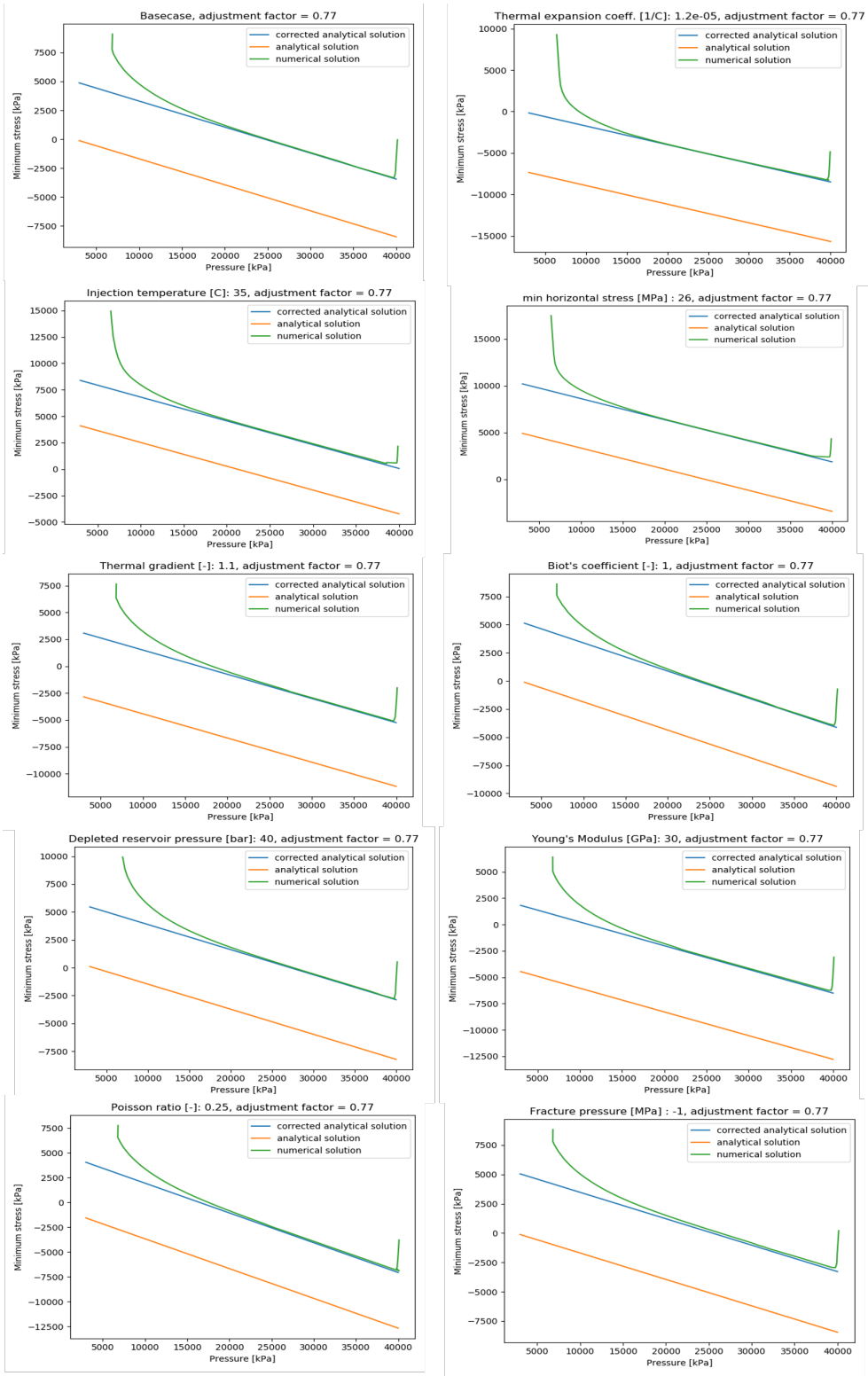

Figure B.2: Injectivity ratio of the basecase. On the left the difference between BHP and average reservoir pressure is plotted for the basecase with fracturing and with fracturing turned off. Fracture iniation causes a sharp drop. Right: injectivity ratio between the fracture and the non-fracture case. THe maximum injectivity ratio due to fracturing is 1.85.

C

Fracture and no fracture cases

This appendix includes the BHP over time of each parameter with and without fracturing, including the basecase to clearly show the effect of the low and highcase. The red lines represent the high case scenarios, with the lighter red being the high case scenario without fracturing. The blue line is the low case scenario, with light blue being the same case without fracturing. The green case is the basecase' BHP development over time for comparison purposes.

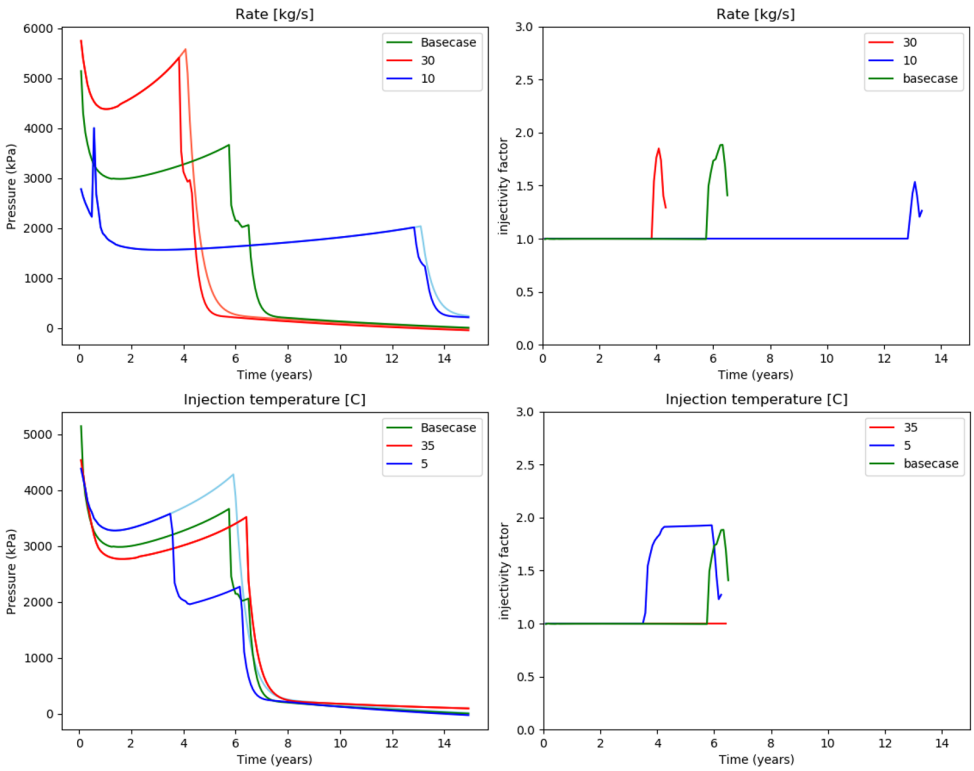

Figure C.1: Injectivity ratio of the basecase. On the left the difference between BHP and average reservoir pressure is plotted for the basecase with fracturing and with fracturing turned off. Fracture iniation causes a sharp drop. Right: injectivity ratio between the fracture and the non-fracture case. THe maximum injectivity ratio due to fracturing is 1.85.

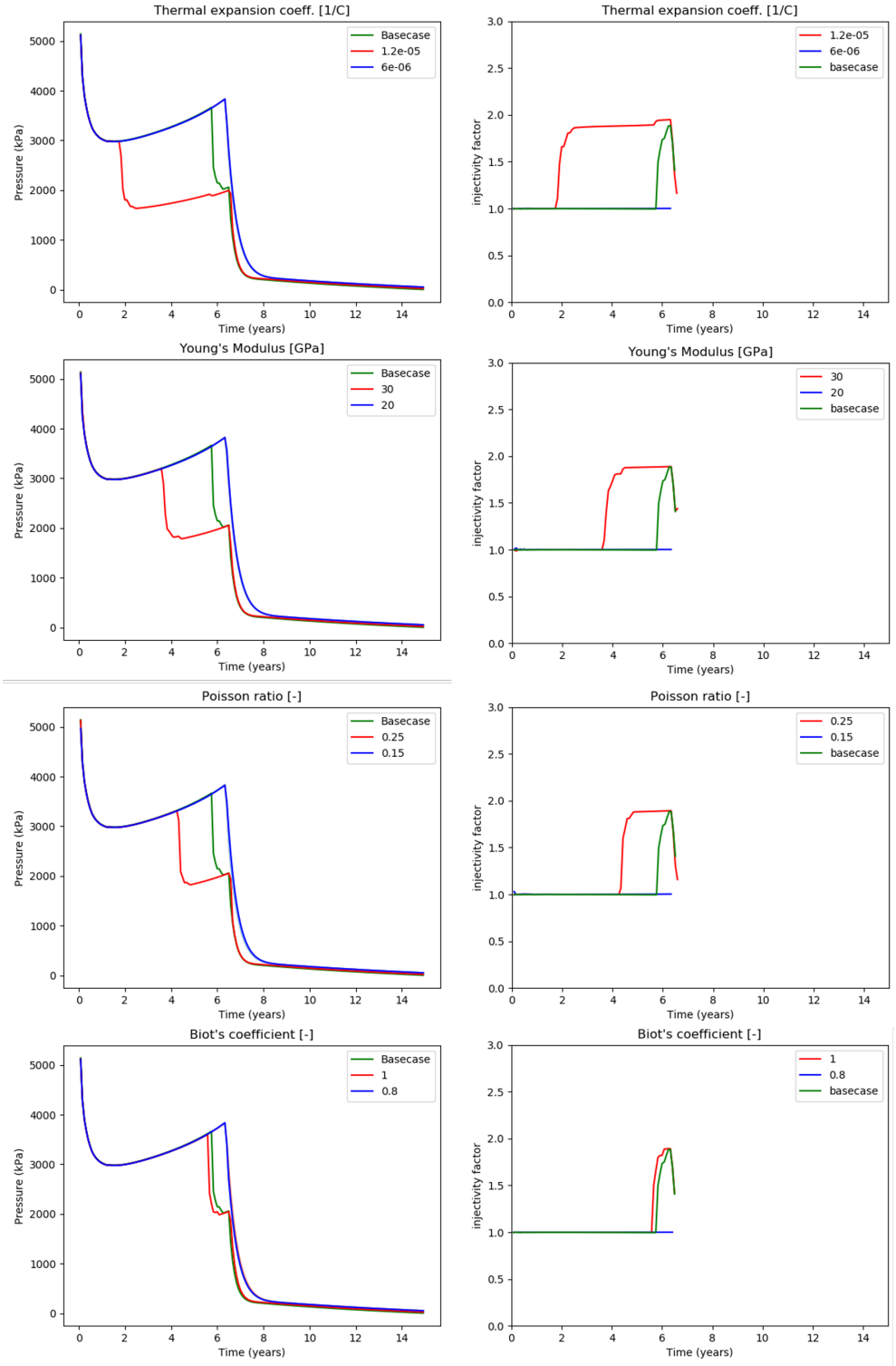

Figure C.2: Injectivity ratio of the basecase. On the left the difference between BHP and average reservoir pressure is plotted for the basecase with fracturing and with fracturing turned off. Fracture iniation causes a sharp drop. Right: injectivity ratio between the fracture and the non-fracture case. THe maximum injectivity ratio due to fracturing is 1.85.

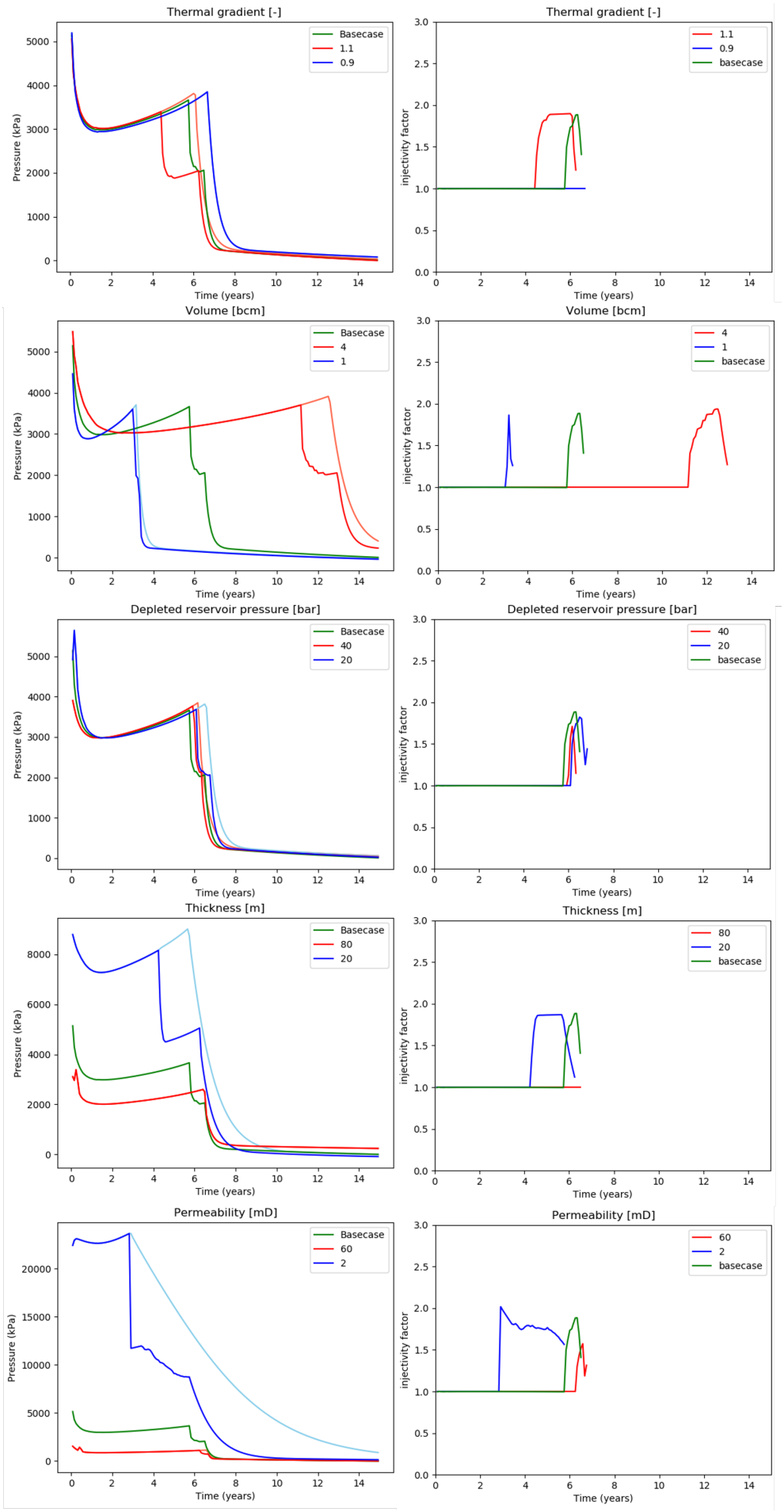

Figure C.3: Injectivity ratio of the basecase. On the left the difference between BHP and average reservoir pressure is plotted for the basecase with fracturing and with fracturing turned off. Fracture iniation causes a sharp drop. Right: injectivity ratio between the fracture and the non-fracture case. THe maximum injectivity ratio due to fracturing is 1.85.

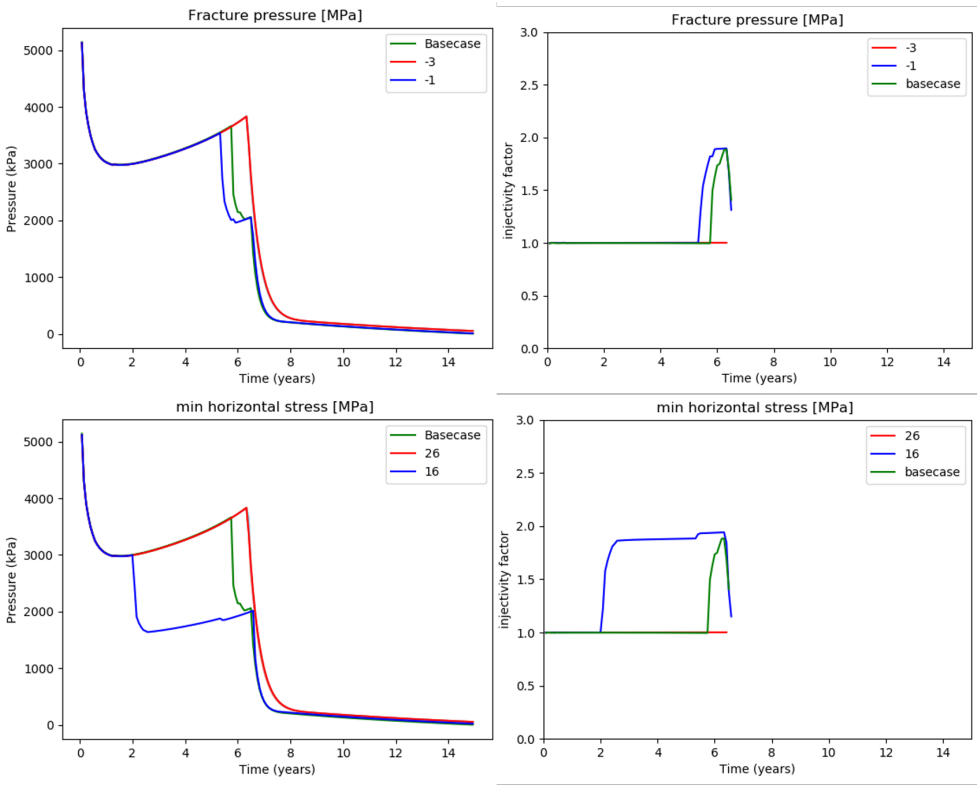

Figure C.4: Injectivity ratio of the basecase. On the left the difference between BHP and average reservoir pressure is plotted for the basecase with fracturing and with fracturing turned off. Fracture iniation causes a sharp drop. Right: injectivity ratio between the fracture and the non-fracture case. THe maximum injectivity ratio due to fracturing is 1.85.

Bibliography

[1] Valérie Masson-Delmotte et al. “Global warming of 1.5 C”. In: *An IPCC Special Report on the impacts of global warming of* 1.5 (2018).

[2] Robbie M Andrew. “A comparison of estimates of global carbon dioxide emissions from fossil carbon sources”. In: *Earth System Science Data* 12.2 (2020), pp. 1437–1465.

[3] Pierre Friedlingstein et al. “Global carbon budget 2021”. In: *Earth System Science Data Discussions* (2021), pp. 1–191.

[4] Harold Koster. “Het Integraal Nationaal Energie-en Klimaatplan 2021-2030”. In: *Bedrijfsjuridische Berichten* 6 (2020).

[5] JM Ketzer et al. *Brazilian atlas of CO2 capture and geological storage*. 2015.

[6] Brad Page et al. “Global status of CCS 2021”. In: *Global CCS Institute* (2021).

[7] Haixia Wang, Jusheng Chen, and Qingling Li. “A Review of Pipeline Transportation Technology of Carbon Dioxide”. In: *IOP Conference Series: Earth and Environmental Science*. Vol. 310. 3. IOP Publishing. 2019, p. 032033.

[8] Somayeh Goodarzi, Antonin Settari, and David Keith. “Geomechanical modeling for CO2 storage in Nisku aquifer in Wabamun Lake area in Canada”. In: *International Journal of Greenhouse Gas Control* 10 (2012), pp. 113–122.

[9] Pengcheng Fu et al. *CO2 injection with fracturing in geomechanically protected caprock: Task 6 of LLNL’s Research Activities to Support DOE’s Carbon Storage Program (FWP-FEW0191)(Final Technical Report)*. Tech. rep. Lawrence Livermore National Lab.(LLNL), Livermore, CA (United States), 2020.

[10] E Peters et al. “Consequences of thermal fracture developments due to injection cold CO2 into depleted gas fields”. In: *Energy Procedia* (2013), pp. 1–18.

[11] Somayeh Goodarzi et al. “Thermal effects on shear fracturing and injectivity during CO2 storage”. In: *ISRM International Conference for Effective and Sustainable Hydraulic Fracturing*. OnePetro. 2013.

[12] JG Veldkamp et al. *Thermal fracturing due to low injection temperatures in geothermal doublets*. Utrecht: TNO, 2016.

[13] Victor Vilarrasa and Lyesse Laloui. “Impacts of thermally induced stresses on fracture stability during geological storage of CO2”. In: *Energy Procedia* 86 (2016), pp. 411–419.

[14] Jie Bao, Zhijie Xu, and Yilin Fang. “A coupled thermal-hydro-mechanical simulation for carbon dioxide sequestration”. In: *Environmental Geotechnics* 3.5 (2014), pp. 312–324.

[15] Zhiyuan Luo and Steven Bryant. “Impacts of Injection Induced Fractures Propagation in CO2 Geological Sequestration–is fracturing good or bad for CO2 sequestration”. In: *Energy Procedia* 63 (2014), pp. 5394–5407.

[16] S Goodarzi et al. “Optimization of a CO2 storage project based on thermal, geomechanical and induced fracturing effects”. In: *Journal of Petroleum Science and Engineering* 134 (2015), pp. 49–59.

[17] Hojung Jung, D Nicolas Espinoza, and Seyyed A Hosseini. “Wellbore injectivity response to step-rate CO2 injection: Coupled thermo-poro-elastic analysis in a vertically heterogeneous formation”. In: *International Journal of Greenhouse Gas Control* 102 (2020), p. 103156.

[18] David S Hughes. “Carbon storage in depleted gas fields: Key challenges”. In: *Energy Procedia* 1.1 (2009), pp. 3007–3014.

[19] RJ Arts et al. “The feasibility of CO2 storage in the depleted P18-4 gas field offshore the Netherlands (the ROAD project)”. In: *International Journal of Greenhouse Gas Control* 11 (2012), S10–S20.

[20] *Geode*. URL: https://www.geodeatlas.nl/.

[21] Suzanne Brunsting et al. “Stakeholder participation practices and onshore CCS: Lessons from the Dutch CCS Case Barendrecht”. In: *Energy Procedia* 4 (2011), pp. 6376–6383.

[22] E De Visser, R De Vos, and C Hendriks. “Catching carbon to clear the skies. Experiences and highlights of the Dutch R and D programme on CCS”. In: (2009).

[23] Andrea Ramirez et al. “Screening CO2 storage options in the Netherlands”. In: *International Journal of Greenhouse Gas Control* 4.2 (2010), pp. 367–380.

[24] *Porthos Project*. Apr. 2022. URL: https://www.porthosco2.nl/project/.

[25] Theo Wong, D.A.J. Batjes, and Jan de Jager. “Geology of the Netherlands”. In: (Jan. 2007).

[26] Abdus Satter and Ghulam M Iqbal. “11-Primary recovery mechanisms and recovery efficiencies”. In: *Reservoir engineering* (2016), pp. 185–193.

[27] Jarand Gauteplass et al. “Hydrate Plugging and Flow Remediation during CO2 Injection in Sediments”. In: *Energies* 13.17 (2020), p. 4511.

[28] Mark D Zoback. *Reservoir geomechanics*. Cambridge university press, 2010.

[29] Richa Shukla et al. “A review of studies on CO2 sequestration and caprock integrity”. In: *Fuel* 89.10 (2010), pp. 2651–2664.

[30] Clement John Adkins and Clement John Adkins. *Equilibrium thermodynamics*. Cambridge University Press, 1983.

[31] M Babar et al. “Identification and quantification of CO2 solidification in cryogenic CO2 capture from natural gas”. In: *International Journal of Automotive and Mechanical Engineering* 15.2 (2018), pp. 5367–5367.

[32] Ludovic Nicolas Legoix et al. “Phase equilibria of the CH4-CO2 binary and the CH4-CO2-H2O ternary mixtures in the presence of a CO2-rich liquid phase”. In: *Energies* 10.12 (2017), p. 2034.

[33] Beatriz Gimeno et al. “Thermodynamic properties of CO2+ SO2+ CH4 mixtures over wide ranges of temperature and pressure. Evaluation of CO2/SO2 co-capture in presence of CH4 for CCS”. In: *Fuel* 255 (2019), p. 115800.

[34] Michiel Creusen. *Near wellbore effects induced by CO2 injection and the influence on injectivity in depleted gas reservoirs*. 2018.

[35] Curtis M Oldenburg. “Joule-Thomson cooling due to CO2 injection into natural gas reservoirs”. In: *Energy Conversion and Management* 48.6 (2007), pp. 1808–1815.

[36] JNE Carneiro et al. “Numerical simulations of high CO2 content flows in production wells, flowlines and risers”. In: *OTC Brasil*. OnePetro. 2015.

[37] T Huijskes and W Schiferli. “Implications of Near-Wellbore Phenomena during CO2 injection in Depleted Gas Fields”. In: *EAGE GET 2022*. Vol. 2022. 1. European Association of Geoscientists & Engineers. 2022, pp. 1–5.

[38] COMPUTER MODELLING GROUP LTD. *GEM User Guide 2020.10: Compositional Unconventional Simulator*. 2020.

[39] Ding-Yu Peng and Donald B Robinson. “A new two-constant equation of state”. In: *Industrial & Engineering Chemistry Fundamentals* 15.1 (1976), pp. 59–64.

[40] Seif-Eddeen K Fateen, Menna M Khalil, and Ahmed O Elnabawy. “Semi-empirical correlation for binary interaction parameters of the Peng–Robinson equation of state with the van der Waals mixing rules for the prediction of high-pressure vapor–liquid equilibrium”. In: *Journal of advanced research* 4.2 (2013), pp. 137–145.

[41] Long Nghiem et al. “Modeling CO2 storage in aquifers with a fully-coupled geochemical EOS compositional simulator”. In: *SPE/DOE symposium on improved oil recovery*. OnePetro. 2004.

[42] Martin Petitfrere et al. “Full-EoS based thermal multiphase compositional simulation of CO2 and steam injection processes”. In: *Journal of Petroleum Science and Engineering* 192 (2020), p. 107241.

[43] COMPUTER MODELLING GROUP LTD. “STARS User Guide 2020.10: Thermal advanced Processes Simulator”. In: (2020).

[44] Amos Nur and J_D Byerlee. “An exact effective stress law for elastic deformation of rock with fluids”. In: *Journal of geophysical research* 76.26 (1971), pp. 6414–6419.

[45] TK Perkins and JA Gonzalez. “Changes in earth stresses around a wellbore caused by radially symmetrical pressure and temperature gradients”. In: *Society of Petroleum Engineers Journal* 24.02 (1984), pp. 129–140.

[46] MHH Hettema et al. “Production-induced compaction of a sandstone reservoir: the strong influence of stress path”. In: *SPE Reservoir Evaluation & Engineering* 3.04 (2000), pp. 342–347.

[47] DCP Peacock, David J Sanderson, and Bernd Leiss. “Use of Mohr Diagrams to Predict Fracturing in a Potential Geothermal Reservoir”. In: *Geosciences* 11.12 (2021), p. 501.

[48] Jonathan M Ramsey and Frederick M Chester. “Hybrid fracture and the transition from extension fracture to shear fracture”. In: *Nature* 428.6978 (2004), pp. 63–66.

[49] FJ Santarelli et al. “Reservoir stress path: the depletion and the rebound”. In: *SPE/ISRM Rock Mechanics in Petroleum Engineering*. OnePetro. 1998.

[50] RM Holt, S Gheibi, and A Lavrov. “Where does the stress path lead? Irreversibility and hysteresis in reservoir geomechanics”. In: *50th US Rock Mechanics/Geomechanics Symposium*. OnePetro. 2016.

[51] James R Gilman and Hossein Kazemi. “Improvements in simulation of naturally fractured reservoirs”. In: *Society of petroleum engineers Journal* 23.04 (1983), pp. 695–707.

[52] K a Uleberg and J Kleppe. “Dual porosity, dual permeability formulation for fractured reservoir simulation”. In: *Norwegian university of science and technology, trondheim RUTH seminar, stavanger*. 1996.

[53] Mohammad Mesbah, Ali Vatani, and Majid Siavashi. “Streamline simulation of water-oil displacement in a heterogeneous fractured reservoir using different transfer functions”. In: *Oil & Gas Sciences and Technology–Revue d’IFP Energies nouvelles* 73 (2018), p. 14.

[54] Jon Jincai Zhang. *Chapter 6 - In situ stress estimate*. Ed. by Jon Jincai Zhang. Gulf Professional Publishing, 2019, pp. 187–232. ISBN: 978-0-12-814814-3. DOI: https://doi.org/10.1016/B978-0-12-814814-3.00006-X. URL: https://www.sciencedirect.com/science/article/pii/B978012814814300006X.

[55] Boyun Guo. *Well productivity handbook: vertical, fractured, horizontal, multilateral, multi-fractured, and radial-fractured wells*. Gulf Professional Publishing, 2019.

[56] Saeed Salimzadeh, Adriana Paluszny, and Robert W Zimmerman. “Effect of cold CO2 injection on fracture apertures and growth”. In: *International Journal of Greenhouse Gas Control* 74 (2018), pp. 130–141.

[57] Víctor Vilarrasa. “The role of the stress regime on microseismicity induced by overpressure and cooling in geologic carbon storage”. In: *Geofluids* 16.5 (2016), pp. 941–953.

[58] J Park. “P18 CCS: Thermal Fracture Simulation”. In: (2020).